Electrophysiological and Computational Approaches to the Investigation and Diagnosis of Motor System Dysfunction

DISSERTATION

Presented in Partial Fulfillment of the Requirements for the Degree Doctor of Philosophy
in the Graduate School of The Ohio State University

By

Thomas Hirschauer

Graduate Program in Neuroscience

The Ohio State University

2015

Dissertation Committee:

John Buford, Advisor

Hojjat Adeli, Co-advisor

Dana McTigue

Per Sederberg

Abstract

The motor system consists of multiple regions of the central nervous system involved in the control of movement. Because each component of the motor system contributes to a specific motor function, clinical signs and symptoms of motor impairment can often be used to deduce the nature and location of a neurological lesion. In this way, a better understanding of neuroanatomical pathways and functional connections between motor areas leads directly to improvements in the diagnosis and treatment of motor system dysfunction. The purpose of this dissertation was to utilize electrophysiological and computational techniques to study the motor outputs of the pontomedullary reticular formation (PMRF) and the computer-aided diagnosis (CAD) of parkinsonism.

Electrophysiological techniques are of particular usefulness in the study of motor function. In a research setting, electrical stimulation can be used to evoke neuronal action potentials. In the clinic, electroencephalography (EEG), nerve conduction studies, and electromyography (EMG) are used to assess motor system function for diagnosing disease and tracking its progression. Additionally, procedures such as transcranial direct-current stimulation and deep brain stimulation (DBS) can be used to modify brain activity during the treatment of certain disorders of the motor system. Computational methods are important in signal processing of electrophysiological recordings and modeling of motor pathways. Furthermore, machine learning algorithms are used in the CAD of neurological disorders.

The first study in this dissertation used electrophysiological techniques to study the motor outputs of the PMRF. The PMRF is the origin of the reticulospinal tract, one of the major descending motor pathways. The reticulospinal system is of particular importance following damage to the corticospinal tract. Unilateral cortical injury and motor cortex stroke, which cause corticospinal neuron death, classically result in contralateral hemiparesis. However, stroke patients also exhibit a loss of fractionated control of joints, abnormal flexion synergies, and a reemergence of the asymmetric tonic neck reflex. These additional motor symptoms indicate an increased reliance on reticulospinal pathways following damage to the corticospinal tract.

To better characterize the function of reticulospinal neurons in stroke patients and healthy subjects, the motor output of the PMRF was investigated by electrically stimulating PMRF neurons or recording spontaneous spiking. Stimulus-triggered averaging (StimulusTA) and spike-triggered averaging (SpikeTA) of EMG and force recordings were performed to identify event-related changes in motor output. EMG was recorded from 12 pairs of upper limb muscles in two monkeys (*M. fascicularis*) and forces were detected using two isometric force-sensitive handles. The majority of stimulation sites produced significant force and EMG responses, with an electromechanical delay (EMD) consistent with previous measurements in primates. The magnitude of force responses was correlated with the average post-stimulus change in EMG activity. A multivariate linear regression analysis was used to estimate the contribution of each muscle to force generation, with flexors and extensors exhibiting antagonistic effects.

A predominant force output pattern of ipsilateral flexion and contralateral extension was observed in response to PMRF stimulation, with the majority of significant ipsilateral force responses directed medially and posteriorly and the majority of contralateral responses directed laterally and anteriorly. This novel approach permits direct measurement of force outputs evoked by CNS microstimation. Despite the small magnitude of post-stimulus EMG effects, low-intensity single-pulse microstimulation of the PMRF evoked detectable forces. The forces, showing the combined effect of all muscle activity in the arms, were consistent with reciprocal pattern of force outputs from the PMRF detectable with StimulusTA of EMG.

In one monkey, the neural activity of PMRF neurons was recorded simultaneously with EMG activity and force output from arm and shoulder muscles. For some of these PMRF neurons, significant post-spike EMG and force effects were detected. These post-spike force effects were significantly correlated with post-spike EMG activity for the same recording site. Consistent with previous findings, PMRF neurons facilitated ipsilateral flexors and contralateral extensors, while suppressing ipsilateral extensors and contralateral flexors. Additionally, EMG and force effects of SpikeTA and StimulusTA obtained from the nearest stimulation site were positively correlated in all significant cases. These findings demonstrate that single PMRF neurons can directly influence force outputs of the upper limbs.

The second study in this dissertation used computational techniques to study the CAD of parkinsonism. Parkinson's disease (PD) is a movement disorder caused by degeneration of dopamine-producing neurons in the basal ganglia. It presents with characteristic parkinsonian motor symptoms – tremor, hypokinesia, rigidity, postural instability. Accurate diagnosis is difficult because other disorders like atypical parkinsonian syndromes (APS) also present with parkinsonian motor symptoms. It was recently discovered that about 10% of people diagnosed with PD do not have dopaminergic neuron loss. These subjects without evidence of dopaminergic deficits (SWEDDs) are thought to have a disorder known as dopa-responsive dystonia instead of PD. In order to differentiate between PD, SWEDDs, and healthy controls, an enhanced probabilistic neural network (EPNN) was implemented to classify subjects based on clinical exams and neuroimaging data.

The EPNN model diagnosed between all three classes with 92.5% accuracy. The Motor Disorder Society-sponsored revision of the Unified Parkinson's Disease Rating Scale Part III was shown to be the most effective clinical exam at differentiated between PD subjects and healthy controls. The putamen striatal-binding ratio of ioflupane (^{123}I), a radioactive compound that binds to dopamine transporters, was shown to be the most effective measurement at differentiating between PD and SWEDDs subjects. Clinical screening for SWEDDs using EPNN exhibited a sensitivity of 59.0% and specificity was 85.9%. Additionally, the results identify olfactory function, which was measured by the University of Pennsylvania Smell Identification Test, as a potential clinical indicator of

SWEDDs, supporting the hypothesis that SWEDDs has a different pathology than PD that disproportionately affects olfactory function.

To my wife, Sonia, and our new baby girl

Acknowledgments

I would like to thank my advisor, Dr. John Buford, for his much appreciated guidance and support throughout my training. Through his mentorship, I have been able to learn a wide range of neuroscience methods. I would also like to thank my coadvisor, Dr. Hojjat Adeli, who advised my computational studies and provided valuable insight and assistance. Thank you to my other committee members, Dr. Dana McTigue and Dr. Per Sederberg, for providing constructive guidance. And thanks to Rebecca Slattery, Amanda Feddersen, Alexis Ortiz-Rosario, Sarah Hulbert, Alexis Burns, and Lynnette Montgomery for their help and technical support. Finally, I would like to thank my wife, Sonia, who has encouraged me and supported me throughout my graduate studies.

This work was funded in part by R01 NS037822 to JAB. Data for the computer-aided diagnosis of parkinsonism was provided by the Parkinson's Progressive Marker's Initative (PPMI). PPMI – a public-private partnership – is funded by the Michael J. Fox Foundation for Parkinson's Research and funding partners, including AbbVie, Avid, Biogen, Bristol-Myers Squibb, Covance, GE Healthcare, Genentech, GlaxoSmithKline, Eli Lilly and Company, Lundbeck, Merck, Meso Scale Discovery, Pfizer, Piramal Imaging, Roche, Servier, and UCB.

Vita

2000-2004	St. Ignatius High School
2006-2006	Research Assistant, University of Nevada-Las Vegas
2007-2007	Research Assistant, University of California-Riverside
2008-2008	Research Assistant, University of Cincinnati
2004-2008	B.S. Physics, University of Dayton B.S. Biology, University of Dayton
2009-present	Medical Scientist Training Program, The Ohio State University College of Medicine
2011-present	Graduate Research Associate, Neuroscience Graduate Program, The Ohio State University

Publications

Hirschauer TJ, Buford JA (2015). Bilateral force transients in the upper limbs evoked by single-pulse microstimulation in the pontomedullary reticular formation. *Journal of Neurophysiology 113*(7): 2592-2604.

Szaflarski JP, DiFrancesco M, **Hirschauer T**, Banks C, Privitera MD, Gotman J, Holland SK (2010). Cortical and subcortical contributions to absence seizure onset examined with EEG/fMRI. *Epilepsy & Behavior 18*(4): 404-413.

Fields of Study

Major Field: Neuroscience

Minor Fields: Computer Science, Cognitive and Brain Sciences

Table of Contents

List of Tables

List of Figures

Chapter 1: Introduction

Normal motor system function

The motor system is comprised of various parts of the central nervous system that are involved in the control of movement, which include the motor cortex, basal ganglia, cerebellum, and motor nuclei of the brainstem (Rizzolatti and Luppino 2001, Groenewegen 2003, Glickstein and Doron 2008). The control of movement encompasses multiple movement-related activities, such as motor planning, motor coordination, and motor learning. The motor system interacts with the muscular system via peripheral motor neurons at the neuromuscular junction (Darabid et al. 2014). At the neuromuscular junction, synaptic release of the neurotransmitter acetylcholine causes contraction of muscle fibers, which increases muscle tension and generates movement (Darabid et al. 2014). Clinically, it is useful to differentiate between lower motor neurons (LMNs) and upper motor neurons (UMNs) (Rekand 2010). LMNs, found in cranial nerve nuclei and the anterior horn of the spinal cord, are the neurons that directly innervate skeletal muscle fibers (Stifani 2014). LMNs receive input from UMNs, which typically have cell bodies in the motor cortex and brainstem (Stifani 2014). The activity of LMNs is influenced both by these excitatory UMNs and by mostly inhibitory interneurons located within the brainstem and spinal cord (Stifani 2014). UMNs are in turn influenced by complex interactions between various motor areas in the cerebral cortex, subcortical structures, the brainstem, and the cerebellum. Functionally and anatomically, the motor system can be divided into two main components – the pyramidal and extrapyramidal motor systems.

Pyramidal motor system

The pyramidal motor system consists of descending motor tracts that pass through the pyramids of the medulla (Martin 2005). These include the corticospinal tract, which projects from the cerebral cortex to the spinal cord, and corticobulbar tract, which projects from the cerebral cortex to the brainstem (Keizer and Kuypers 1989). The corticospinal tract is the principal motor pathway in primates, especially for fine motor control of distal muscles (Lemon 2008). Pyramidal tract fibers often synapse directly onto motor neurons in the spinal cord and brainstem, in contrast to extrapyramidal pathways that are more involved in modulation of motor outputs.

The corticospinal tract consists of neurons whose cell bodies are located in layer V of the cerebral cortex and whose axons project to the spinal cord (Martin 2005). The majority of these neurons are located in the motor cortex, an area of the frontal lobe located anterior to the central sulcus (Rizzolatti and Luppino 2001). The motor cortex is divided into multiple cortical areas, the largest of which are the primary motor cortex (M1), the dorsal and ventral premotor cortex (PMd and PMv), and the supplementary motor area (SMA), which are shown in Figure 1.1 (Rizzolatti and Luppino 2001). About one third of corticospinal fibers originate in M1, and another third originate in the supplementary SMA, PMd, and PMv combined (Rizzolatti and Luppino 2001). The vast majority (~80-85%) of corticospinal axons cross midline at the decussation of the pyramids and form the lateral corticospinal tract, terminating on lower motor neurons and interneurons in the anterior horn of the contralateral spinal cord (Liu and Chambers 1964).

M1, located directly anterior to the central sulcus, contains many motor neurons that synapse directly on LMNs in the anterior horn of the spinal cord (Rizzolatti and Luppino 2001). PMd and PMv, located anterior to the M1 arm representation, are involved in planning and preparing for movement (Rizzolatti and Luppino 2001). SMA, located anterior to the M1 leg representation, is involved in internally generated movement, bimanual control, postural stability, and temporal sequences of actions (Rizzolatti and Luppino 2001). The corticospinal tract allows for fine voluntary movements and fractionated control of joints, with particular importance for control of the distal muscles of the contralateral limbs such as those for independent finger movements (Lawrence and Kuypers 1968).

The corticobulbar tract consists of motor cortex neurons whose axons project to the brainstem, including axons collaterals from corticospinal neurons (Keizer and Kuypers 1989). In addition to cranial nerve nuclei, which are analogous to motor pools in the spinal cord anterior horn, the brainstem contains the origins of multiple bulbospinal pathways. These are the pontomedullary reticular formation (PMRF), which gives rise to the reticulospinal tract; the red nucleus, which gives rise to the rubrospinal tract; and the vestibular nuclei, which give rise to the vestibulospinal tract (Lemon 2008). Corticobulbar pathways, such as the corticoreticular tract, are able to influence motor control via inputs to brainstem motor pathways (Ziemann et al. 1999).

Extrapyramidal motor system

The extrapyramidal motor system consists of motor pathways that do not travel through the medullary pyramids. These include the previously mentioned major brainstem motor pathways – the reticulospinal, vestibulospinal, and rubrospinal tracts – and regulatory components such as the basal ganglia and cerebellum. The basal ganglia are a network of subcortical nuclei involved in action selection and initiation of movement (Obeso et al. 2002). The main components of the basal ganglia are the striatum, which consists of the caudate nucleus and putamen; the globus pallidus, which is divided into internal and external portions; the substantia nigra, which is divided into the pars reticulate and the pars compacta; the nucleus accumbens; and the subthalamic nucleus (Obeso et al. 2002). The cerebellum, a region of the brain located inferior to the occipital lobe and posterior to the brainstem, is important in motor coordination (Thach et al. 1992). The cerebellum receives feedback from sensory systems and makes small adjustments to fine-tune body and limb movements (Thach et al. 1992). The reticulospinal tract, which originates in the reticular nuclei in the pons and medulla of the brainstem, is involved in the control of locomotion, postural stability, and voluntary movement (Lemon 2008). The vestibulospinal tract, which originates in the vestibular nuclei of the brainstem, is involved in maintaining posture and balance (Lemon 2008). The rubrospinal tract, which originates in the red nucleus of the midbrain, is involved in voluntary movement of the upper limbs, but is significantly smaller in humans compared to other primates (Lemon 2008).

Disorders of the motor system

Overview of motor system dysfunction

Motor system dysfunction affects over five million people in the United States (Borlongan et al. 2013, Lawrence et al. 2001, Nakayama et al. 1994). There are many causes of motor system dysfunction, shown in Table 1.1, but two of the most common causes are stroke and Parkinson's disease (PD). About 77% of stroke patients report weakness or paralysis (Lawrence et al. 2001, Nakayama et al. 1994). Because stroke causes injury to the motor cortex, it primarily affects the pyramidal motor system, resulting in UMN lesion symptoms like loss of fine motor control, weakness, and paralysis. In contrast, PD affects the extrapyramidal system, involving deficits in the initiation of movement and motor coordination (Davie 2008).

Unilateral motor cortex injury and hemiparetic stroke

The MCA, a branch of the internal carotid artery, is the most common site of occlusion in ischemic stroke (Ng et al. 2007). One reason for the high rate of motor impairment in stroke is that the MCA supplies blood to most of the motor cortex. Occlusion of the MCA results in insufficient blood flow to the lateral cerebral cortex leading to cell death in affected areas. Because the corticospinal tract descends primarily contralaterally, these deficits affect the opposite (contralateral) side of the body as the cortical lesion. The medially located M1 leg representation is supplied primarily by the anterior cerebral artery, resulting in sparing of lower limb motor control following MCA stroke (de Freitas et al. 2000). However, since the more laterally located M1 arm representation is supplied by the MCA, upper limb motor control is less commonly spared. As a result, deficits in reaching and other arm movements represent a large contribution to post-stroke morbidity.

Disorders of the basal ganglia

PD is the second most common neurodegenerative disorder, second only to Alzheimer's disease. About one million (1 in 300) people in the U.S. have PD (de Lau and Breteler 2006). PD is caused by degeneration of dopaminergic neurons in the substantia nigra (Davie 2008). This degeneration of substantia nigra neurons in PD is histologically associated with intracellular aggregations of alpha-synuclein and other proteins, called Lewy bodies (Davie 2008). This loss of substantia nigra neurons has widespread effects through the basal ganglia, as shown in Figure 1.2, leading to a characteristic set of motor symptoms – tremor, hypokinesia, rigidity, and postural instability – known as parkinsonism (Gelb 1999, Davie 2008).

PD is part of the group of movement disorders of basal ganglia origin, which also includes Huntington's disease, Sydenham's chorea, and hemiballismus (Obeso et al. 2002). Although the etiology of these movement disorders is varied, they all involve damage to basal ganglia circuitry. As previously stated, PD is caused by loss of dopaminergic neurons in the substantia nigra pars compacta (Davie 2008). Huntington's disease is a caused by trinucleotide expansion in the Huntingtin gene, which disproportionately affects striatal neurons (Walker 2007, Eidelberg and Surmeier 2011). Sydenham's chorea is caused by an autoimmune-mediated destruction of striatal neurons following group A β-hemolytic streptococci infection (Swedo et al. 1993). Hemiballismus can result from various conditions resulting in damage to the subthalamic nucleus (Postuma and Lang 2003). Because the basal ganglia are involved in the initiation of movement, these movement disorders lead to either insufficient or excessive movement.

Clinical correlates

Impairment and recovery following hemiparetic stroke

Because the majority of corticospinal axons descend contralaterally, unilateral loss of motor cortex neurons results in primarily contralateral hemiparesis. This is reflected in decreased corticomuscular signal coupling between EEG and EMG in stroke patients compared to healthy controls (Fang et al. 2009). Other deficits observed post-stroke are prolonged cognitive planning time, elevated cognitive effort, impaired coordination and motor control, and delays in initiation and termination of muscle contractions (Daly et al. 2006, Chae et al. 2002). Patients exhibit the loss of fractionated, or independent, control of joints (Ellis et al. 2012, Yao et al. 2009). Following hemiparetic stroke, patients exhibit abnormal muscle coactivation patterns during isometric torque generation at the elbow and shoulder (Dewald et al. 1995). In addition, they display deficits in the coordination of multi-joint arm movements indicating disturbed control of limb dynamics (Levin 1996, Beer et al. 2000, Daly et al. 2007). With rehabilitation therapy, functional recovery is usually complete by 20 weeks poststroke for all degrees of initial stroke severity (Twitchell 1951, Jorgensen et al.

1995). Encouraging use of the impaired arm by restraining the unaffected arm was shown to effectively promote the recovery of motor function in stroke patients with chronic motor impairment (Taub et al. 2006).

Differential diagnosis of parkinsonism

While PD is the most common parkinsonian syndrome, the differential diagnosis of parkinsonism is complicated by the existence of atypical parkinsonian syndromes (APS), or Parkinson-plus syndromes, which also exhibit classical parkinsonian symptoms, but include additional features distinguishing them from idiopathic PD (Jankovic 2008). Because of these overlapping symptoms, APS are especially difficult to differentiate from PD. The most common APS are multiple system atrophy (MSA), progressive supranuclear palsy (PSP), and corticobasal degeneration (CBD) (Jankovic 2008). One in ten patients diagnosed clinically with early PD are later shown to have functional imaging scans without evidence of dopaminergic deficit (SWEDDs) (Schwingenschuh et al. 2010). Improved diagnostic methods will result in earlier detection of disease, allowing patients to be treated sooner.

The development of various clinical examinations and neuroimaging analyses has increased the quantity of clinical data available for diagnosis of movement disorders. With increasing amounts of diagnostic data available to clinicians, it becomes increasingly difficult for physicians to generate, internalize, and apply accurate medical algorithms. Computer-aided diagnosis (CAD) can improve the diagnostic accuracy by incorporating precise clinical values and performing complex calculations to determine the probability of competing diagnoses. In addition to improvements in accuracy, CAD has been shown to detect early stages of disease with greater sensitivity (Freer and Ulissey 2001).

Research objectives

The corticospinal pathway is central to fine motor control of voluntary movement in healthy primates (Lemon 1993). As a result, much of motor systems research has focused on this system. However, clinical evidence has indicated an important function of the reticulospinal system in stroke patients (Dewald et al. 1995, Dewald and Beer 2001, Ellis et al. 2007, Ellis et al. 2012). Despite this importance, many aspects of the reticulospinal system remain inadequately understood (Jang 2012). The first objective of this dissertation is to determine the EMG and force outputs of reticulospinal neurons using a novel technique to record force responses evoked by spontaneous spiking and electrical stimulation in the PMRF. We hypothesize that EMG and force outputs of reticulospinal neurons can be detected using stimulus-triggered averaging (StimulusTA) and spike-triggered averaging (SpikeTA). It is expected that EMG and force responses will exhibit a double reciprocal pattern of activity characterized by flexion of the ipsilateral arm and extension of the contralateral arm relative to the PMRF stimulation or recording site.

Using diagnostic criteria promoted by the National Institute of Neurological Disorders and Stroke (NINDS), PD diagnosis only achieves diagnostic certainty of 57-90% (Gelb et al. 1999, Jankovic 2008). Improvements to these criteria require probabilistic inferences from large collections of data, including clinical signs and symptoms, neuroimaging scans, and laboratory test results (Jankovic 2008). With increasing amounts of medical information and increasing usage of electronic medical data, there is a growing role for CAD. The second objective of this dissertation is to identify an accurate machine learning algorithm for differentiating between patients with PD, SWEDDs, and healthy controls. Furthermore, by determining which data are most predictive of disease state, novel clinical features of and associations between PD and SWEDDs may be identified. We hypothesize that PD, SWEDDs, and healthy subjects will be able to be accurately classified using machine learning algorithms based on clinical and neuroimaging features. It is expected that the enhanced probabilistic neural network will exhibit the highest classification accuracy. Furthermore, non-motor function is expected to be better able to differentiate between PD and SWEDDs than motor function.

Tables & Figures

Motor system injury			2.7%
	Cortical injury		
		Stroke	
		Traumatic brain injury	
	Spinal cord injury		
Movement disorders			0.3%
	Parkinsonian syndromes		
		Parkinson’s disease	
		Atypical parkinsonian syndromes	
	Huntington’s disease		
Hemiballismus			
Motor neuron disorders			< 0.1%
	Amyotrpohic lateral sclerosis (ALS)		
	Spinal muscular atrophy (SMA)		
	Guillain-Barre syndrome (GBS)		
	Charcot-Marie-Tooth disease (CMT)		
Multiple Sclerosis			< 0.1%
Cerebral Palsy			< 0.1%

Table 1.1 Prevalence of the leading causes of motor system dysfunction in the United States. The most common causes are stroke and other brain and spinal cord injuries, followed by PD (Borlongan et al. 2013, Lawrence et al. 2001, Nakayama et al. 1994).

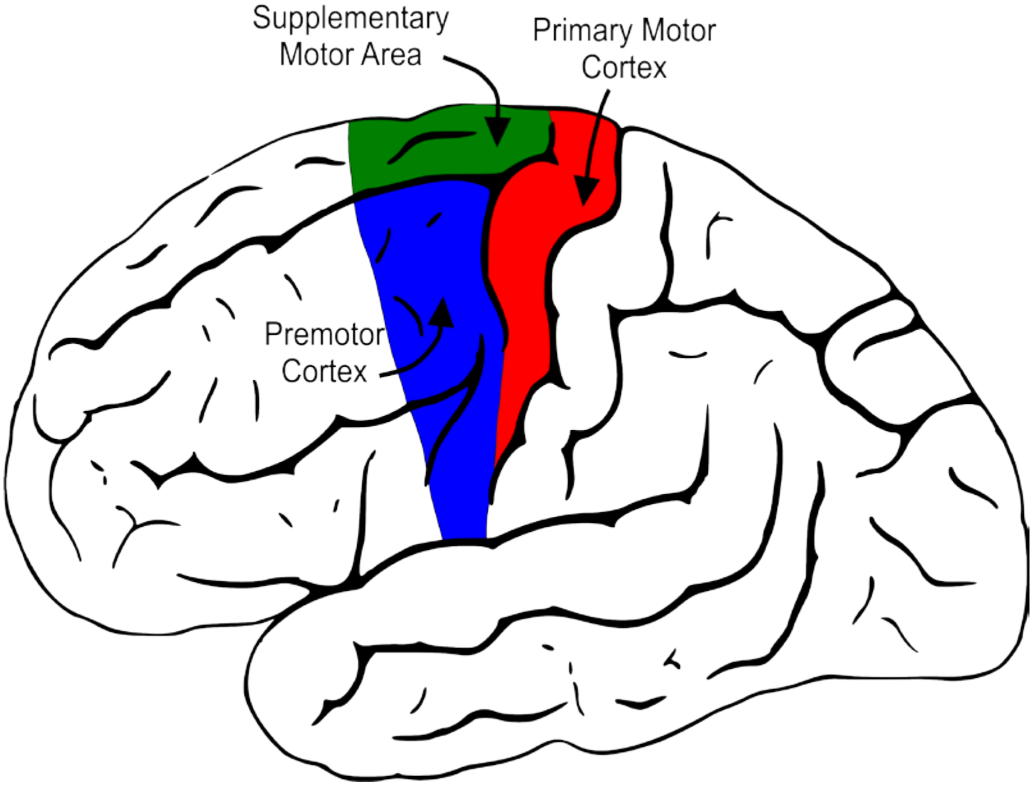

Figure 1.1 Lateral view of a human brain displaying the areas of the motor cortex. The primary motor cortex (M1) is located directly anterior to the central sulcus (shown in red). The premotor cortex (PMd and PMv) is located anterior to the lateral portion of M1 (shown in blue). The supplementary motor area (SMA) is located dorsal to PMd and extends into the medial longitudinal fissure (shown in green). Adapted from Gray (1918).

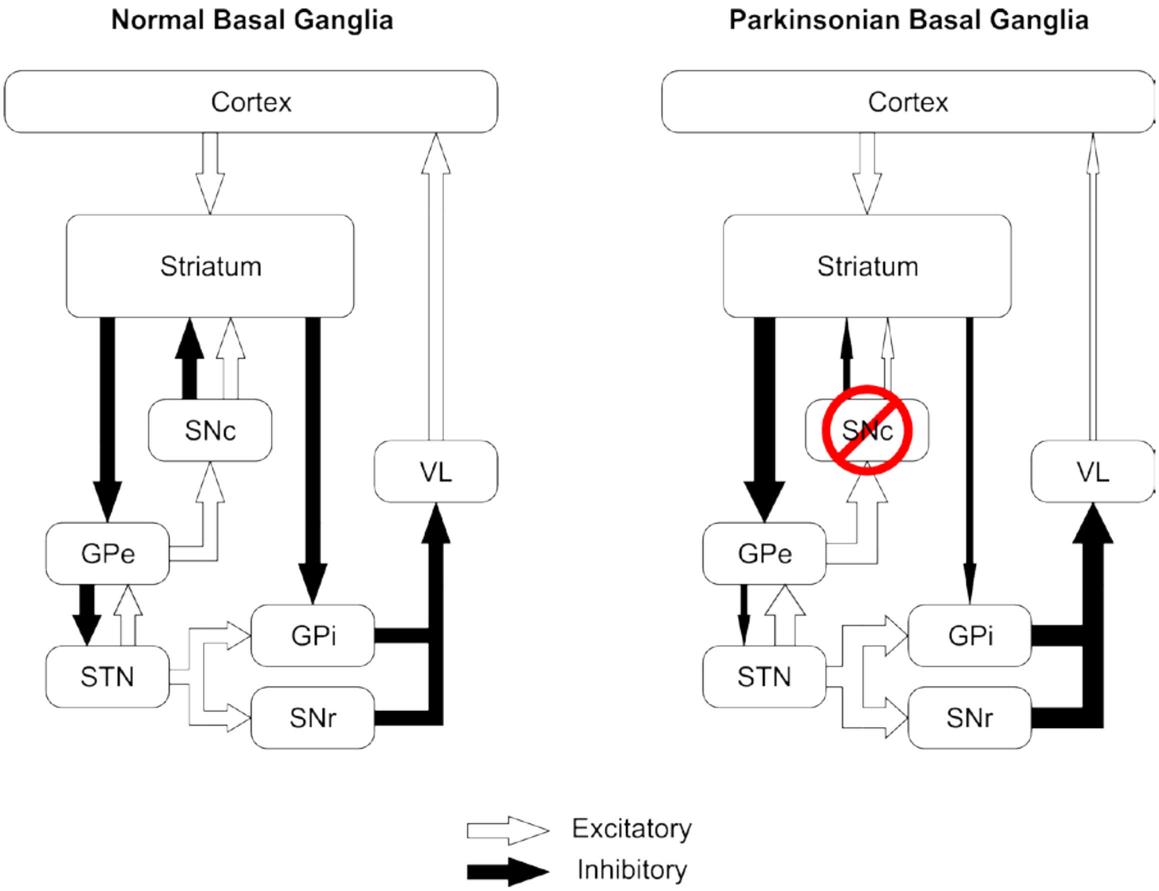

Figure 1.2 A comparison of normal and PD motor circuits. PD subjects have a loss of dopaminergic neurons in the substantia nigra pars compacta (SNc), decreasing the amount of dopamine delivered to the putamen (Obeso et al. 2002). Open arrows represent excitation, filled arrows represent inhibition. *GPi*, internal globus pallidus; *GPe*, external globus pallidus; *SNc*, substantian nigra pars compacta; *SNr*, substantia nigra pars reticulata; STN, subthalamic nucleus; *VL*, ventral lateral nucleus of the thalamus.

Chapter 2: Review of the anatomy and physiology of the reticulospinal system

Bilateral projections of reticulospinal neurons

The reticulospinal tract, which originates in the PMRF, is a major descending motor pathway (Kuypers 1958, 1981; Peterson et al. 1974, 1975, 1979). The main targets of reticulospinal axons are interneurons in lamina VII and VIII and motor neurons in lamina IX that primarily innervate axial and proximal limb muscles (Grillner and Lund 1966, 1968; Jankowska et al. 2003; Matsuyama et al. 1997; Peterson et al. 1979). However, recent studies have also shown reticulospinal activation of distal limb muscles, including muscles of the hand (Soteropoulos et al. 2012).

The reticulospinal tract, like the corticospinal tract, contains both monosynaptic and polysynaptic projections to axial and upper limb motor neurons (Peterson et al. 1979). However, in contrast to the corticospinal tract, which projects primarily *contralaterally*, the reticulospinal tract projects primarily *bilaterally* to spinal motor neurons and interneurons (Keizer and Kuypers 1989, Sakei et al. 2009). Within the PMRF, the gigantocellular reticular nucleus has more ipsilateral projections than contralateral (Sakei et al. 2009). Stimulation of this region produces excitation of ipsilateral upper limb motor neurons more often than contralateral (Peterson et al. 1979).

Reticulospinal axons that descend ipsilaterally are able to produce contralateral effects through commissural interneurons and decussating axon collaterals (Bannatyne et al. 2003; Jankowska et al. 2003; Sakai et al. 2009, Szokol et al. 2011). Stimulation studies have demonstrated functional connections indicating widespread bilateral projections. In the cat, short stimulus trains were used to elicit reticulospinal recruitment of axial and proximal limb muscles bilaterally (Drew and Rossignol 1990a, 1990b; Schepens and Drew 2006; Sprague and Chambers 1954). A reciprocal motor output pattern was observed following stimulation, characterized by ipsilateral limb flexion, contralateral limb extension, and head rotation toward the ipsilateral side (Sprague and Chambers 1954). Stimulus trains in the monkey PMRF have reproduced the same motor pattern in the upper limb (Herbert et al. 2010). Motor outputs of stimulus trains have exhibited high agreement with those of stimulus-triggered averaging (StimulusTA) of single-pulse microstimulation (Herbert et al. 2010). StimulusTA studies in the monkey have revealed a double reciprocal pattern of EMG activity from upper limb muscles, consisting of facilitation of ipsilateral flexors and contralateral extensors and suppression of ipsilateral extensors and contralateral flexors (Davidson and Buford 2004, 2006). These bilateral outputs to proximal limb muscles make the reticulospinal system well-suited to coordinate bilateral limb movement (Kuypers 1958, 1981; Peterson et al. 1974, 1975, 1979).

Reticulospinal control of movement

The reticulospinal system, one of the evolutionarily oldest descending pathways, is the primary circuit involved in supraspinal control of locomotion in vertebrates (Drew et al. 2004, Matsuyama et al. 2004). In the lamprey, activity of reticulospinal neurons initiates swimming (Grillner 2003, Ménard and Grillner 2008). In the cat, reticulospinal neurons are modulated in phase with rhythmic muscle activity during locomotion (Drew et al. 1986, Matsuyama and Drew 2000). Stimulation of the mesencephalic locomotor region (MLR), which projects to neurons in the reticular formation, is sufficient to produce locomotion with intensity-dependent gait patterns (Shik et al. 1966). During gait modifications, reticulospinal neurons exhibit coinciding changes in discharge activity (Matsuyama and Drew 2000, Prentice and Drew 2001).

The existence and function of the MLR has been identified in many vertebrate species, including the lamprey (McClellan and Grillner 1984), the rat (Garcia-Rill et al. 1990), the rabbit (Corio et al. 1993), the cat (Shik et al. 1966), and the monkey (Eidelberg et al. 1981). There are significant homologies between the brainstem and midbrain postural and locomotor control structures of primates and other animals (Mori et al. 1996). While homologies in locomotor control systems exist between primates and other vertebrates, locomotion generators in the monkey depend more on supraspinal inputs than those in the cat (Eidelberg et al. 1981). Clinical studies point to the existence of similar locomotor control regions in humans, known as the pedunculopontine nucleus (PPN) (Caplan and Goodwin 1982; Masdeu et al. 1994; Zweig et al. 1987; Hanna and Frank 1995; Garcia-Rill 1985).

In addition to locomotion, the reticulospinal pathway is also involved in head movement for gaze control (Cowie and Robinson 1994, Cowie et al. 1994). Electrophysiological studies demonstrated that stimulation of the gigantocellular reticular nucleus produced ipsilateral head movements (Cowie and Robinson 1994).

Complementary tract tracing studies identified gigantocellular reticular nucleus efferents that projected to motor nuclei of the head and neck (Cowie et al. 1994).

Reticulospinal pathways are also involved in postural stability, which could account for the greater number of projections to axial and proximal limb muscles (Bolton et al. 1992, Eccles et al. 1975, Matsuyama and Drew 2000). Lesions of both the brainstem (Kuypers 1964; Lawrence and Kuypers 1968) and spinal regions containing reticulospinal tract (Afelt 1974; Bem et al. 1995; Brustein and Rossignol 1998; Eidelberg et al. 1981; Gorska et al. 1990, 1993) result in postural deficits, indicating reticulospinal involvement. Similarly, injection of acetylcholine receptor agonists into the PMRF results in impaired postural responses during voluntary limb movement (Luccarini et al. 1990; Sakamoto et al. 1991).

More recently, the reticulospinal system has been shown to be involved in voluntary limb movements (Buford and Davidson 2004). In the cat, reticulospinal neurons were modulated during postural adjustments and reaching movements (Schepens et al. 2004, 2006, 2008). In the monkey, reticulospinal neurons were shown to be modulated during voluntary reaching (Buford and Davidson 2004) and during finger movement (Soteropoulos et al. 2012). It is thought that the same reticulospinal pathways involved in locomotion are also activated during reaching (Drew et al. 2004).

Cortical and subcortical projections to PMRF

The basal ganglia are involved in the initiation of movement, as demonstrated by disorders like PD, which can cause akinesia. Classically, the basal ganglia have been thought to influence locomotion by a corticostriatocortical pathway that travels from the cortex to the striatum and back to the cortex via the thalamus (Alexander et al. 1986). However, the loss of spontaneous initiation of locomotion in the postmammillary cat, but not in the premammillary cat, implies the involvement of direct projections from the basal ganglia to the MLR (Garcia-Rill et al. 1983, 1986). Furthermore, stimulation in the substantia nigra delayed locomotion onset, increased step cycle time, and disturbed stepping rhythm (Takakusaki et al. 2003).

In addition to subcortical pathways, there exist cortical pathways from motor cortex neurons that project directly to the reticular formation via corticoreticular efferents (Keizer and Kuypers 1989). In the cat, cortical projections from M1 to the PMRF were mostly through corticospinal axon collaterals, but the cortical projections from premotor cortex and SMA were mostly direct (Kably and Drew 1998). In the monkey, transcranial magnetic stimulation (TMS) evoked short-latency responses from neurons in the PMRF (Fisher et al. 2012). In humans, voluntary movements are initiated with reduced premotor reaction times when the imperative stimulus to initiate movement is replaced by a startling acoustic stimulus (Valls-Sole et al. 1995, 1999, 2008). Additionally, TMS over the motor cortex delayed this early release of movement caused by acoustic startle (Alibiglou and MacKinnon 2012). Furthermore, the corticoreticular connections thought to mediate this effect, projecting from premotor cortex to the PMRF, have been identified using diffusion tensor tractography (Yeo et al. 2012).

Motor impairment following unilateral stroke

The primary motor deficit following unilateral motor cortex stroke is weakness affecting the opposite side of the body, called contralateral hemiparesis. In addition to weakness, unilateral UMN lesions like stroke often present with spasticity, hyperreflexia, and hemiplegia. A pattern known as pyramidal weakness is common, which includes greater weakness in upper limb extensors and lower limb flexors (Cheney et al. 1991, Thijsa et al. 1998). Motor impairment is generally most severe immediately following stroke with initial improvement evident within weeks of the stroke (Partridge et al. 1987, Bonita and Beaglehole 1988). Some rehabilitation techniques such as physical therapy, repetitive task training, and biofeedback have been shown to be effective at enhancing motor recovery (Langhorne et al. 2009).

Many studies have examined other motor deficits in hemiparetic stroke patients. Some of the deficits observed alongside hemiparesis are cognitive difficulty in generating movement and impaired motor control (Daly et al. 2006, Chae et al. 2002). Of particular note, certain motor symptoms demonstrate the importance of reticulospinal function after stroke. For instance, stroke subjects show deficits in the coordination of multi-joint arm movements indicating disturbed control of limb dynamics (Levin 1996, Beer et al. 2000, Daly et al. 2007). Similarly, stroke patients exhibit abnormal muscle coactivation patterns during isometric torque generation at the elbow and shoulder (Dewald et al. 1995, Dewald and Beer 2001; Ellis et al. 2007). This loss of fractionated joint control is thought to be caused by increased reliance on the reticulospinal system (Ellis et al. 2012).

Another line of evidence supporting this concept is related to the asymmetric tonic neck reflex (ATNR), a primitive reflex thought to be mediated by the PMRF (Brink et al. 1985; Srivastava et al. 1984). The ATNR is characterized by a classic “fencing” posture, with ipsilateral arm flexion and contralateral arm extension, similar to the motor pattern evoked by PMRF stimulation (Davidson and Buford 2004, 2006; Ellis et al. 2012). The ATNR is normally suppressed in the adult nervous system, but often reemerges following stroke, indicating increased reticulospinal excitability (Ellis et al. 2012). The acoustic startle reflex, also mediated by brainstem pathways, is similarly increased following stroke (Brown et al. 1991, Li et al. 2014).

Reticulospinal mediated functional recovery

Motor recovery after stroke is mediated by brain reorganization, which can be enhanced with rehabilitation techniques like constraint-induced movement therapy (Krakauer 2005, Mark and Taub 2004). Studies have detected reorganization in both the ipsilesional and contralesional motor cortices (Krakauer 2005). The nature of this reorganization is thought to include unmasking of latent synapses, facilitation of alternative networks, synaptic remodeling, and axonal sprouting. (Hallett 2001, Elbert and Rockstroh 2004, Bütefisch 2004, Ward 2004)

The contralesional motor cortex has been shown to play a role in functional reorganization during stroke recovery. Stroke patients with normal motor examinations showed increased contralesional motor activation (Krakauer et al. 2004). TMS applied to the contralesional PMd caused an increase in reaction time in the stroke patients but not controls, with the magnitude of the increase significantly correlated with the degree of motor impairment (Johansen-Berg et al. 2002). In addition, multiple cases have been described in which patients with good recovery after stroke-induced hemiparesis subsequently lost function in both ipsilaterally and contralaterally after a stroke to the opposite hemisphere (Fisher 1992, Ago et al. 2003).

Because the contralesional motor cortex is ipsilateral to the affected limbs, the corticospinal pathway, which projects contralaterally, is not ideally situated to mediate recovery (Soteropoulos et al. 2011). In contrast, the reticulospinal system, because of its bilateral pattern of projection to the upper limbs, has been considered a candidate pathway for alternative motor control of the impaired limb after stroke (Jankowska and Edgley 2006, Ellis et al. 2012). Reticulospinal neurons receive inputs from corticospinal fiber collaterals from both the ipsilateral and contralateral motor cortex (Keizer and Kuypers 1984, 1989; Ugolini and Kuypers 1986; Matsuyama and Drew 1997; Kably and Drew 1998). Electrical stimulation of cortical neurons has been shown to evoke excitatory postsynaptic potentials in reticulospinal neurons (Magni and Willis 1964, Peterson et al 1974, He and Wu 1985, Canedo and Lamas 1993).

Several studies support the ability of motor cortex to exert motor effects through a cortico-reticulospinal circuit (Baker et al. 2015). In the cat, lesion of the pyramidal tract demonstrated cortical actions transmitted via reticulospinal neurons (Alstermark et al. 1985, Edgley et al. 2004). Stimulation of the motor cortex has been shown to evoke postural adjustment in the ipsilateral and contralateral forelimbs, which is thought to be mediated by a corticoreticular pathway (Gahéry and Nieoullon 1978). Functional recovery after stroke cannot be explained by ipsilateral corticospinal pathways alone (Palmer et al. 1992). After corticospinal tract lesion in the monkey, there was an increase in motor responses to stimulation of the reticulospinal tract but not to stimulation of the ipsilateral corticospinal tract (Zaaimi et al. 2012). Additionally, this increase was observed in forelimb flexors and not extensors, matching symptoms of pyramidal weakness common after stroke (Zaaimi et al. 2012). In humans, TMS of the motor cortex has been shown to yield responses in the ipsilateral limb (Ziemann et al. 1999, Alagona et al. 2001). In stroke patients, these responses to TMS are stronger and evoked at lower thresholds than those in healthy controls (Alagona et al. 2001). These responses have been shown to depend on head rotation, indicating involvement of the same reticulospinal pathway that mediates the ATNR (Ziemann et al. 1999, Tazoe and Perez 2014). Reticulospinal involvement is most common in lesions with little corticospinal sparing (Turton et al. 1996).

Based on the output of the reticulospinal tract, there are likely two major corticoreticular pathways that could mediate cortical control of ipsilateral muscles. The first is corticoreticular projections to *ipsilateral* reticulospinal neurons that project to ipsilateral spinal motor nuclei, and the second is corticoreticular projections to *contralateral* reticulospinal neurons that descend ipsilaterally with respect to the reticular nuclei and terminate on commissural interneurons in the spinal cord that synapse on neurons in the contralateral motor nuclei (with respect to the reticular nuclei).

Motor outputs of reticulospinal neurons

To adequately understand the function of the reticulospinal system in both healthy people and those recovering from stroke, it is necessary to determine the motor effects of a reticulospinal neuron in a physiological setting. Previous studies have identified changes in EMG activity evoked by electrical stimulation in the PMRF, but because of the extensive branching of reticulospinal axons which causes effects in many muscles, it is difficult to infer what effects this activity will have on movement (Davidson and Buford 2004, 2006). No studies have been performed to identify the movements or force outputs associated with physiological levels of neural activity in the PMRF. By recording spontaneous spiking or evoking spiking through electrical stimulation while simultaneously recording EMG and forces, the effect of PMRF neurons on the upper limb muscle activity and movement could be determined.

Chapter 3: Stimulus-triggered averaging of reticulospinal motor outputs evoked by single-pulse microstimulation

Introduction

Although they primarily descend ipsilaterally, reticulospinal axons produce contralateral effects through commissural interneurons and decussating axon collaterals (Bannatyne et al. 2003; Jankowska et al. 2003; Sakai et al. 2009). Microstimulation studies in the monkey in the monkey PMRF using short stimulus trains have produced reciprocal patterns of ipsilateral upper limb flexion and contralateral extension (Herbert et al. 2010), similar to previously observed patterns in the cat (Sprague and Chambers 1954). Motor outputs of stimulus trains have exhibited high agreement with those of stimulus-triggered averaging (StimulusTA) of single-pulse microstimulation (Herbert et al. 2010). StimulusTA studies in the monkey have revealed a double reciprocal pattern of EMG activity from upper limb muscles, consisting of facilitation of ipsilateral flexors and contralateral extensors and suppression of ipsilateral extensors and contralateral flexors (Davidson and Buford 2004, 2006).

Spike-triggered averaging (SpikeTA) is considered to be the most direct method of investigating motor outputs in electrophysiological studies. The major motor effects revealed by SpikeTA are thought to be primarily mediated through monosynaptic and disynaptic connections to motor neurons (Cheney and Fetz 1985; Baker and Lemon 1998; Davidson et al. 2007). StimulusTA is also thought to activate monosynaptic and disynaptic pathways, but with a larger number of neurons engaged (Cheney and Fetz 1985). StimulusTA and SpikeTA from the same recording sites in the motor cortex and PMRF exhibit similar EMG activity (Cheney and Fetz 1985; Davidson et al. 2007). These findings support the view that StimulusTA reveals the output of reticulospinal neurons through relatively direct pathways which more accurately depict the physiological effects of PMRF neural activity than trains of stimuli.

To our knowledge, no SpikeTA or StimulusTA studies have investigated the movements and force outputs resulting from motor activity within the central nervous system. There have been multiple studies, however, that have investigated the relationship between neural activity and force. Evarts (1968) devised one of the first single unit recording studies to determine whether primary motor cortex neuron activity related to force or displacement. Over time, investigators have devised analytical approaches to extract correlates of force, velocity, and position signals from neural activity in cortical motor areas (Georgopoulos et al. 1992, Ashe 1997, Moran and Schwartz 1999). However, in the reticulospinal system, no comparable studies exist. In cats standing on force platforms, reticulospinal motor outputs were associated with stereotyped force output patterns for postural adjustments (Gahéry et al. 1980), but there have been no purely upper limb studies relevant to reaching where forces were measured.

The purpose of this study was to determine the force effects of PMRF motor output evoked with single-pulse stimuli by using the StimulusTA approach to measure forces in addition to EMG activity. Despite the small magnitude of previously detected post-stimulus EMG effects, we expected measureable forces to be exerted by the upper limbs in response to PMRF stimulation. Furthermore, we expected the pattern of forces to correspond to the double reciprocal pattern of EMG activity associated with PMRF output. Demonstrating the effectiveness of this novel technique for measuring motor outputs could have broad applications for motor systems neurophysiology by permitting direct measurement of force outputs evoked by CNS microstimation. This would allow for identification of physiologically relevant force effects of CNS neural activity.

Methods

Subjects, task, and surgery

Two male monkeys (*Macaca fascicularis*) were trained to perform a bilateral isometric force control task administered by Tempo software (Reflective Computing, Olympia, WA, USA). Subjects sat in a primate chair with their head restrained and simultaneously controlled two cursors on a computer screen via two stationary force-sensitive joysticks. The joysticks were located at waist level, so during the task both the subject's arms were positioned much like a person's would be to hold a gearshift in a car. The subjects tended to grip the joysticks with their palms down and their forearms pronated. Each hand controlled one cursor via a single joystick, as shown in Fig. 1. Cursors were primarily controlled by pushing and pulling along the anteroposterior y-axis, also shown in Fig. 1. A trial began once the subject was holding both joysticks with the cursors within the range of two central targets corresponding to zero y-direction force. Once this starting position was held for 1.0 s, targets appeared indicating the necessary forces that must be applied to complete the task. The subject had to push or pull on each joystick to move the cursors to the targets. Once the cursors were on targets, that effort had to be maintained for 0.5 s. This was implemented as a simple reaction time task, with the subject free to begin the effort to move the cursors as soon as the targets appeared. Pushing or pulling forces of approximately 30 N were required to hold the cursors on the targets. The next trial could be initiated after a 1.0 s reward period; the subject self-paced the start of the next trial. Within each session, the trial types were presented in a pseudorandomized order. The start positions were in the center left and center right of the screen for the left and right joysticks. For each arm, the target positions were either directly above the start position (for a trial requiring pushing) or directly below it (for a trial requiring pulling). Two targets appeared for each trial type (one for each arm), in one of 4 possible combinations.

Surgical procedures for implanting the recording chamber and EMG electrodes were similar to those provided in previous reports (Davidson and Buford 2004, 2006). A stainless steel recording chamber was mounted to the skull over a craniotomy of the left parietal bone and secured with bone screws and dental acrylic. The center of the recording chamber was directed toward Horsley-Clark stereotaxic coordinates anteroposterior (AP) 0, mediolateral (ML) 0, dorsoventral (DV) -12, allowing bilateral access to the PMRF (Szabo and Cowan 1984). The chamber was tilted approximately 10° laterally to avoid penetration of midline vascular structures. EMG electrodes consisted of pairs of multi-stranded, Teflon-coated stainless steel wires that were led subcutaneously from the cranial implant to the electrode implant sites. Insulation was removed from the last 2 mm of the tips of the wires, which were inserted intramuscularly with a hypodermic needle (Betts et al. 1976; Park et al. 2000). Twelve bilateral arm and shoulder muscle pairs were implanted for a total of 24 muscles. The implanted muscles with their functions and abbreviations are presented in Table 1.

Subject care complied with the NIH Guide for the Care and Use of Laboratory Animals and the institutionally approved animal care protocol for our laboratory. Surgeries were performed under veterinary supervision in aseptic conditions. Animals were pretreated with antibiotics and anesthetized with ketamine HCl (13 mg/kg IM) followed by isoflurane gas (1-2%) through endotracheal intubation. While under anesthesia, the subject’s respiration, heart rate, and body temperature were monitored. Antibiotics and non-steroidal anti-inflammatory analgesics (e.g., buprenorphine, ibuprofen) were administered postoperatively to prevent infection and discomfort.

Stimulation procedures

Microstimulation was delivered by polyimide- and epoxy-insulated tungsten microelectrodes (Frederick Haer and Co, Bowdoin, ME, USA). Electrodes were inserted through a 23-gauge thin-walled stainless steel guide cannula, which was aligned with stimulation sites by placement through a two-dimensional grid in the recording chamber. Guide tubes were advanced into the brain and stopped a few millimeters into the cerebellum. The electrode was lowered through the guide tube and into the brainstem with a manual hydraulic microdrive.

A total of 311 stimulation sites from 83 penetrations were located throughout the PMRF, which is bounded by the abducens nucleus dorsally, the inferior olive and pyramidal tract inferiorly, and the facial nucleus laterally. The abducens nucleus was identified during electrode insertion by recordings from cells with firing rates proportional to ipsilateral eye abduction (Fuchs and Luschei 1970). Prior to stimulation, electrophysiological activity was recorded as the electrode was inserted to its maximal depth. As the electrode was retracted, stimulation was applied at 0.5 mm intervals to regions in which task-related neural activity had been detected.

At each StimulusTA site, 2000 biphasic pulses were delivered at a rate of 5 Hz by a digital stimulus controller (Master-8, AMPI, Israel) connected to an analog stimulus isolator (Model 2200, AM-Systems, Carlsborg, WA, USA). A stimulus current of 30 µA was used unless this current level produced observable muscle twitches or movement, in which case the current was reduced in 5 µA increments until the response was no longer visible. A default current of 30 µA was chosen because previous studies in PMRF output indicate this is an effective stimulus intensity for StimulusTA in the cat (Drew and Rossignol 1990a, 1990b) and monkey (Cowie and Robinson 1994; Davidson and Buford 2004, 2006; Herbert et al. 2010). While some stimulus currents were as low as 10 µA, the vast majority of currents were 30 µA (> 95%). For each session, stimulation was delivered continuously for 400 s throughout all phases of the task and regardless of subject behavior. Both subjects appeared to be unaware of this background stimulation.

EMG recording

Electromyographic data were collected from 12 pairs of chronically-implanted intramuscular electrodes. The electrode wires were led subcutaneously to three 17-pin plugs (WPI #223-161) mounted in the dental acrylic of the cranial implant. The integrity of the EMG implants was verified by periodic testing of electrode impedances. For both subjects, electrodes were located in both the left and right of 12 pairs of upper limb muscles, listed in Table 1. EMG activity was recorded at a sampling rate of 4 kHz with 20-2000 Hz band-pass filtering from all implanted muscles during stimulation using Spike2 software and a Power 1401 data acquisition unit (CED, Cambridge, England). A template subtraction algorithm removed EKG artifact prior to processing.

Force recording

Bilateral forces were recorded using two stationary, force-sensitive joysticks, which the subjects were trained to grasp. To maintain an isometric condition, the joysticks measured the magnitude and direction of forces applied by the subject, but did not move. The joysticks consisted of a ball handle on top of a shaft screwed into the mounting site of a 6 degree-of-freedom load cell (Gamma Model, ATI Industrial Automation, Apex, NC, USA). The single-trial resolution of the load cells was 3.5 mN, which was subsequently improved by signal averaging. Each load cell output controlled the movement of its respective cursor on the display screen. Force measurements were sampled at 4 kHz along the x-, y-, and z-axes from each joystick, shown in Fig. 1. Force response vectors were calculated using simple vector addition of the axial components. Force measurements were recalibrated for each recording session by defining the average force of periods in which the subject was not contacting the joysticks to be 0 N. The firmware in the controller for the load cell was supplied parameters about the length of the joystick so that output readings were calibrated for the point of force application.

EMG averaging and analysis

Procedures for compiling StimulusTAs of EMG data have been previously described in detail (Davidson and Buford 2006; Herbert et al. 2010). Briefly, for each muscle, EMG records were adjusted to remove DC offsets, rectified, and averaged off-line using custom scripts for Spike2 and MATLAB. Averages were compiled over an 80 ms window with a 20 ms pre-stimulus period and a 60 ms post-stimulus period. Triggers were selected for averaging only if the mean EMG of the 80 ms window was at least 10% greater than the peak baseline noise (McKiernan et al. 1998). Periods during which the EMG level exceeded the maximum amplifier range (4.5 V) were also excluded. As a result, the number of stimulus triggers varied for the StimulusTA of each muscle, with a typical analysis including more than 1900 triggers. A minimum of 500 triggers were required for a StimulusTA to be included in the analysis (McKiernan et al. 1998).

To test for post-stimulus EMG effects, multiple fragment statistical analysis (MFSA) (Poliakov and Schieber 1998) was performed by dividing the stimulation period into N non-overlapping fragments, where N is the square root of the number of triggers in the trial. For each fragment, the average post-stimulus EMG response was determined by subtracting the average EMG during a target interval from the average EMG during preceding and following control intervals. The target interval was a 10 ms period centered at 11 ms post-stimulus (Poliakov and Schieber 1998) and control intervals were

10 ms periods centered at 9 ms pre-stimulus and 31 ms post-stimulus, chosen to avoid the stimulus artifact observed immediately following stimulation. The distribution of the average post-stimulus EMG response for each fragment was used to determine a *p*-value for the significance of post-stimulus effects in each muscle using Student's *t*-test with significance level $\alpha = 0.05$. Onset and duration were calculated for significant responses, with onset and offset latencies defined as the times at which the EMG amplitude crossed the 2 SD threshold, shown in Fig. 3*A*.

Force averaging and analysis

Because force measurements could only be collected while the subjects made contact with the joysticks, only data from stimulation sites for which the subject contacted each joystick for cumulatively greater than 100 s (25.0%) of the 400 s stimulation period were included in the StimulusTA force analysis, with 162/311 (52.1%) of stimulation sites meeting these criteria. Subjects were considered to not be making contact with the joysticks if the net force on the joystick was less than 50 mN for greater than 15 ms. Force data were averaged over a 200 ms peri-stimulus window, consisting of a 50 ms pre-trigger and 150 ms post-trigger period. Only triggers during which contact was maintained throughout the entire 200 ms time window were included in the study. Since sites with less than 500 triggers were excluded from the analysis, the number of triggers for which contact was maintained ranged from 500 to 2000 for each stimulation site. To remove slow drift from force recordings, a baseline ramp subtraction procedure was used to level the baseline and set it to zero (Cheney and Fetz 1985).

MFSA was again used to test for post-stimulus force effects (Poliakov and Schieber 1998). For the force response average, the target interval was a 20 ms period centered at 40 ms post-stimulus, and control intervals were 20 ms periods centered at 0 ms and 80 ms post-stimulus. These periods were chosen based on force onset and time-to-peak estimates from trials in which the change in force deviated from baseline by > 4 SD (Soto and Cros 2011). The *N* averages of the difference between target period and control for all 3 components of force were used to determine a *p*-value for the significance of post-stimulus force effects using Hotelling's *T*-squared statistic. The distributions of the direction of force responses for each arm were compared using Pearson's chi-squared test. The statistical significance of bilateral force responses was determined using Fisher's method to combine unilateral significance values. Bilateral force patterns were quantified in Fig. 10 by defining "pure flexion" (directed equally medially and posteriorly) as 1 and "pure extension" (directed equally laterally and anteriorly) as -1 for the ipsilateral side and pure flexion as -1 and pure extension as 1 for the contralateral side and then finding the average of both sides.

Multiple multivariate linear regression

To test for agreement between EMG and force measurements, a multiple multivariate linear regression was performed with the post-stimulus changes in EMG activity of all 12 muscles as explanatory variables and the components of the force responses along all 3 axes as dependent variables. For each muscle, regression coefficients were used to determine if the EMG activity significantly predicted the components (along the x-, y-, or z- axis) of the force response. The change in EMG activity, defined as the average activity during the control intervals subtracted from the average activity during the target interval (Poliakov and Schieber 1998), was calculated for each muscle and used to predict forces recorded from the joystick on the corresponding side only. Because of the bilateral symmetry of the subject's body and posture, the data from both sides were combined into one set. There were no significant differences between the quality or behavior of EMG and force recordings from the left and right arms.

Anatomy and histology

Electrolytic lesions were made with 20 µA stimulation applied for 20 s (DC anodal) in the final tracks at multiple points of interest. After being placed under deep anesthesia with sodium pentobarbital, the subjects were transcardially perfused with phosphate-buffered saline and phosphate-buffered formalin. The brain was then removed and submerged in phosphate-buffered formalin with 30% sucrose for cryoprotection. A freezing microtome was used to cut 50 µm frontal sections and every fourth section was mounted and stained with cresyl violet. The locations of brainstem structures were identified using a stereotaxic atlas (Szabo and Cowan 1984). The locations of EMG recording electrodes were verified by post-mortem dissection. Following histological reconstruction, 12 additional stimulation sites that were outside of the PMRF or within 0.5 mm of midline were excluded from the analysis. As a result, 150 sites met all of the criteria for inclusion in the analysis.

Results

Task-related EMG activity and force outputs

Electromyographic activity was present in all muscles at various times during performance of the task. The EMG activity of every muscle was significantly modulated between the hold phase and the target phase of the task ($p < 0.001$). The average force output during the target phase of the task was approximately 30 N along the y-axis, with smaller magnitude forces (< 10 N) measured along the x- and z-axes during the same time period. A representative example of task-related changes in y-axis force output and BIC and TRIC EMG activity is shown in Fig. 2. No post-stimulus EMG or force effects were evident in the raw data from single pulses before stimulus-triggered averaging was applied.

There was typically a low-to-moderate level of EMG activity during pre-trial hold periods when the subject waited with its hands on the force sensors but before it was instructed to apply force. This resting level of EMG activity was usually sufficient for inter-trial triggers to meet the inclusion criteria for the analysis. The force output was greatest during the target phase of the task. All muscles showed a significant difference in the EMG activity for the pulling vs. pushing aspects of the task. The greatest differences in EMG for pulling vs. pushing were found in the flexors BIC, PMJ, and ADLT and the extensors TRIC and PDLT. The flexors were preferentially facilitated during pulling trials (negative y-direction), whereas the extensors were facilitated during pushing (positive y-direction).

General characteristics of post-stimulus EMG effects

In total, 733 post-stimulus EMG effects (PStEs) were evoked from 139 of the 150 sites included in the analysis, accounting for 92.7% of all PMRF sites tested. On average, 22.0 ± 13.9% of the muscles analyzed responded per effective stimulus site, corresponding to five or six muscles. The overall range of EMG responses was 4.2% (one muscle) to 70.8% (17 muscles) of the 24 muscles tested. A selected example of post-stimulus EMG and force effects is shown in Fig. 3.

Of the 733 PStEs, 423 (57.7%) were post-stimulus suppression (PStS) and 310 (42.3%) were post-stimulus facilitation (PStF). Consistent with its overall prevalence, PStS was evoked from more sites (132/150, 88.0%) than PStF (103/150, 68.7%). Exclusive PStS was observed from 36 sites (24.0%), while exclusive PStF was observed from only 7 sites (4.7%). For each effective stimulus site, 12.7 ± 8.2% of the muscles analyzed were suppressed, and 9.3 ± 10.1% were facilitated. The average onset for PStF of 8.3 ± 2.9 ms was significantly earlier than the average onset for PStS of 9.7 ± 2.9 ms, $t(731) = 6.46$, $p < 0.001$, as shown in Table 2.

Post-stimulus EMG effects by muscle

Fig. 4 shows the effectiveness of stimulation for each muscle, calculated as the number of stimulus-evoked responses in a muscle divided by the number of sites for which EMG was recorded from that muscle. Stimulation was most effective at limb girdle muscles compared to limb flexors and extensors, $\chi^2(1, N = 733) = 29.9$, $p < 0.001$.

EMG effects were most commonly observed in axial muscles like UTR (58.0%) and LAT (51.3%) and least commonly in distal muscles like FCU (27.3%) and ECR (14.0%).

Post-stimulus muscle activation patterns

An average-linkage clustering algorithm was used to classify each of the 12 muscles into two clusters based on their post-stimulus changes in EMG activity from all 150 stimulation sites as calculated by MFSA (Poliakov and Schieber 1998). Muscles that had similar changes in EMG activity across many stimulation sites were clustered nearer each other. The clustering dendrogram is shown in Fig. 5*A*. The clustering assignments segregated muscles into a “flexor-like” muscle group, which contains the primary elbow and shoulder flexors (BIC and ADLT), and an “extensor-like” muscle group, which contains the primary elbow and shoulder extensors (TRIC and PDLT). The wrist muscles, FCU and ECR, were the muscles whose activity was least correlated with either group. While FCU and ECR are most correlated with each other, this may simply be due to the lower effectiveness of stimulation on distal muscles.

Facilitation was the most common post-stimulus effect seen in ipsilateral flexors (BRAC, BIC, ADLT, PMJ) and contralateral extensors (TRIC, PDLT, UTR), while suppression was the most common effect seen in ipsilateral extensors and contralateral flexors, as shown in Fig. 5*B*. LAT exhibited generalized suppression, but more so for the contralateral side of the body, consistent with its classification as a flexor. In general, this agrees with previously published reports (Davidson and Buford 2004), with the new finding that SUP and SUB both group with the extensors.

General characteristics of transient force responses

Significant force responses were detected from 105 (70.0%) of the 150 stimulation sites. Of those sites, 64 sites (61.0%) produced significant force responses bilaterally. Unilateral force responses were detected from the ipsilateral arm for 19 sites (18.1%) and from the contralateral arm for 22 sites (21.0%). In total, 169 significant force responses were detected from either arm. The average magnitude of significant force responses was 12.0 ± 8.5 mN with a maximum of 40.9 mN. For perspective, this mean is about 1.2 grams and the max is about 5.0 grams by weight. The forces required for task performance were approximately 1000 times greater than the observed post-stimulus force responses. The magnitudes were not significantly different between ipsilateral and contralateral responses.

Force onset latencies were determined for post-stimulus effects in which the instantaneous change in force deviated from baseline by > 4 SD. This threshold was reached in 65 (38.5%) of the 169 significant force responses from either arm. For these force responses, the force onset latency was defined as the time at which the change in force crossed the 2 SD threshold relative to the baseline mean. The average onset latency was 15.9 ± 2.6 ms, as shown in Table 2. No significant difference in onset latency was detected between ipsilateral and contralateral force responses. The average time-to-peak, defined as the length of time between stimulus delivery and the maximum force deviation from baseline, was 45.2 ± 18.3 ms (median = 38.8 ms). There was no significant difference in time-to-peak between ipsilateral and contralateral force responses.

Bilateral force output patterns

For the 105 stimulation sites in the PMRF that produced a significant force response in at least one arm, the majority of forces were directed along one of two directions, either medially and posteriorly or laterally and anteriorly. The direction of these force responses was significantly dependent on the laterality of the response relative to the location of the stimulation site (i.e. ipsilateral vs. contralateral), $\chi^2(3, N = 193) = 114.9$, $p < 0.001$. The direction of force responses in the x-y plane can be divided into four groups, determined by the signs of the x- and y- components of force, with each group consisting of one 180° quadrant. 65.3% of significant force responses from the ipsilateral arm were directed medially and posteriorly, $\chi^2(3, N = 95) = 86.5$, $p < 0.001$, shown in Fig. 6; while 78.6% of responses from the contralateral arm were directed laterally and anteriorly, $\chi^2(3, N = 98) = 151.6$, $p < 0.001$, also shown in Fig. 6. For simplicity, results are presented as if the left side were always ipsilateral. Because of the bilateral symmetry of the subject and task design, this was done by mirroring results from right-sided stimulation across midline. In this frame of reference, the average ipsilateral force response was directed at an angle of 317° (medially and posteriorly), and the average contralateral force response was directed at an angle of 47° (laterally and anteriorly). This output pattern is consistent with the facilitation of ipsilateral flexors and contralateral extensors and the reciprocal suppression of contralateral flexors and ipsilateral extensors observed in EMG recordings.

Relationships between force responses and post-stimulus EMG effects

At all 105 sites with a significant force effect in the stimulus-triggered average, there was also at least one muscle with a significant PStE. As noted above, there were 139 sites of the 150 that resulted in a significant PStE, leaving 34 sites from which at least one PStE was evoked, but the force response was not significant. These 34 sites evoked, on average, fewer PStEs than their counterparts, $t(126) = 7.36$, $p < 0.001$.

For those sites from which significant PStEs were found in EMG records and in the forces, the average magnitude of the force responses was significantly correlated with the average post-stimulus change in EMG activity elicited for the same site, $r^2 = 0.425$, $F(1, 148) = 109.4$, $p < 0.001$, as shown in Fig. 7. Similarly, the average force magnitude was significantly correlated with the number of muscles exhibiting a post-stimulus EMG effect, $r^2 = 0.373$, $F(1, 148) = 85.3$, $p < 0.001$. The magnitude of the force and EMG responses was determined by subtracting the average value during the control intervals from the average value during the target interval. For Fig. 7, the average EMG response was calculated by finding the average percent change from baseline during the target interval for all 24 EMG recordings. Similarly, the average force response was found for recordings from both force sensors. As noted above, the magnitude of the stimulus triggered force responses was about $1/1000^{th}$ of the force required to perform the task. Likewise, the sizes of the PStEs ranged from $1/100^{th}$ to $1/1000^{th}$ of the task-related modulation of the EMG levels. The average onset of the PStEs at 8.3 ± 2.9 ms was significantly earlier than the average onset of the force responses at 15.9 ± 2.6 ms, $t(373)$

= 19.5, $p < 0.001$, allowing sufficient time between events for the electromechanical delay.

Multiple multivariate linear regression

To test how well post-stimulus changes in EMG activity account for the observed force responses, a multiple multivariate linear regression model was developed. The explanatory variables were the changes in average EMG activity between control and target intervals for all 12 muscles on one side, measured in multiples of the standard deviation of the EMG levels recorded during the baseline period. The response variables were the components of the force responses along each axis, recorded from the same side as the EMG recordings. For each stimulation site, the force responses were calculated by determining the change in force between the average force onset time and the average time-to-peak. In order to determine the force contributions of all the muscles from which EMG was recorded, a stepwise regression was not used.

The beta coefficients of the regression analysis represent the contributions of each muscle to the generation of force in the ipsilateral arm, as shown in Fig. 8*A*. Facilitation of flexors and suppression of extensors were significantly associated with a resultant medial and posterior deflection in the force response of the corresponding arm, $\chi^2(3, N = 7) = 8.43$, $p = 0.038$; while facilitation of extensors and suppression of flexors were associated with a resultant lateral and anterior deflection, $\chi^2(3, N = 5) = 8.60$, $p = 0.035$. Additionally, the relative change in the EMG activity significantly correlated with the component of the force responses along the x-axis, $r^2 = 0.576$, $F(12, 287) = 32.54$, p <

0.001; y-axis, $r^2 = 0.410$, $F(12, 287) = 16.63$, $p < 0.001$; and z-axis, $r^2 = 0.294$, $F(12, 287) = 9.98$, $p < 0.001$. Every muscle except the FCU made a significant contribution to the regression model, shown in Fig. 8*A*. Variance inflation factors for all muscles were < 5 indicating tolerable multicollinearity of post-stimulus EMG effects. The goodness of fit for the x- and y- components of the linear regression model is shown in Figs. 8*B* and 8*C*, respectively.

Force contributions of antagonistic muscle pairs

According to the regression model, BIC and TRIC made the largest and most significant contributions to the force response ($\beta = 10.7$, $p < 0.001$ and $\beta = 10.0$, $p < 0.001$, respectively). To determine the ability of BIC and TRIC EMG activity alone to explain forces in the x-y plane, a directional tuning curve for the BIC and TRIC was generated, shown in Fig. 9. For each muscle, the correlation coefficients were found between the EMG activity and the projection of the force response vectors in 12 directions at 30° intervals. The correlation coefficient curves were fit well by sinusoidal functions, $r^2 = 0.962$ for both BIC and TRIC. The EMG activity of BIC was best correlated with the components of force directed along an angle of 295° (medially and posteriorly). The TRIC EMG activity was best correlated with the components of force directed along an angle of 118° (laterally and anteriorly). As expected of antagonistic muscles, the BIC and TRIC correlated with components of force in opposite directions (177° difference).

Force patterns by location of stimulation

Stimulus sites were distributed throughout the PMRF with no significant preference for laterality. For bilaterally significant responses, the average force output pattern was significantly different between left- and right-sided stimulation, $t(71) = 16.4$, $p < 0.001$, shown in Fig. 10*B*. The degree of flexion in the response from one arm was significantly correlated with the degree of extension in the other, $r^2 = 0.379$, $F(1, 71) = 43.3$ $p < 0.001$. In Fig. 10*A*, stimulation sites are categorized by their corresponding force output pattern, with different colors representing the directions of the post-stimulus forces effects. Sites that produced a force pattern of left-sided flexion and right-sided extension are shown in red, and sites that produced a pattern of right-sided flexion and left-sided extension are shown in blue. Sites for which no significant bilateral force responses were detected are shown in gray.

Discussion

Detection of transient force responses

Single-pulse microstimulation produces small EMG responses detectable with StimulusTA, but does not produce obvious muscle twitches and is thought to be imperceptible to the subject (Cheney and Fetz 1985). Measuring this post-stimulus EMG activity has been a valuable method for studying motor outputs of cortical and brainstem neurons (Cheney and Fetz 1985; Davidson and Buford 2004, 2006). While individiual movements evoked by a single stimulus may be too small to observe, the present study shows that force responses associated with muscle recruitment can be detected using

StimulusTA. The overall effect of StimulusTA on arm movement is difficult to predict using only the complex pattern of facilitation and suppression of the muscles in that limb. But direct recording of these small force changes can reveal general patterns of arm movement resulting from muscle recruitment. To our knowledge, this is the first demonstration of such a measurement. This approach could also have considerable applications in other brain regions where questions about the coordinate representation encoded remain under study (Kakei et al. 1999, 2001).

While many studies have produced limb and head movements with short stimulus trains in the motor cortex (Lemon 2008) and a few have done so in the brainstem (Drew and Rossignol 1990a, Cowie and Robinson 1994, Riddle et al. 2009, Herbert et al. 2010), this type of stimulation produces spatial and temporal summation leading to activation of polysynaptic pathways. In contrast, the low frequency (5 Hz) and low current intensity (30 μA) of single-pulse microstimulation minimizes temporal and spatial summation and primarily activates monosynaptic and disynaptic pathways, producing a more physiologically relevant response (Cheney and Fetz 1985). StimulusTA with single-pulse microstimulation produces motor outputs similar to those from SpikeTA (Davidson et al. 2007), indicating that results from StimulusTA offer a better approximation of the motor effects of spontaneous neural activity than techniques that use higher frequency stimulation. Hence, it seems likely the force responses measured here are from relatively direct reticulospinal pathways.

Electromechanical delay

Muscle fiber contraction and force generation trails the motor unit action potential onset by a time period known as the electromechanical delay (EMD). Muscle contraction following excitation in the frog sartorius muscle has been shown to occur with a latency as short as 2.5 ms (Sandow 1952). In human finger muscles, forces associated with contraction of single motor units have been measured based on the triggered averaging approach (Kilbreath et al. 2002, Yu et al. 2007). In those studies, forces of 20-50 mN began in single fingers within 2-3 ms of the beginning of the motor unit action potential. In the present study, StimulusTA produced force responses with an average onset time of 15.9 ms post-stimulation, which, considering an average flexor EMG onset latency of around 8.3 ms, corresponds to an EMD of approximately 7.6 ms. An EMD of 8.0 ms has been observed in humans in response to a maximal electrical stimulation of the posterior tibial nerve (Grosset et al. 2008). Winter and Brookes (1991) measured the time interval from the change in electrical activity to the registration of force from a human soleus muscle to be 10.2 ms, and Muro and Nagata (1985) reported similar results of 11.7 ms in unstretched soleus muscle and 7.0 ms in heavily stretched muscle. Hence, the timing of the present results is consistent with the hypothesis that the detected force responses resulted directly from the post-stimulus EMG changes measured by StimulusTA and not through an indirect mechanism. Studies relying on *movement onset* have reported longer estimates of EMD (Norman and Komi 1979, Philipp and Hoffmann 2014, Hoffmann and Strick 1999), but measurements of *force onset* in a pretensed, isometric condition would be expected to reveal relatively short electromechanical delays.

Linear regression analysis

Multivariate linear regression is used to determine the effects of multiple explanatory variables on their associated dependent variables. Linear regression is appropriate for these data because the mean rectified EMG varies approximately linearly with the isometric force generated by a muscle over the mid-range recruitment levels studied (Lippold 1952, Milner-Brown and Stein 1975). Furthermore, because of the stationary position of the subject's arms, activity from a specific muscle will generate forces in a consistent direction. If the force responses are caused by the change in EMG activity following stimulation, a multivariate linear regression model should be able to describe this relationship. Our model uses the change in EMG activity from 12 muscles on one side to predict the direction and magnitude of the force response generated from the corresponding arm.

Linear regression analysis determined the contributions of each muscle to the forces generated at the joysticks, based on muscle EMG activity. The force responses of the studied muscles matched their expected functions, with elbow and shoulder flexors producing forces toward the body and extensors producing forces away from the body. BIC and TRIC made the largest contributions to force generation. Activation of wrist muscles was generally weak and hand position on the joysticks was free to vary with the subject's style across trials, as long as the overall force was properly directed. As a result, the wrist muscles did not strongly contribute to the regression model. The limited contribution of more proximal muscles to the regression model may be dependent on the arm position required by the task and could vary with another recording setup.

Muscle groupings

Davidson and Buford (2006) identified functional groups of upper limb muscles based on reciprocal patterns of EMG activation following PMRF stimulation. Of the muscles analyzed in this study, BIC, BRAC, ADLT, and PMJ have previously been shown to be facilitated during ipsilateral PMRF stimulation and suppressed during contralateral stimulation. Similarly, TRIC, PDLT, and UTR have been shown to be suppressed during ipsilateral PMRF stimulation and facilitated during contralateral stimulation. These groupings were preserved in this study by the clustering algorithm with grouped muscles based only on similarity of post-stimulus EMG activity. The cluster encompassing the BIC, BRAC, ADLT, and PMJ was designated as the “flexor-like” muscle group, while the cluster containing TRIC, PDLT, and UTR was designated as the “extensor-like” muscle group.

Possibly owing to their less consistent responses to stimulation, the distal FCU and ECR were the last muscles to be clustered into either group. Although stimulation has proven less effective at activating more distal muscles, the reticulospinal tract has been shown to make monosynaptic and disynaptic projections to both forearm and intrinsic hand muscles (Riddle et al. 2009). While our results indicate a relatively low level of consistency between the flexor and extensor synergies in the proximal limb muscles and the activation patterns in wrist muscles, hemiparetic stroke patients have been shown to exhibit flexion synergy between proximal arm muscles and those of the wrist and fingers (Miller and Dewald 2012). One possible factor in this discrepancy is that our subjects were free to adopt individual styles and vary their grip on the joysticks across trials, which may have introduced some variability and reduced the consistency of muscle activation patterns. In other words, this might be due to experimental conditions. It is also possible that this is a species difference between humans and macaques.

Rotator cuff muscles, such as SUB and SUP, act as stabilizers of the shoulder joint in addition to other actions on the humeroscapular joint. The primary functions of SUP are external rotation and elevation of the glenohumeral joint. The primary functions of SUB are internal rotation and adduction of the glenohumeral joint. Despite their seemingly opposite functions, both of these muscles strongly clustered with the extensors. This is consistent with their role as stabilizers, both acting during extension particularly to stabilize the glenohumeral joint. However, it is difficult to determine if this pattern of synergy is contingent on the subject being in the position required by the task.

Reciprocal force output pattern

Stimulation of the PMRF has been known to produce bilateral motor output patterns in the cat (Drew and Rossignol 1990a, 1990b; Sprague and Chambers 1954) and monkey (Davidson and Buford 2004, 2006). These movement patterns include flexion of the spine, ipsilateral head turning, ipsilateral arm flexion, and contralateral arm extension. The StimulusTA results agree that PMRF stimulation produces a bilateral pattern of EMG activity. Consistent with previous studies, ipsilateral facilitation and contralateral suppression of flexor-like muscles and reciprocal effects on extensor-like muscles were observed. Generalized suppression of LAT was compatible with flexion of the spine, and ipsilateral suppression and contralateral facilitation of UTR was compatible with ipsilateral head turning. Post-stimulus force responses indicate a strong pattern of flexion of the ipsilateral arm and extension of the contralateral arm, as shown in Fig. 10. This pattern was also detected in force responses corresponding to stimulation sites in which only unilateral EMG activity was identified.

This bilateral action of the PMRF is supported anatomically by evidence of bilaterally distributed monosynaptic and disynaptic pathways. While the majority of reticulospinal axons terminate ipsilaterally, they have also been shown to project bilaterally (Matsuyama et al. 1997). Additionally, ipsilaterally projecting neurons can evoke bilateral motor outputs via commissural interneurons (Bannatyne et al. 2003; Jankowska et al. 2003, 2006). The pattern of flexion of one limb and the extension of the other is closely tied to locomotion (Drew and Rossignol 1984). Supraspinal locomotor command signals to central pattern generators in the spinal cord are primarily conveyed via reticulospinal pathways (Eidelberg et al. 1981; Matsuyama et al. 2004). However, PMRF neurons have also been shown to be modulated during voluntary reaching (Buford and Davidson 2004; Schepens et al. 2004, 2006, 2008). These results suggest that reticulospinal pathways involved in locomotion are also activated during reaching (Drew et al. 2004).

Task-dependent facilitation of post-stimulus effects

It is possible that, because of the the requirements of the task, the behavior of the subjects preferentially facilitated force responses along the y-axis. If the behavioral task required exertion of forces in the x-direction, that may have affected the relative magnitudes of the components of force in the x- and y-directions. However, because the flexion/extension pattern of the force responses was produced with bilaterally symmetric task requirements, we would expect the force responses to display the observed reciprocal force output pattern regardless of the exact nature of the task. While it would be interesting to subdivide the averages into periods of different patterns of exertion to construct an average from data collected only while both arms were pushing, another with one arm pulling and the other pushing, etc., the design of the study did not permit that. We would have needed to apply at least four times as many stimuli to support that analysis, perhaps more, and this would have made data collection four times as slow. As a practical matter in the design of this study, there was simply not enough time to perform so much stimulation. Perhaps a future study could be designed to allow dividing the stimuli for averaging in this manner.

Conclusions

This novel technique for measuring force responses from StimulusTA provides strong confirmation of a bilateral double reciprocal pattern of PMRF output. The high internal consistency of our results, especially the EMD determined by the force onset latency and the strong correlation between EMG activity and force direction and magnitude, supports the validity of these findings. To our knowledge, this is the first report of low-intensity, single-pulse microstimulation in the CNS producing measureable force outputs. Our study provides a new approach to measuring very small forces on the order of a few grams by weight generated by single-pulse microstimulation in the CNS.

Potentially, this approach could also reveal force responses associated with spontaneous neural activity in the motor system. This technique could be applied to other brain regions, such as the motor cortex, to detect physiological motor outputs.

No.	*Muscle*	*Function(s)*	*Abbr.*
1	Flexor carpi ulnaris	Wrist flexion	FCU
2	Extensor carpi radialis	Wrist extension	ECR
3	Brachioradialis	Elbow flexion	BRAC
4	Biceps brachii	Elbow flexion	BIC
5	Triceps brachii, lateral	Elbow extension	TRIC
6	Anterior deltoid	Humerus flex. & in. rot.	ADLT
7	Posterior deltoid	Humerus ext. & ex. rot.	PDLT
8	Subscapularis	Humerus adduct. & in. rot.	SUB
9	Supraspinatus	Humerus abduct. & ex. rot.	SUP
10	Pectoralis major	Humerus flex. & adduct.	PMJ
11	Latissimus dorsi	Humerus ext. & adduct.	LAT
12	Upper trapezius	Scapula elevation	UTR

Table 3.1 List of EMG implantation sites. EMG Implants were located in left and right muscles, with 12 muscles per side, for a total of 24 muscles. Abbr. functions: *flex.* flexion, *ext.* extension, *adduct.* adduction, *abduct.* abduction, *rot.* rotation – *in.* internal and *ex.* external.

	Timing (ms)					
	EMG PStF		*EMG PStS*		*Force*	
	Onset	*Duration*	*Onset*	*Duration*	*Onset*	*TTP*
Mean	8.3	7.3	9.7	6.6	15.9	45.2
SD	2.9	5.0	2.9	3.7	2.6	18.3

	Amplitude		
	EMG PStF (%)	*EMG PStS (%)*	*Force (mN)*
Mean	11.0	9.2	12.0
SD	4.0	3.4	8.5

Table 3.2 Characteristics of post-stimulus effects. Timing and amplitude characteristics of post-stimulus force responses and EMG facilitation and suppression. Onset latency is defined as the earliest time at which the EMG or force recording deviated from baseline activity by > 2 SD. *TTP*, Time-to-peak.

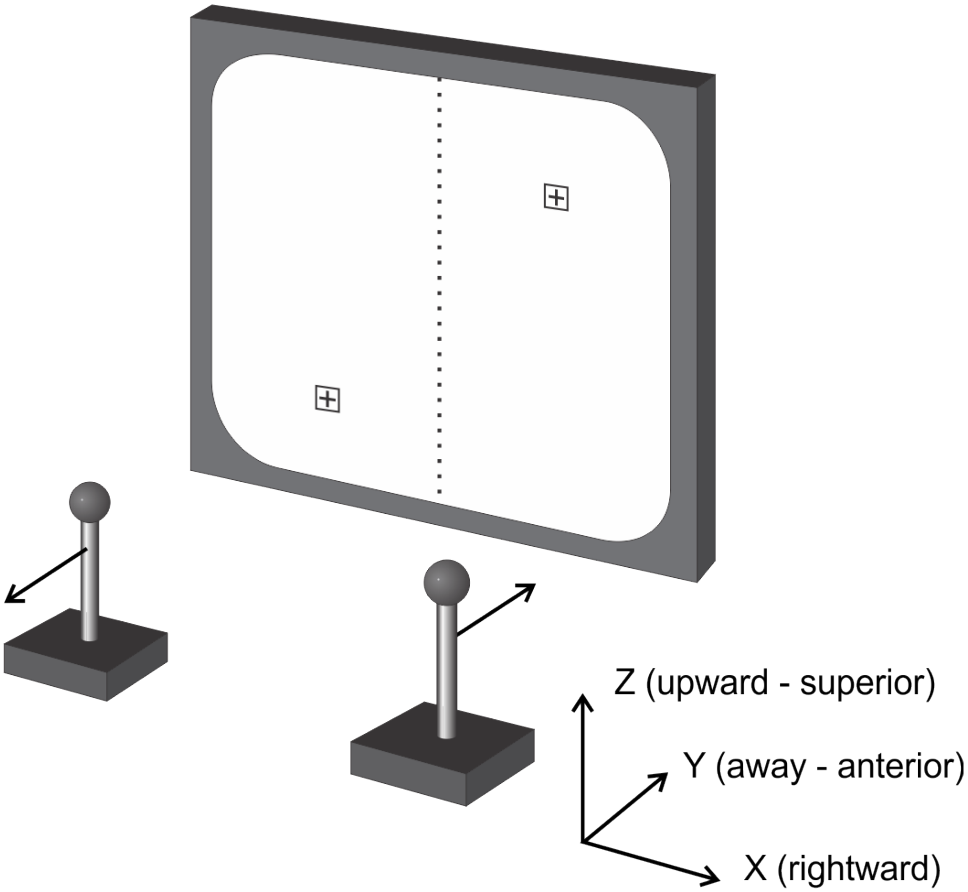

Figure 3.1 Schematic of the apparatus for the isometric force control task. The force-sensitive joysticks control the cursors on the display screen. The target locations correspond to the positions for a task requiring left-sided pulling and right-sided pushing. The coordinate system demonstrates the orientations of the x- (mediolateral), y- (anteroposterior), and z- (superoinferior) axes.

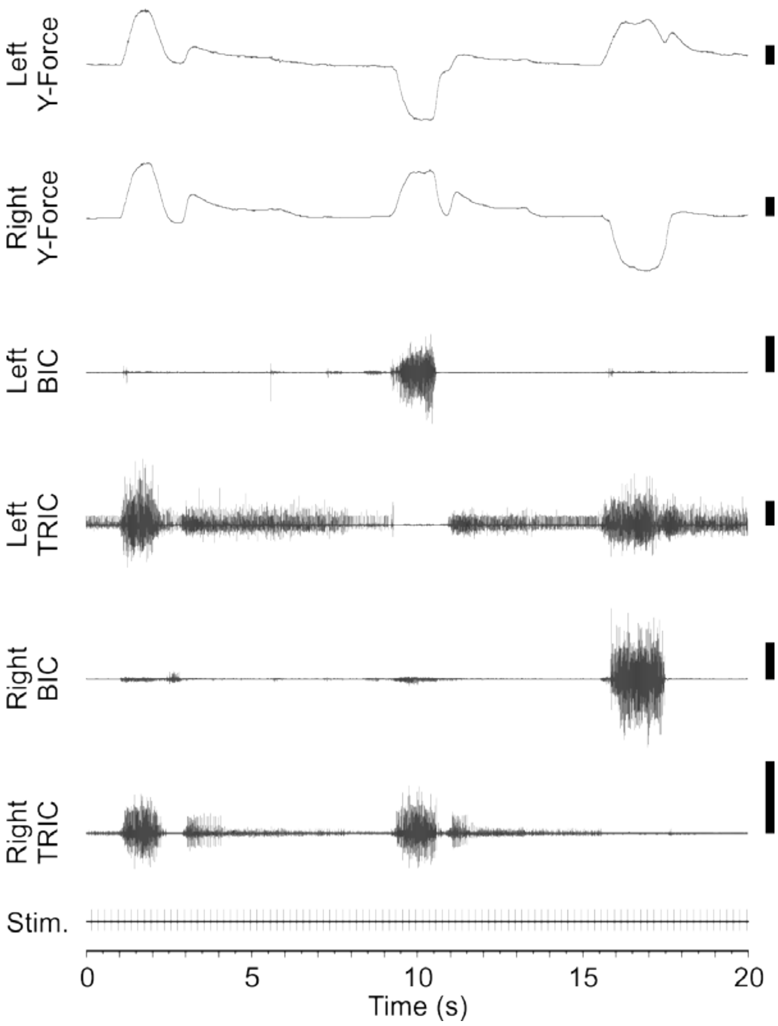

Figure 3.2 Representative example of task-related changes in y-axis force and BIC and TRIC EMG activity. Three trials are shown over a 20 s period. The first trial required bilateral pushing, the second left-sided pulling and right sided pushing, and the last left-sided pushing and right-sided pulling. EMG recordings show increased BIC activity during trials requiring pulling for that arm and increased TRIC activity during trials requiring pushing. Scale bars represent 10 N for force recordings and 1 mV for EMG recordings. Throughout the session, 30 µA stimulation was applied at 200 ms intervals (5 Hz).

Figure 3.3 Selected example of EMG and force recordings of ipsilateral flexion and contralateral extension in response to left-sided PMRF stimulation. *A*: Significant post-stimulus EMG effects. Significant periods of PStF are indicated by *filled bars*, PStS by *open bars*. Scale bars on right represent 0.01 mV except those for ECR and right TRIC which represent 0.001 mV. *B*: Corresponding post-stimulus force responses showing posteromedial forces toward the body from the left (ipsilateral) arm and anterolateral forces away from the body from the right (contralateral) arm. Scale bars represent 10 mN. For this site, all averages included at least 1355 triggers. The 30 µA stimulation was applied at time 0 s.

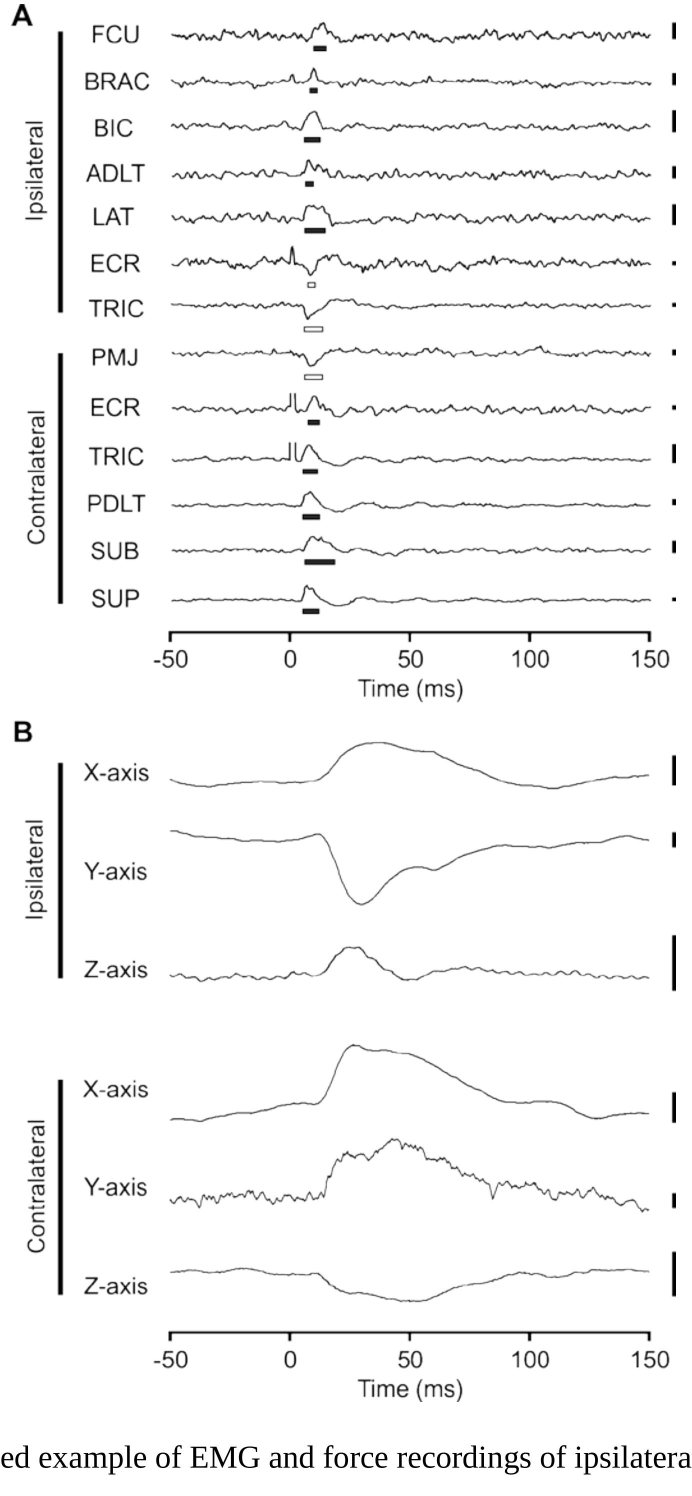

Figure 3.3 Selected example of EMG and force recordings of ipsilateral flexion and contralateral extension in response to left-sided PMRF stimulation.

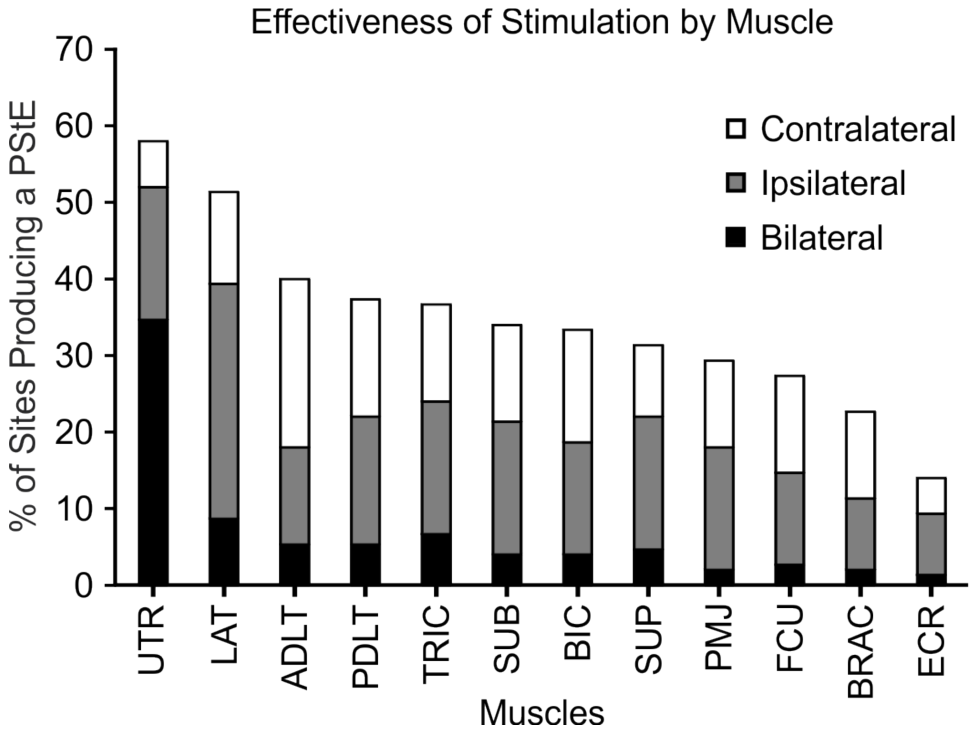

Figure 3.4 Effectiveness of stimulation at producing post-stimulus EMG effects, determined for each muscle by calculating the percentage of sites from which a PStE was observed for each muscle. Percentages are subdivided based on the laterality of the responses evoked from each muscle. The height of the black bar represents the proportion of PStEs that produced a bilateral response, the gray bar represents ipsilateral responses, and the white bar represents contralateral responses.

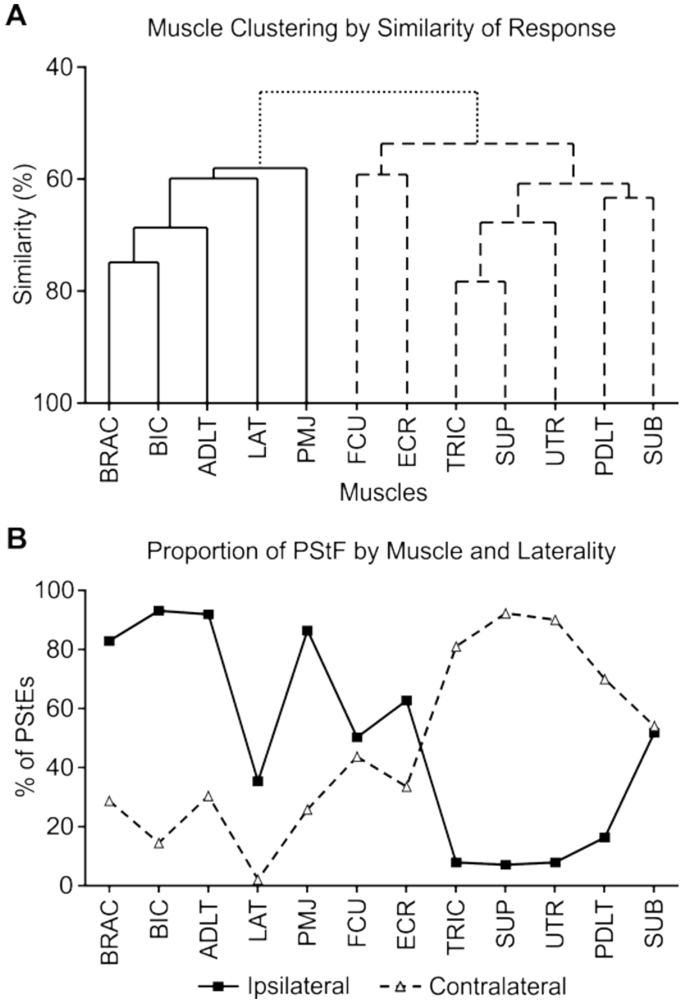

Figure 3.5 Muscle activation patterns and distribution of PStF and PStS by muscle. *A*: Dendrogram showing muscle activation groupings based on average-linkage clustering algorithm of relative change in EMG activity following stimulation. The *solid line* indicates the flexor-like cluster; the *dashed line* indicates the extensor-like cluster. Similarity in activity between muscles is denoted by the vertical location of the branch point. *B*: Each point represents the percentage of PStEs that were PStF for that muscle, organized along the horizontal axis to match clustering results. The *solid line* represents ipsilateral muscles; the *dashed line* represents contralateral muscles.

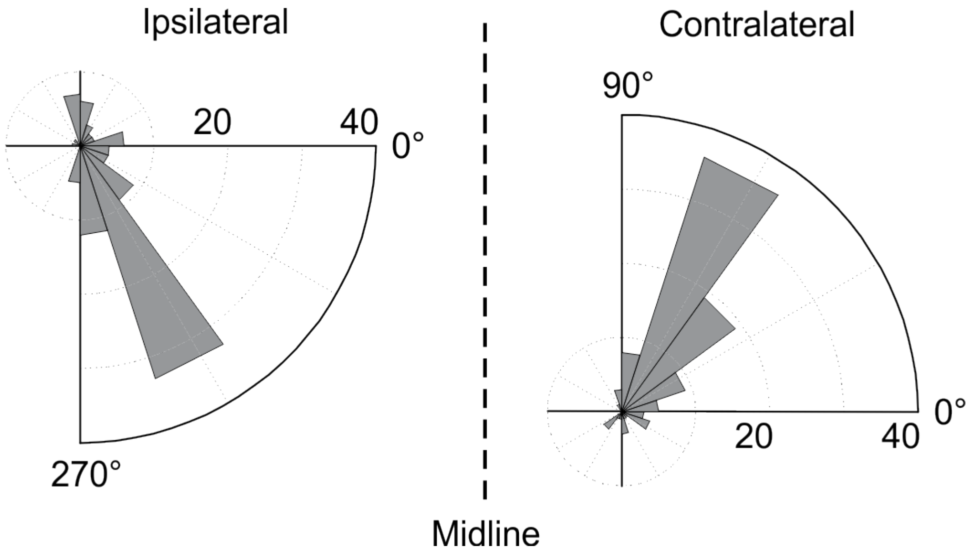

Figure 3.6 Polar histograms of the direction of post-stimulus force responses in the horizontal (x-y) plane. *Left*: Distribution of force responses from side ipsilateral to the stimulus site, with 0° medial and 270° posterior, shown as if the ipsilateral side were always on the left. Ipsilateral force responses were primarily directed medially and posteriorly, $p < 0.001$. *Right*: Distribution of force responses contralateral to stimulus site, with 0° lateral and 90° anterior, shown as if the contralateral side were always on the right. Contralateral force responses were primarily directed laterally and anteriorly, $p < 0.001$.

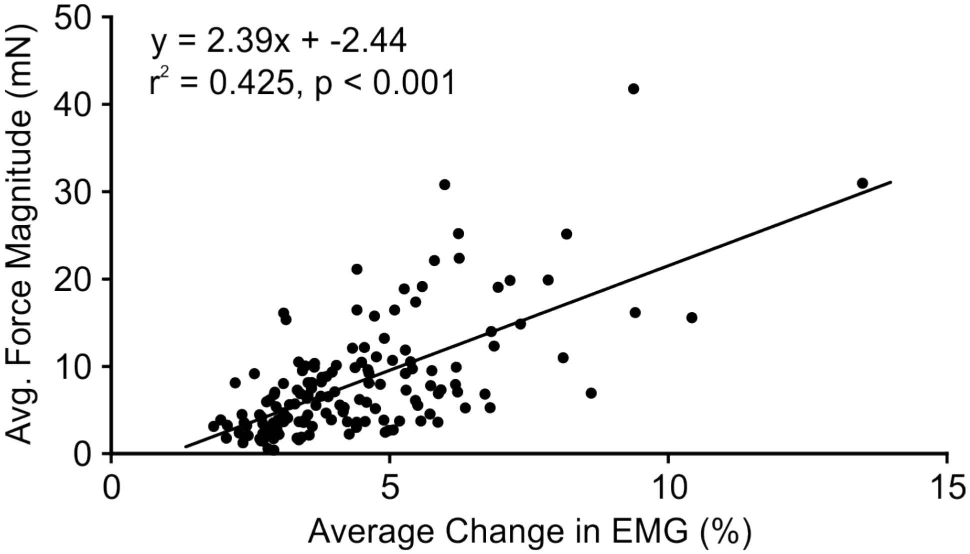

Figure 3.7 Correlation between the magnitude of post-stimulus EMG effects with the magnitude of post-stimulus force responses. A significant correlation was observed between the average change in EMG activity during the target interval as a percentage of the baseline activity and the average force magnitude, $r^2 = 0.425$, $p < 0.001$, $n = 150$.

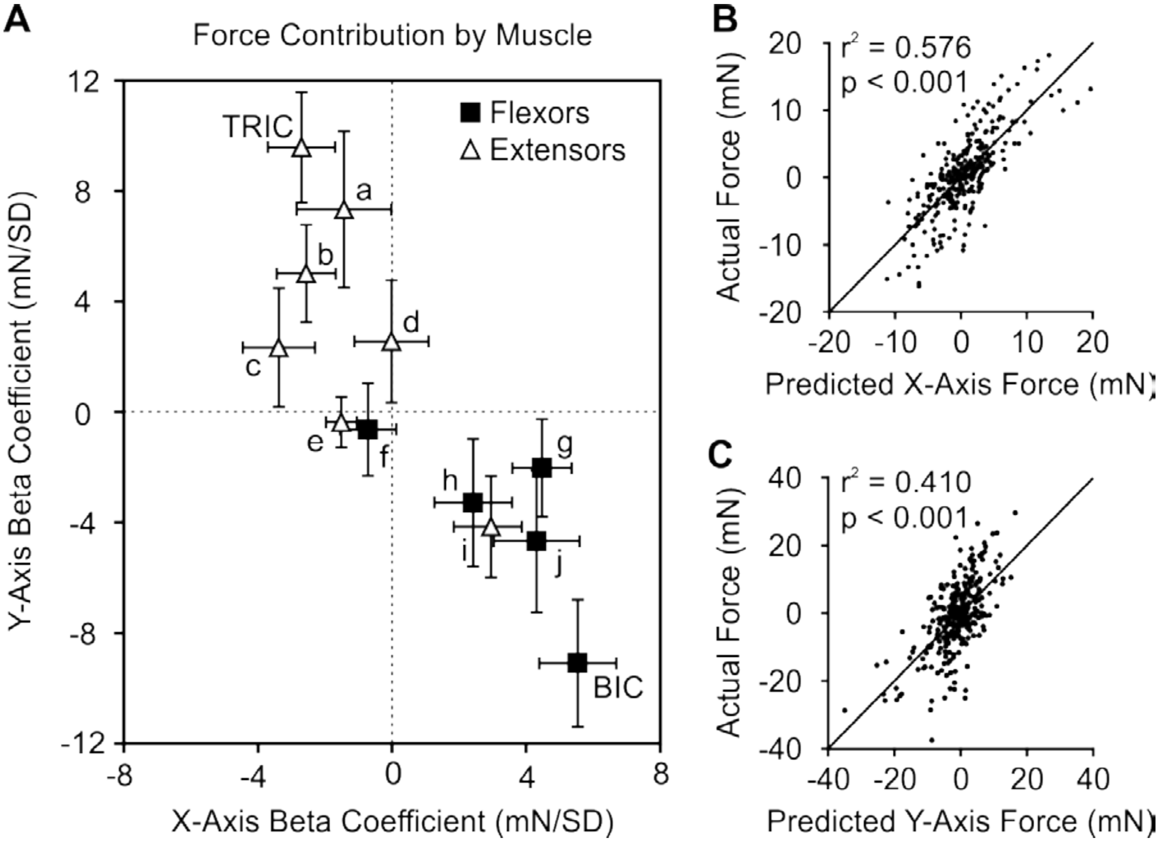

Figure 3.8 *A*: Contributions of each muscle to force responses as determined by the linear regression model. *Filled* s*quares* represent flexor-like muscles and *open triangles* represent extensor-like muscles. BIC and TRIC are directly labeled and superscripts specify the other muscles: *a*, ECR; *b*, PDLT; *c*, SUP; *d*, FCU; *e*, UTR; *f*, LAT; *g*, ADLT; *h*, PMJ; *i*, SUB; *j*, BRAC. The positive x-axis is medial, and the positive y-axis is anterior. Error bars correspond to the standard error. *B*: Linear regression model predictions compared with actual x-axis (mediolateral) components of force responses and best-fit line, $r^2 = 0.576$, $p < 0.001$, n = 300. *C*: Linear regression model predictions compared with actual y-axis (anteroposterior) components of force responses and best-fit line, $r^2 = 0.410$, $p < 0.001$, n = 300.

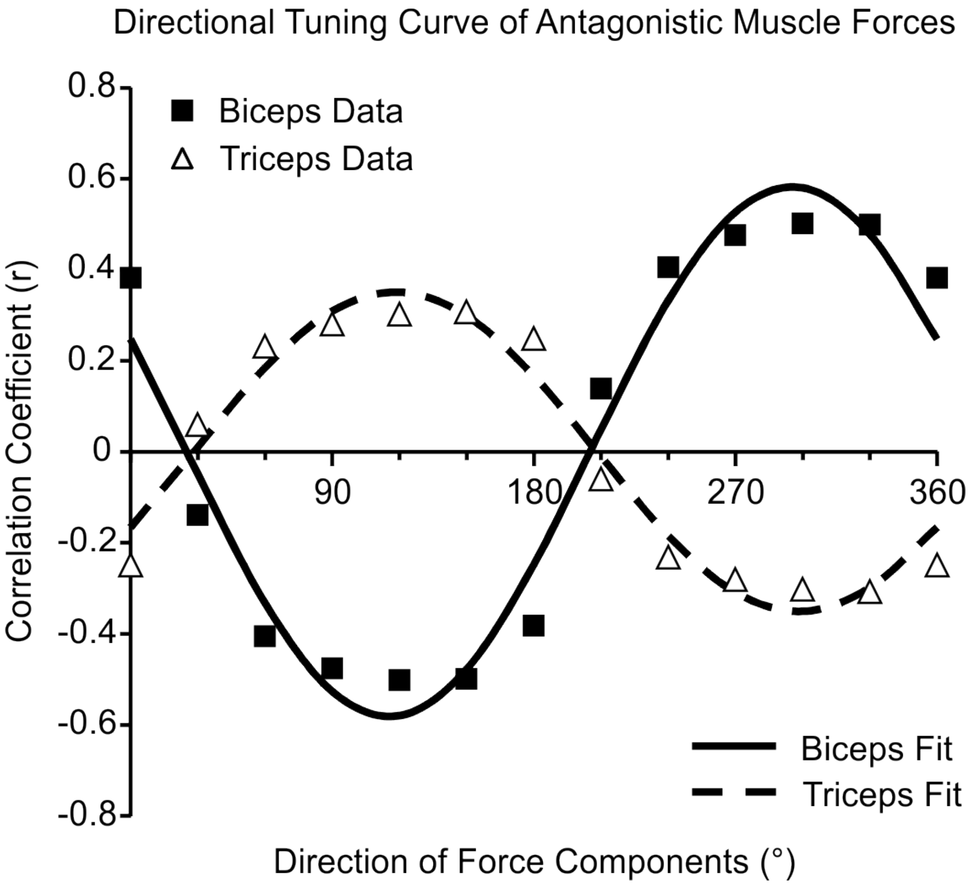

Figure 3.9 Directional tuning curve showing the correlation of EMG activity with the components of force responses in each direction. For BIC and TRIC, the correlation coefficients were found between the EMG activity and the components of force in 12 directions at 30° intervals. Standard cosine functions were used to fit data for BIC (*solid line*, *filled circles*) and TRIC (*dashed line*, *open triangles*). BIC activity was best correlated with the force components for 295°, and TRIC activity was best correlated with the force components for 118°. For both BIC and TRIC, r^2 = 0.962.

Figure 3.10 *A*: Anatomical locations of stimulation sites with associated force response patterns. Brainstem sections adapted from Szabo and Cowan (1984) with nomenclature from Martin and Bowden (1996). *Colored circles* represent a significant force response, with *red* representing a pattern of left-sided flexion and right-sided extension (LFRE), *blue* representing left-sided extension and right-sided flexion (LERF), and intermediate values defined by the color scale at the bottom. *Gray circles* indicate nonsignificant bilateral force responses. *n4* fourth cranial nerve; *n5* fifth cranial nerve; *6* sixth cranial nerve nucleus; *n7* seventh cranial nerve; *7* seventh cranial nerve nucleus; *n8* eighth cranial nerve; *10* tenth cranial nerve nucleus; *12* 12th cranial nerve nucleus; *icp* inferior cerebellar peduncle; *mcp* middle cerebellar peduncle; *scp* superior cerebellar peduncle; *Py* pyramidal tract; *tz* trapezoid body; *IO* inferior olivary nucleus; *SO* superior olivary nucleus; *IVe* inferior vestibular nucleus; *SVe* superior vestibular nucleus; *LVe* lateral vestibular nucleus; *MVe* medial vestibular nucleus; *PrP* nucleus prepositus; *ACu* anterior cuneate nucleus; *Sol* nucleus solitarius; *Pr5* principal nucleus of fifth cranial nerve; *Sp5* spinal nucleus of fifth cranial nerve; *LC* locus coeruleus; *IC* inferior colliculus; *SC* superior colliculus; *4V* fourth ventricle; *Aq* cerebral aqueduct. The circle with crosshairs represents dorsoventral -12, mediolateral 0 in the stereotaxic coordinates. *B*: Bilateral force output patterns by laterality of stimulation site (left vs. right). Output patterns corresponding to LFRE are closer to 1, and those corresponding to RFLE are closer to -1. *** $p < 0.001$. Error bars, S.E.M.

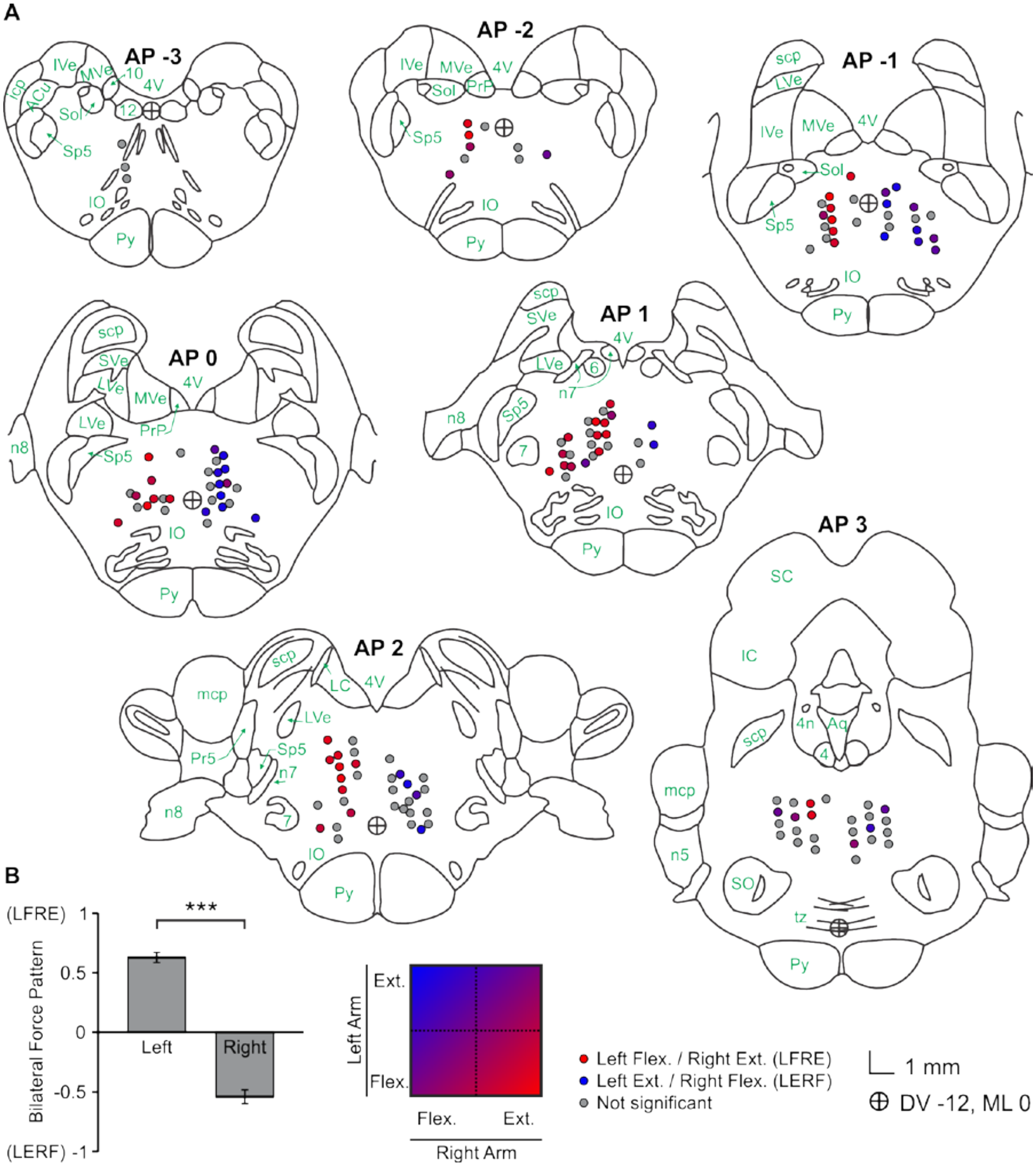

Figure 3.10 Anatomical locations of stimulation sites with associated force response patterns.

Chapter 4: Comparison of stimulus-triggered averaging results to spike-triggered averaging of motor outputs from nearby reticulospinal neurons

Introduction

Spike-triggered averaging (SpikeTA) is the most direct electrophysiological method of investigating physiological motor outputs of neurons. SpikeTA is performed by averaging the EMG activity before and after action potentials recorded from an individual neuron. The major motor effects revealed by SpikeTA of CNS neurons are thought to be primarily mediated through monosynaptic and disynaptic connections to motor neurons (Cheney and Fetz 1985; Baker and Lemon 1998; Davidson et al. 2007). Because StimulusTA is also thought to activate monosynaptic and disynaptic pathways (Cheney and Fetz 1985), it might be expected that StimulusTA and SpikeTA would produce similar effects when performed at the same site. Previous SpikeTA studies of spontaneous neural activity in the motor cortex and PMRF revealed similarity between post-spike EMG effects and post-stimulus EMG effects evoked by single-pulse microstimulation (Cheney and Fetz 1985; Davidson et al. 2007). In the PMRF study, less than 5% (14/309) of recorded neurons produced SpikeTA effects, suggesting that most reticulospinal neurons affect cervical motor neurons indirectly through interneurons (Davidson et al. 2007). Force transients in the upper limbs evoked by microstimulation of PMRF neurons have been identified with StimulusTA in the primate (Hirschauer and

Buford 2015), but no SpikeTA-based studies have detected force outputs of spontaneous PMRF spiking.

The purpose of the present study was to determine the motor outputs that result from spontaneous spiking of PMRF neurons using the SpikeTA approach to measure post-spike EMG *and* force effects. Despite the small magnitude of previously detected post-spike EMG effects, we expected measureable forces to be exerted by the upper limbs following spontaneous PMRF spiking. Furthermore, we expected the pattern of forces to correspond to the reciprocal pattern of EMG activity associated with PMRF output observed in previous StimulusTA and SpikeTA studies (Hirschauer and Buford 2015). Similarity between StimulusTA and SpikeTA force effects would confirm the validity of StimulusTA as an accurate method to determine the force outputs from CNS neurons. Additionally, demonstrating the effectiveness of this technique would permit direct measurement of force outputs evoked by spontaneous spiking of CNS neurons.

Methods

Subjects, task, and surgery

The experimental setup and surgical procedures have been previously described (Hirschauer and Buford 2015). Briefly, one male monkey (*Macaca fascicularis*) was trained to perform a bilateral isometric force control task, in which the subject controlled two cursors on a computer screen via two stationary force-sensitive joysticks located in front of it at waist level. The subject tended to grip the joysticks with its palms down and its forearms pronated. Cursors were primarily controlled by pushing and pulling along the anteroposterior y-axis, with each cursor controlled by one joystick. Each trial consisted of a hold period with targets located midway between the top and bottom of the screen (1.0 s duration). The subject had to grip the joystick but neither push nor pull. An exertion period then occurred with targets moving either up or down on the screen. The subject had to push to move the cursor up, or pull to move it down to capture the target. The cursors both had to be held on target for 0.5 second to complete a trial. The task was set so that pushing or pulling forces of approximately 30 N were required to move the cursors to the targets. Two targets appeared for each trial type (one for each arm), in one of 4 possible combinations (push:push, push:pull, pull:push, pull:pull), which were presented in a pseudorandomized order.

Surgical procedures for implanting the recording chamber and EMG electrodes were similar to those provided in previous reports (Davidson and Buford 2004, 2006; Hirschauer and Buford 2015). A stainless steel recording chamber was mounted to the skull over a craniotomy of the left parietal bone and secured. The center of the recording chamber was directed toward Horsley-Clark stereotaxic coordinates anteroposterior (AP) 0, mediolateral (ML) 0, dorsoventral (DV) -12, allowing bilateral access to the PMRF (Szabo and Cowan 1984). The chamber was tilted approximately 10° laterally to avoid penetration of midline vascular structures. Subcutaneous EMG electrodes were implanted intramuscularly in 12 pairs of arm and shoulder muscles bilaterally (Park et al. 2000). The muscles implanted were the anterior deltoid (ADLT), biceps brachii (BIC), brachioradialis (BRAC), extensor carpi radialis (ECR), flexor carpi ulnaris (FCU), latissimus dorsi (LAT), posterior deltoid (PDLT), pectoralis major (PMJ), subscapularis

(SUB), supraspinatus (SUP), triceps brachii (TRIC), and upper trapezius (UTR), on both sides. Subject care complied with the NIH Guide for the Care and Use of Laboratory Animals and the institutionally approved animal care protocol for our laboratory.

Neural activity recording and neuron isolation

Extracellular neural recordings were obtained by inserting tungsten microelectrodes through guide tubes placed in a two-dimensional grid over an open craniotomy. For each recording, the guide tube was advanced into the cerebellum and the electrode was lowered through the guide tube and into the brainstem. Recordings were made from 174 different sites throughout the PMRF from 35 electrode penetrations. Extracellular field potentials were recorded from neurons as the electrode was inserted through the brainstem until neural activity was no longer detected. Following recordings, 30 µA single-pulse microstimulation was applied at 0.5 mm intervals as the electrode was retracted to regions in which task-related neural activity had been detected (Hirschauer and Buford 2015).

Neuron isolation was performed by identifying putative action potentials in raw neuronal recordings using CED Spike2 software. Next, principal component analysis was applied to the action potential features and distinct clusters were identified as separate neurons. Differences in action potential magnitude, shape, and duration allowed for differentiation between nearby neurons. Final spike assignments were restricted so that individual neurons did not have firing rates over 100 Hz, eliminating most instances where potentials from two neurons were detected as one.

EMG and force recordings, averaging, and analysis

As previously described (Hirschauer and Buford 2015), EMG activity was recorded from 12 pairs of chronically-implanted intramuscular electrodes. Bilateral forces were recorded using two stationary, force-sensitive joysticks, which the subject was trained to grasp. To maintain an isometric condition, the joysticks measured the magnitude and direction of forces applied by the subject, but did not move. Each load cell output controlled the movement of its respective cursor on the display screen. Force measurements were recorded along the x-, y-, and z-axes from each joystick. Force vectors were calculated using simple vector addition of the axial components. Procedures for compiling StimulusTAs of EMG data have been previously described in detail (Davidson and Buford 2006; Herbert et al. 2010, Hirschauer and Buford 2015). Briefly, for each muscle, EMG records were adjusted to remove DC offsets, rectified, and averaged off-line using custom scripts for Spike2 and MATLAB. Averages were compiled over an 80 ms window with a 20 ms pre-spike period and a 60 ms post-spike period. A minimum of 4000 triggers were required for a SpikeTA to be included in the analysis, with a typical analysis including more than 12000 triggers.

To test for post-stimulus EMG effects, multiple fragment statistical analysis (MFSA) (Poliakov and Schieber 1998) was performed by dividing the stimulation period into *N* non-overlapping fragments, where *N* is the square root of the number of triggers in the trial. For each fragment, the average post-spike EMG effect was determined by subtracting the average EMG during a target interval (6-16 ms post-spike) from the average EMG during preceding and following control intervals (14-4 ms pre-spike and

26-36 ms post-spike) (Poliakov and Schieber 1998), chosen to match StimulusTA intervals. The distribution of the average post-spike EMG activity for each fragment was used to determine a *p*-value for the significance of post-spike effects in each muscle using Student's *t*-test with significance level $\alpha = 0.05$. The overall statistical significance of EMG effects for each neuron was determined using Fisher's method to combine significance values from individual muscles.

Because force measurements could only be collected while the subject made contact with the joysticks, only data recorded from neurons for which the subject contacted each joystick for cumulatively greater than 100 seconds during neural recording were included in the SpikeTA force analysis. The subject was considered to not be making contact with the joysticks if the net force on the joystick was less than 50 mN for greater than 15 ms. Force data were averaged over a 200 ms peri-spike window, consisting of a 50 ms pre-spike and 150 ms post-spike period. Only triggers during which contact was maintained throughout the entire 200 ms time window were included in the study. A 50 Hz moving average-based high-pass filter was applied to isolate fast changes in force caused by neuronal spiking from slower changes in force associated with task-related movement.

MFSA was again used to test for post-spike force effects (Poliakov and Schieber 1998). The post-spike force effect was defined as the change in force between the average force onset time (16 ms) and the mean time-to-peak (31 ms) as determined by the high-pass filtered StimulusTA force traces (Hirschauer and Buford 2015). The *N* averages of the force change for all 3 components of force were used to determine a *p*-

value for the significance of post-spike force effects using Hotelling's *T*-squared statistic. The statistical significance of bilateral force responses was determined using Fisher's method to combine unilateral significance values.

Results

General characteristics of post-spike EMG effects

In total, post-spike EMG effects (PStEs) were detected from 34 of the 269 neurons (10.4%) isolated from 174 recording sites included in the analysis. On average, 15.7 ± 7.8% of the muscles responded per recording site with a significant effect, corresponding to 3 or 4 muscles. The overall range of EMG responses was 4.2% (1 muscle) to 33.3% (8 muscles) of the 24 muscles tested. A selected example of post-spike EMG effects is shown in Figs. 4.1 and 4.2. Of the 128 PStEs, 71 (55.5%) were post-spike suppression (PStS) and 57 (45.5%) were post-spike facilitation (PStF). Post-spike EMG effects were more often observed in proximal muscles (ADLT = 22.1%, UTR = 20.6%) than distal muscles (ECR = 10.3%, FCU = 11.8%). The majority of flexor muscles exhibited higher percentages of facilitation ipsilaterally and suppression contralaterally (ipsilateral PStF %: ADLT, 83%; BIC, 60%; BRAC, 80%; FCU, 75%; and LAT, 40%); whereas the majority of extensor muscles exhibited higher percentages of facilitation contralaterally and suppression ipsilaterally (contralateral PStF %: SUB, 80%; SUP, 29%; TRIC, 72%; and UTR, 60%). These results are consistent with previous reports from our lab for StimulusTA and SpikeTA data, demonstrating that the SpikeTA effects obtained here were typical.

General characteristics of post-spike force effects

Significant post-spike force responses were detected for 12 of the 34 recording sites (35.3%) from which significant EMG effects were found. The average onset latency for post-spike force responses was 17.6 ± 2.0 ms. An example of post-spike force responses is shown in Fig. 4.3, corresponding to the same recording site as the EMG effects shown in Figs. 4.1 and 4.2. The average post-spike change in EMG activity was significantly correlated with the average post-spike force effect magnitude, $p < 0.001$ (Fig. 4.4).

Comparison of StimulusTA and SpikeTA effects

The comparison of post-stimulus and post-spike EMG effects for one of the neurons, shown in Fig. 4.5, exhibits a significantly positive correlation, $p < 0.001$, $r^2 = 0.484$, indicating that for muscles with a large StimulusTA effect, there tended to be a large SpikeTA effect. Of the 34 neurons exhibiting significant post-spike EMG effects, 5 neurons (15%) showed a significant correlation with the post-stimulus EMG effects from the nearest StimulusTA site. For all 5 of these neurons that displayed a significant correlation with their nearest stimulation site, the correlation was *positive*, $p = 0.031$.

Discussion

Detection of post-spike force responses

Spontaneous neural spiking produces small EMG effects revealed by SpikeTA. Measuring this post-spike EMG activity has been a valuable method for studying motor outputs of cortical and brainstem neurons (Cheney and Fetz 1985; Davidson and Buford 2004, 2006). Although individual muscle twitches generated by a single spike may be too small to observe, the present study shows that force responses associated with muscle recruitment can be detected using SpikeTA. It is difficult to predict the overall effect of PMRF neuron spiking on arm movement with only PSpEs because muscle responses are typically widespread, bilateral, and complex. However, the present results show that direct recording of these small force changes can reveal general patterns of arm movement resulting from muscle recruitment. To our knowledge, this is the first demonstration of such a measurement.

Electromechanical delay

In a previous study, StimulusTA produced force responses with an average onset time of 15.9 ms post-stimulation which corresponds to an EMD of approximately 7.6 ms (Hirschauer and Buford 2015). In this study, the average force onset latency was 17.6 ms post-spike, which corresponds to an EMD of approximately 8.0 ms. The timing of the force onset supports the hypothesis that the observed force effects resulted directly from the post-spike changes in EMG and not through a more indirect pathway.

Similarity of SpikeTA and StimulusTA EMG and force responses

The significant correlation between post-spike and post-stimulus EMG effects at nearby sites, shown in Fig. 4.5, demonstrates that single-pulse microstimulation is capable of reproducing the motor outputs of spontaneous neural spiking. Agreement between SpikeTA and StimulusTA methods confirm the double reciprocal pattern of motor output from PMRF neurons – facilitation of ipsilateral flexors and contralateral extensors and suppression of contralateral flexors and ipsilateral extensors. In addition to correlations in EMG effects, SpikeTA and StimulusTA exhibited similarities for post-spike and post-stimulus *force effects*, shown in Fig. 4.3. However, because stimulation does not necessarily activate the same neuron from which spiking was recorded, there were many cases in which SpikeTA and StimulusTA results were uncorrelated.

Reciprocal force output pattern

Stimulation of the PMRF has been known to produce bilateral motor output patterns in the cat (Drew and Rossignol 1990a, 1990b; Sprague and Chambers 1954) and monkey (Davidson and Buford 2004, 2006; Hirschauer and Buford 2015). These movement patterns include flexion of the spine, ipsilateral head turning, ipsilateral arm flexion, and contralateral arm extension. The present SpikeTA results demonstrate that spontaneous spiking of PMRF neurons produces a bilateral pattern of EMG activity. Consistent with previous studies, ipsilateral facilitation and contralateral suppression of flexor-like muscles and reciprocal effects on extensor-like muscles were observed. Post-spike force responses also display a pattern of flexion of the ipsilateral arm and extension of the contralateral arm, shown in Fig. 4.3, similar to post-stimulus force patterns. This bilateral action of the PMRF is supported anatomically by evidence of bilaterally distributed monosynaptic and disynaptic pathways. While the majority of reticulospinal axons terminate ipsilaterally, they have also been shown to project bilaterally

(Matsuyama et al. 1997). Additionally, ipsilaterally projecting neurons can evoke bilateral motor outputs via commissural interneurons (Bannatyne et al. 2003; Jankowska et al. 2003, 2006).

Conclusions

The present results demonstrate that single PMRF neurons can produce muscle recruitment in a bilateral reciprocal pattern sufficient to produce very small force transients consistent with ipsilateral upper limb flexion and contralateral upper limb extension. This novel measurement of force responses assciated with single unit neural activity in the brainstem opens a new window to the study of motor functions of the central nervous system.

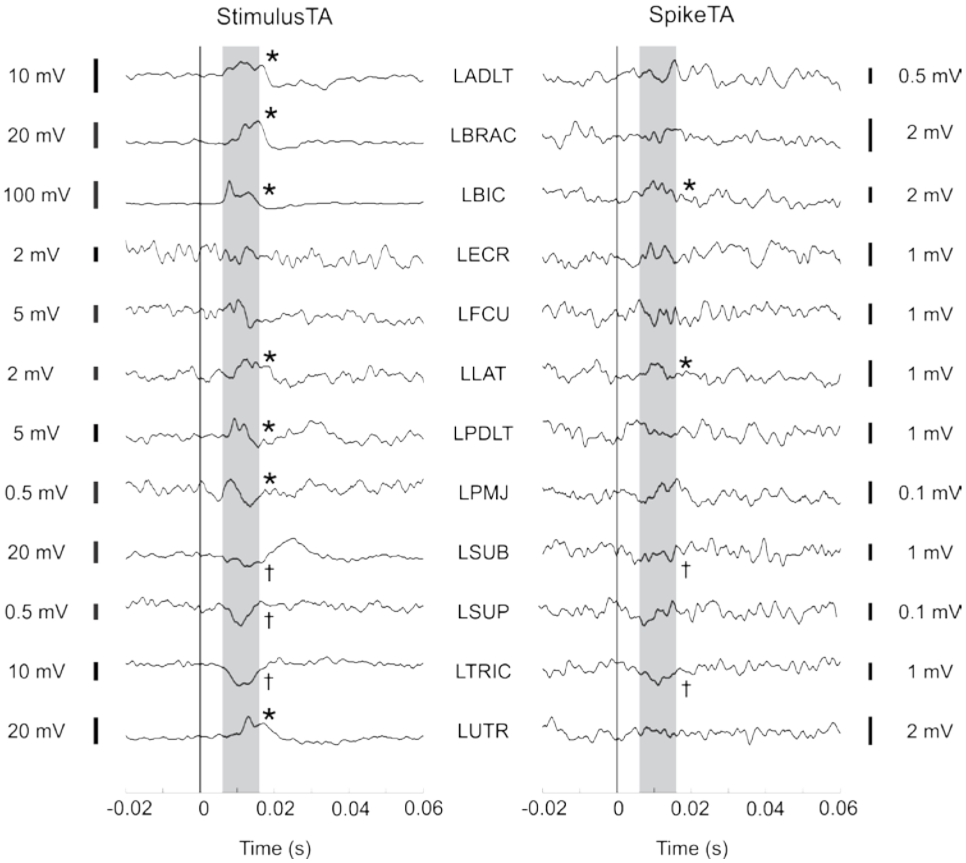

Figure 4.1 Selected example of EMG recordings of ipsilateral flexor facilitation and extensor suppression in response to left-sided PMRF stimulation (StimulusTA, left) or spontaneous spiking (SpikeTA, right). Significant post-stimulus EMG effects are indicated by *asterisks* for PStF and *daggers* for PStS. Scale bars represent indicated voltage changes. For StimulusTA, all averages included at least 1355 triggers; for SpikeTA, all averages included at least 15000 triggers. For StimulusTA, 30 µA stimulation was applied at time 0 s; for SpikeTA, a neuronal spike was detected at time 0 s.

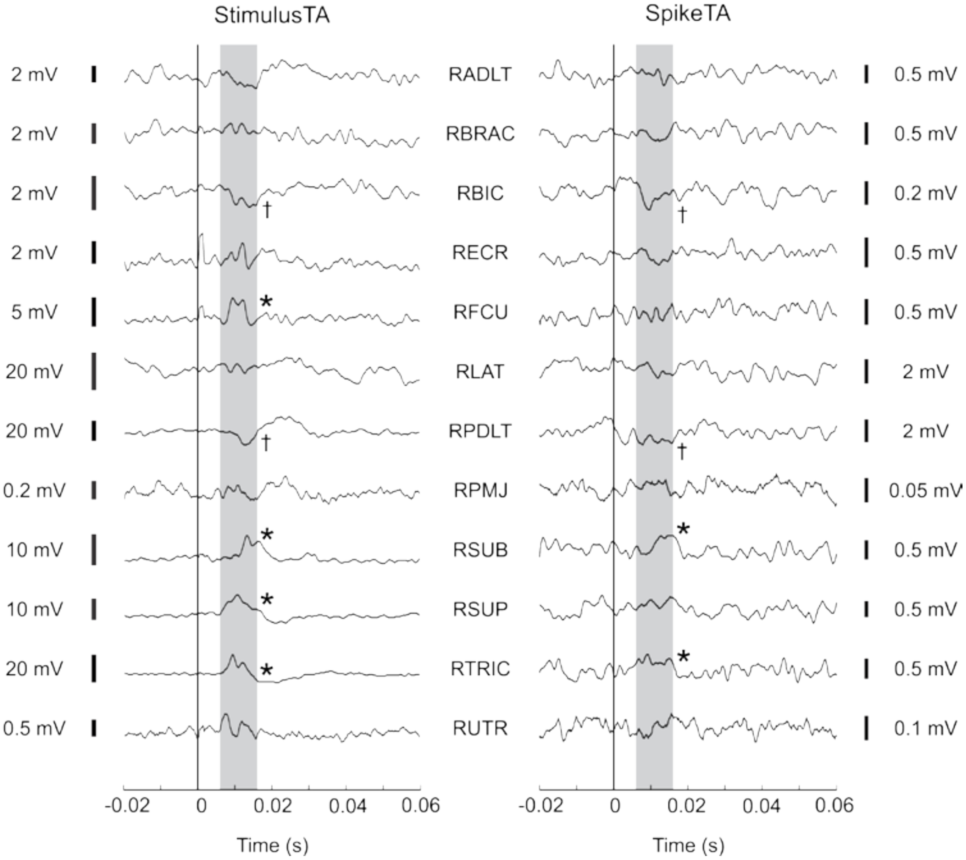

Figure 4.2 Corresponding example of EMG recordings of contralateral flexor suppression and extensor facilitation in response to left-sided PMRF stimulation (StimulusTA, left) or spontaneous spiking (SpikeTA, right). Significant post-stimulus EMG effects are indicated by *asterisks* for PStF and *daggers* for PStS. Scale bars represent indicated voltage changes. For StimulusTA, all averages included at least 1355 triggers; for SpikeTA, all averages included at least 15000 triggers. For StimulusTA, 30 µA stimulation was applied at time 0 s; for SpikeTA, a neuronal spike was detected at time 0 s.

Figure 4.3 *A*: Corresponding example of post-spike force recordings of ipsilateral flexion and contralateral extension in response to left-sided PMRF stimulation (StimulusTA, left) or spontaneous spiking (SpikeTA, right). A 50 Hz high-pass filter was applied to both force traces. *B*: Raw force average and high-pass filtered average. The area shaded in gray represents the 15-ms interval during which there is a maximal change in force in the high-pass filtered StimulusTA averages. Scale bars represent indicated force changes. For StimulusTA, all averages included at least 1355 triggers; for SpikeTA, all averages included at least 24427 triggers. For StimulusTA, a 30 µA electrical pulse was delivered at time 0 s; for SpikeTA, a neuronal spike was detected at time 0 s.

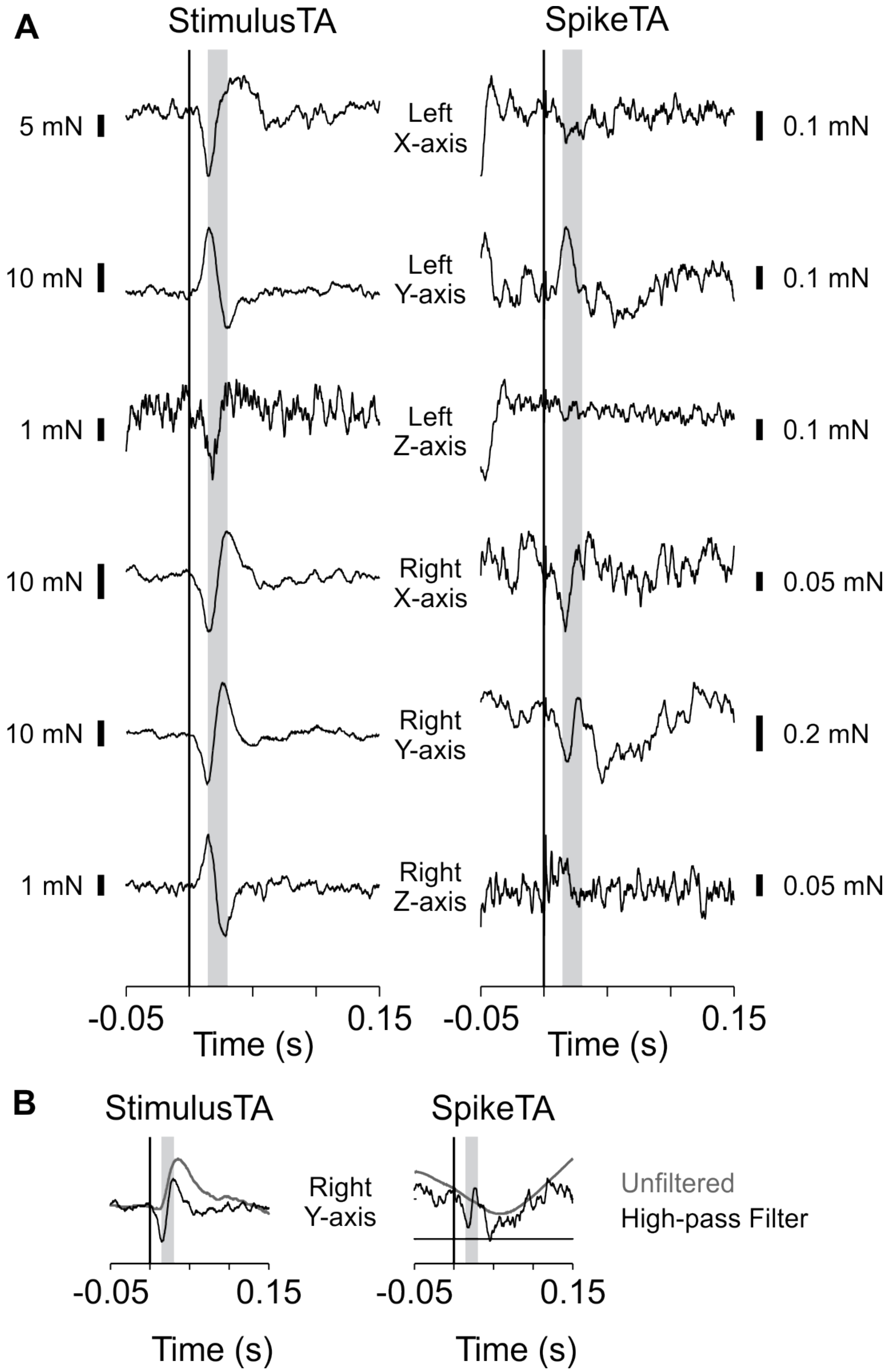

Figure 4.3 Corresponding example of post-spike force recordings of ipsilateral flexion and contralateral extension.

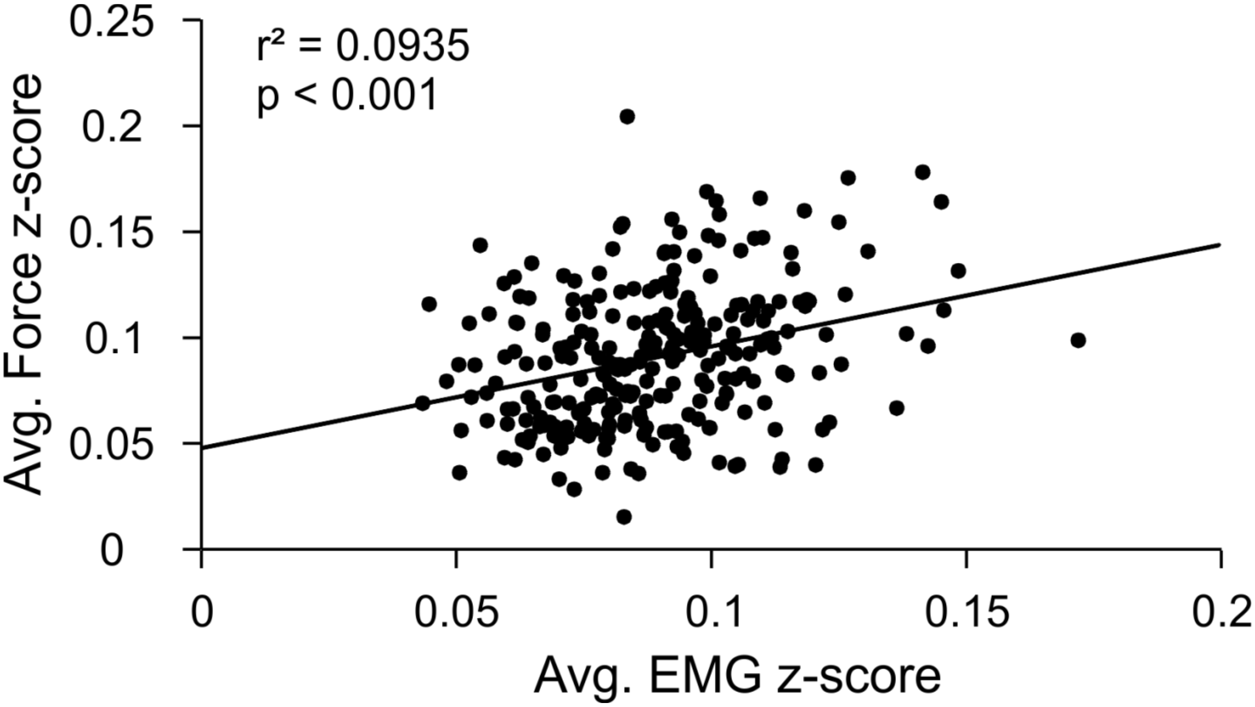

Figure 4.4 Comparison of average z-scores for post-spike EMG activity and average z-scores for post-spike force effects. EMG and forces were significantly correlated. N = 269, $r^2 = 0.094$, $p < 0.001$.

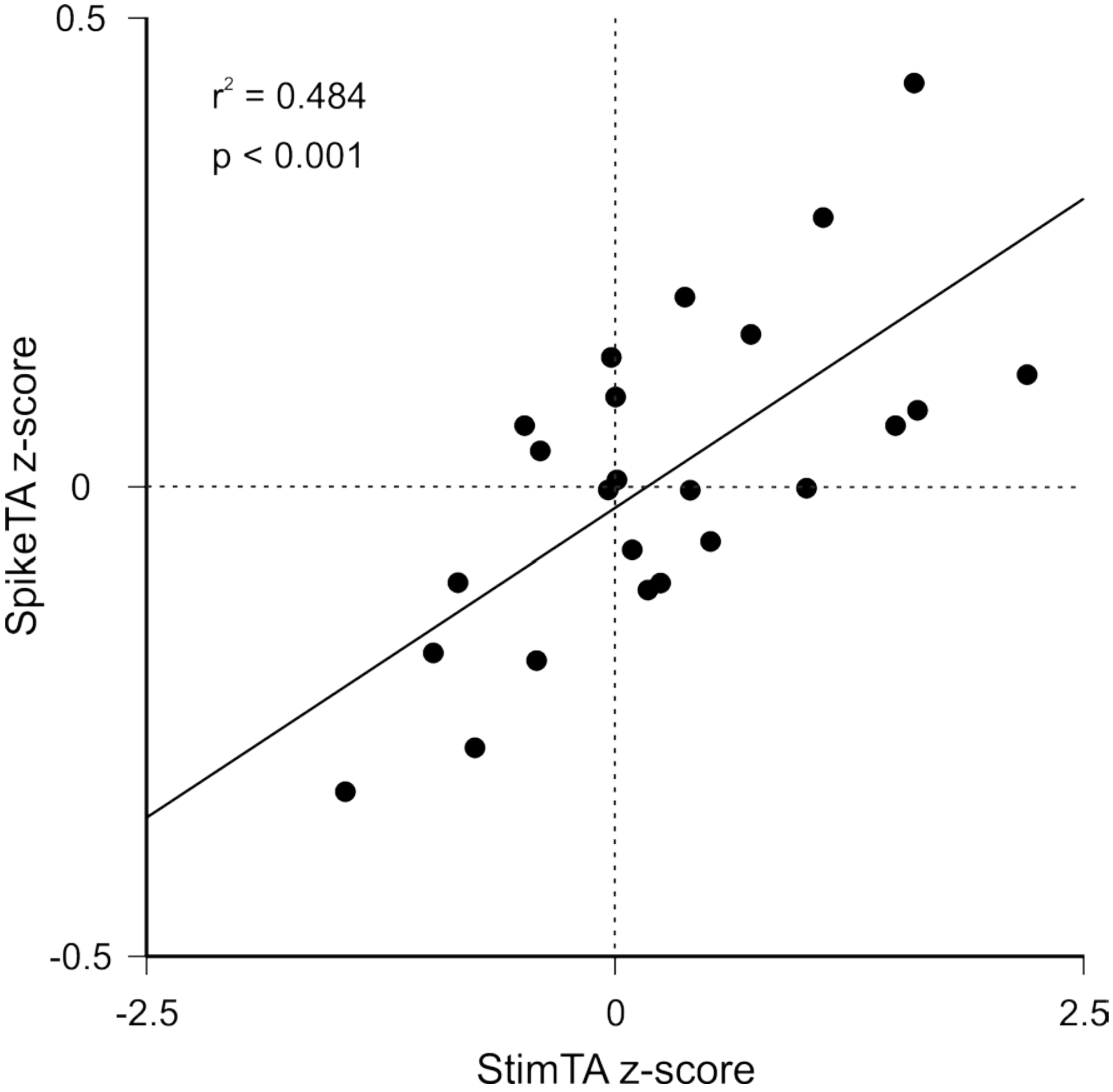

Figure 4.5 Comparison of z-scores for post-spike and post-stimulus EMG effects in 24 muscles. SpikeTA and StimulusTA effects were significantly correlated. For StimulusTA, all averages included at least 1355 triggers; for SpikeTA, all averages included at least 24427 triggers. $r^2 = 0.484$, $p < 0.001$.

Chapter 5: Review of the diagnosis of Parkinson's disease

Parkinson's disease and other movement disorders

Affecting an estimated one million people in the United States, PD is the second most common neurodegenerative disease after Alzheimer's disease (de Lau and Breteler 2006). PD is a movement disorder characterized by tremor, hypokinesia, rigidity, and postural instability (Gelb et al. 1999). Moreover, PD is one of the movement disorders of basal ganglia origin, which also include Huntington's disease, Sydenham's chorea, and hemiballismus (Obeso et al. 2002). Although the etiology of these movement disorders is varied, they all involve damage to basal ganglia circuitry. As previously stated, the motor symptoms of PD are caused by the loss of dopaminergic neurons in the substantia nigra (Obeso et al. 2002). Huntington's disease, which is caused by trinucleotide expansion in the Huntingtin gene, results in widespread neuronal death that disproportionately affects striatal neurons (Walker 2007, Eidelberg and Surmeier 2011). Sydenham's chorea, a sequela of group A β-hemolytic streptococcal (*S. pyogenes*) infection, is caused by an autoimmune-mediated destruction of striatal neurons (Swedo et al. 1993). Hemiballismus, which has multiple etiologies, is caused by damage to the subthalamic nucleus (Postuma and Lang 2003).

Because PD is caused by a deficiency in dopamine-producing neurons, the symptoms of PD are most effectively treated with a dopamine precursor known as L-DOPA (Connolly and Lang 2014). Less widely used drugs include dopamine agonists, monoamine oxidase B inhibitors (MAOBIs), and catechol-O-methyl transferase inhibitors (COMTIs) (Connolly and Lang 2014). However, disease progression is associated with a decrease in drug therapy effectiveness. More severe cases of PD can be managed by strategically delivering electrical stimulation to the thalamus or different nuclei of the basal ganglia in a process known as deep brain stimulation (DBS) (Perlmutter and Mink 2006). Parkinsonian symptoms are significantly alleviated by stimulation to the ventral intermediate nucleus of the thalamus, the subthalamic nucleus, or the internal segment of the globus pallidus (Perlmutter and Mink 2006).

Differential diagnosis of parkinsonism

The diagnosis of PD is complicated by the existence of by other parkinsonian syndromes, such as secondary parkinsonism and APS (Jankovic et al. 2008). Secondary parkinsonism describes a syndrome in which parkinsonian motor symptoms are caused by an identifiably etiology, such as environmental toxins, drugs, metabolic disease, infection, or trauma (Olanow and Tatton 1999). APS are disorders that exhibit classical parkinsonian symptoms, but include additional features distinguishing them from idiopathic PD. Because of these overlapping symptoms, APS are especially difficult to differentiate from PD (Jankovic et al. 2008). It is has been estimated by neuropathological studies using brain bank specimens that 25% of clinical diagnoses of PD are incorrect (Playfer 1997, Tolosa et al. 2006). The most common Parkinson-plus syndromes are multiple system atrophy (MSA), progressive supranuclear palsy (PSP), and corticobasal degeneration (CBD) (Jankovic et al. 2008). Additionally, one in ten patients diagnosed clinically with early PD are later shown to have SWEDDs (Schwingenschuh et al. 2010). Other disorders often included in the differential diagnosis of parkinsonism and possible sources of misdiagnosis are shown in Table 5.1.

The clinical diagnosis of PD requires a diagnosis of parkinsonian syndrome and the absence of any exclusion criteria that would suggest secondary parkinsonism or APS (Gelb et al. 1999). The UK Parkinson's Disease Society Brain Bank and the National Institute of Neurological Disorders and Stroke (NINDS) have both developed criteria for clinical PD diagnosis but these only achieve diagnostic certainty of 75-90% (Gelb et al. 1999; Jankovic 2008). However, these criteria are primarily dependent on motor symptoms and ignore features such as olfactory function and functional neuroimaging results (Gelb et al. 1999). With recent findings that non-motor symptoms can precede the onset of motor symptoms by as much as 20 years, including non-motor symptoms into the assessment can allow for early detection of PD (de Lau and Breteler 2006, Savica et al. 2010). Improved diagnostic methods that result in greater accuracy and earlier detection of disease will allow for patients to be treated sooner with better outcomes (DeKosky and Marek 2003). In additional, the severity of non-motor symptoms, such as autonomic dysfunction, pain, and sleep disturbances, are more strongly correlated with decreased quality of life than motor symptoms (Gallagher et al. 2010). Increased diagnostic and prognostic accuracy requires consideration of supplementary clinical examinations, laboratory tests, and neuroimaging results (Jankovic 2008).

Overview of computer-aided diagnosis and detection

One of the earliest examples of the successful implementation of CAD in a clinical setting was for the diagnosis of acute abdominal pain (de Dombal et al. 1972). Since receiving FDA approval in 1998, CAD has been routinely used in the clinic for breast cancer screening (Doi 2007, Elmore et al. 2005, Noble et al. 2009). CAD for mammography-based breast cancer screening has been shown to increase the recall rate, the proportion of early-stage cancer detected, and the overall number of cancers detected without decreasing the positive predictive value for biopsy (Freer and Ulissey 2001). Other studies estimate that the use of CAD for breast cancer screening is comparable to double reading of mammograms (Bennett et al. 2006, Houssami et al. 2009). In neurology, CAD has been used clinically to differentiate patients with Alzheimer's disease from cognitively intact age-matched controls based on structural MRI scans (Klöppel et al. 2008).

The development of various clinical examinations and neuroimaging analyses has increased the quantity of clinical data available for diagnosis of neurological disorders. With increasing amounts of diagnostic data available to clinicians, it becomes increasingly difficult to generate, internalize, and apply accurate medical algorithms. Machine learning algorithms are capable of considering vast quantities of data during diagnosis and implementing probabilistic reasoning with high precision to determine the likelihood of a given diagnosis based on the symptoms and test results of a patient. Improved diagnostic methods will result in increased sensitivity and earlier detection of disease, allowing patients to be treated sooner.

Various machine learning classification techniques have been utilized in CAD to differentiate between healthy subjects and those with disease (Wang and Summers 2012, Shiraishi et al. 2011, Yousefi and Hamilton-Wright 2014). Some commonly used algorithms are listed in Table 5.2. Support vector machines, illustrated in Figure 5.1, classify unknown cases by finding a hyperplane in the feature space that best separates the training data based on class, then assigning the case to a class based on its location in the feature space relative to the hyperplane (Cortes and Vapnik 1995). The k-nearest neighbors (k-NN) algorithm, illustrated in Figure 5.2, classifies unknown cases by assigning them to the class that matches the plurality of the k training data that are nearest to the unknown case in the feature space. Classification trees classify unknown cases by developing a stepwise flowchart that during each step either assigns the test case to a class based on the value of the current feature or advances to consider the next feature (Cover and Hart 1967, Quinlan 1986).

Computer-aided diagnosis of Parkinson’s disease

Previous studies have investigated the CAD of PD by utilizing certain types of clinical features to differentiate between PD and either healthy controls or other parkinsonian syndromes. Because parkinsonian syndromes are defined by their motor symptoms, many CAD studies have focused on these features. Smith and Timmis (2008) used an evolutionary algorithm to classify subjects based on pen velocity profiles obtained during a figure-copying task performed by PD patients and age-matched controls. Daliri (2013) classified subjects based on gait information collected from force sensors placed underneath the feet of PD subjects and healthy controls. Hauser et al. (2011) used ROC curve analysis to determine minimal clinically important change in total UPDRS for monitoring improvement in PD subjects. MCIC for improvement in total UPDRS score (parts I-III) was reported to be -3.0 points. Merello et al. (2002) tested parkinsonian patients without specific diagnoses using a levodopa challenge. They reported that levodopa challenge predicts clinical diagnosis of PD and that a 30% improvement in UPDRS scores was supportive of PD diagnosis.

Other studies have used neuroimaging, which directly measures changes in brain structure and function, to differentiate between PD, APS, and healthy subjects. Babu et al. (2014) used voxel-based morphometry (Ghosh-Dastidar et al. 2006) to identify voxels with a significant change in tissue volume, concluding that tissue volume changes in the superior temporal gyrus region are most associated with PD. A common neuroimaging technique in PD diagnosis is the use of single positron emission computed tomography (SPECT) to measure the striatal-binding ratio (SBR) of radioactive ioflupane (^{123}I), a compound that binds to presynaptic dopamine transporters. Prashanth et al. (2014) and Martinex-Murcia et al. (2014) distinguished between PD and healthy subjects based on SBR of ioflupane (^{123}I) with accuracy up to 96.1%. Garraux et al. (2013) classified PD and APS subjects more accurately than a nuclear medicine specialist based on 18-FDG positron emission topography (PET) scans. Salvatore et al. (2014) used SVM to classify subjects based on features extracted from PCA of structural MRI from PD, PSP, and healthy control subjects and found that voxels in the midbrain, pons, corpus callosum, and thalamus were most important to classification between PD and PSP patients.

Morales et al. (2013) used a multivariate filter-based naïve Bayes model to predict cognitive function in PD subjects based on structural MRI measurements with 97.0% accuracy. Boelmans et al. (2010) used diffusion tensor imaging (DTI) of the corpus callosum to differentiate PD from CBD.

The inclusion of non-motor clinical features can improve diagnostic accuracy. Armañanzas et al. (2013) identified non-motor PD symptoms that predict disease severity in terms of Hoehn & Yahr (HY) staging and the clinical impression of severity index for PD (CISI-PD). Hallucinations, involuntary loss of stools, and difficulty swallowing were among the features most commonly selected to differentiate between mild and moderate PD. Goldstein et al. (2008) constructed ROC curves to determine the ability to differentiate between PD, MSA, and control subjects based on CSF and plasma catechol concentrations, olfactory function, and PET scans that measure dopaminergic functioning. They reported that both the putamen dopaminergic functioning and olfactory testing were able to differentiate between PD and MSA subjects. However, the use of a combination of motor and non-motor symptoms in the CAD of parkinsonism differentiating between PD, SWEDDS, and healthy subjects has not been investigated.

Tables & Figures

1. *Parkinson's disease* (primary parkinsonism)
2. *Scans without evidence of dopaminergic deficiency* (SWEDDs)
3. *Atypical parkinsonian syndromes* (APS)
    - Multiple system atrophy (MSA)
    - Progressive supranuclear palsy (PSP)
    - Corticobasal degeneration (CBD)
    - Dementia with Lewy bodies (DLB)
    - Frontotemporal dementia and parkinsonism linked to chromosome 17 (FTDP-17)
4. *Secondary parkinsonism*
    - Vascular parkinsonism
    - Toxin-induced parkinsonism
    - Medication-induced parkinsonism
    - Post-infectious parkinsonism
5. *Alzheimer's disease with parkinsonism*
6. *Huntington's disease*
7. *Essential tremor*

Table 5.1 Differential diagnosis of Parkinson's disease. Secondary parkinsonisms are parkinsonian syndromes with a known cause of substantia nigra degeneration. Atypical parkinsonian syndromes are parkinsonian syndromes with additional characteristics distinguishing them from PD (Aerts et al. 2011).

Supervised learning

- Support vector machine (SVM)
- k-Nearest neighbors (k-NN)
- Classification tree (CT)
- Probabilistic neural network (PNN)
- Enhanced probabilistic neural network (EPNN)

Unsupervised learning

- Cluster analysis
    - k-Means clustering
    - Expectation-maximization
    - Gaussian mixture model
- Hidden Markov model
- Principal component analysis

Table 5.2 Machine learning classification algorithms in computer-aided diagnosis. For supervised learning, training data have known class labels. For unsupervised learning, the classes of the data are unknown.

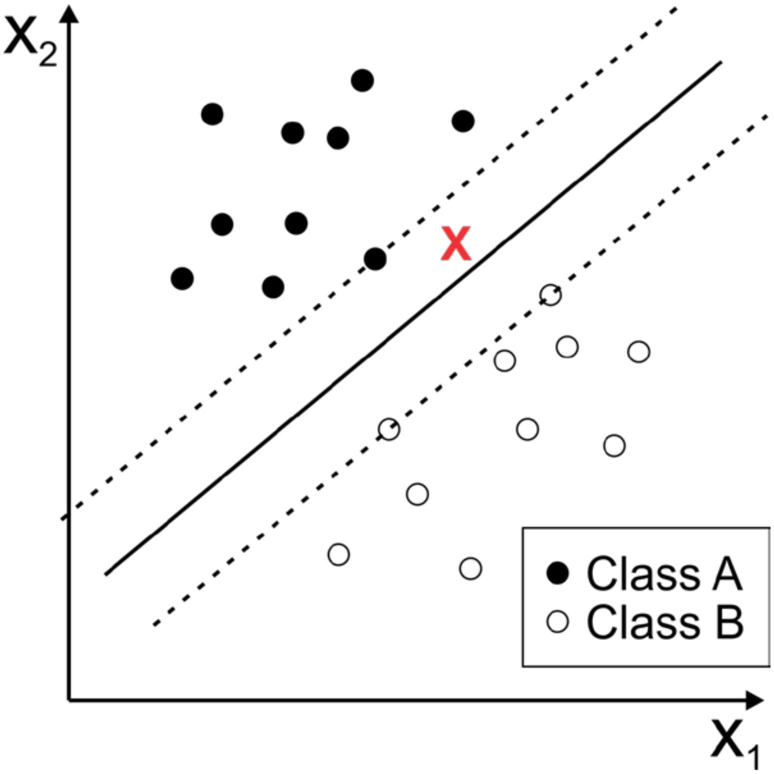

Figure 5.1 Support vector machine classifier. The SVM identifies a line (for two dimensions), plane (for three dimensions), or hyperplane (for higher order dimensions) that separates the members of the two classes on either side and maximizes the margin between any data point and the hyperplane. The maximum margin line (solid black) is equidistant from the nearest cases of either class. A test case, indicated by the red X, would be assigned to class A because it is located on the same side of the classification line as the training cases from class A. *Filled circles*, class A; *open circles*, class B.

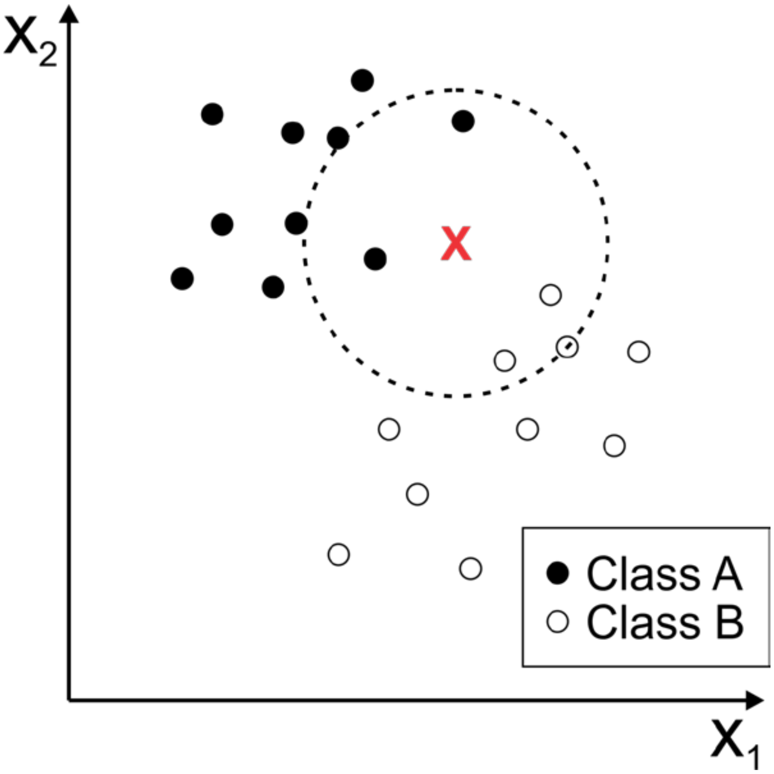

Figure 5.2 k-Nearest neighbors classifier. The k-NN algorithm calculates the Euclidean distances between the test case and the training cases and then determines the nearest *k* training cases to the test case. The test case is assigned to the class that makes up the plurality of the *k* nearest training cases. For $k = 5$, a test case, indicated by the red X, would be assigned to class B because 3 of the 5 nearest training cases are members of class B. *Filled circles*, class A; *open circles*, class B.

Chapter 6: Computer-aided diagnosis of Parkinson’s disease using an enhanced probabilistic neural network

Introduction

PD is caused by degeneration of dopaminergic neurons in the substantia nigra, which leads to a characteristic set of motor symptoms – tremor, hypokinesia, rigidity, and postural instability – known as parkinsonism (Davie 2008). Although PD commonly presents with these classic motor deficits, early and accurate diagnosis remains challenging (Jankovic et al. 2008). In fact, neuropathological studies using brain bank specimens have estimated that 25% of clinical diagnoses of PD are incorrect (Tolosa et al. 2006). One reason for this difficulty is the presence of SWEDDs and APS, summarized in Table 5.1, which present with parkinsonism but have secondary features distinguishing them from PD.

Approximately 10% of patients diagnosed clinically with early PD have normal dopaminergic functional imaging (Schwingenschuh et al. 2010). Based on their imaging results, these patients are classified as having SWEDDs. These patients have been hypothesized to have an atypical presentation of dopa-responsive dystonia (DRD) instead of PD (Schneider et al. 2007, Marek and Seibyl 2003, De Rosa et al. 2014). Distinguishing between PD and SWEDDs is difficult because patients present with similar motor symptoms (Lee et al. 2014). However, recent studies have identified a difference between some non-motor symptoms of PD and SWEDDs patients (Yang et al. 2014).

Since the 1970s, artificial intelligence and machine learning techniques (Adeli and Hung 1995) have been employed to aid clinicians in improving diagnostic accuracy (de Dombal et al. 1972). Because of the complicated nature of PD diagnosis, these techniques can provide specific benefit to neurologists considering the differential diagnosis of parkinsonism (Jankovic et al. 2008). Some studies have used CAD to differentiate PD from APS. For instance, a recent study used a support vector machine (SVM) to differentiate between 28 subjects with PD, 28 subjects with progressive supranuclear palsy (PSP), and 28 healthy controls (HC) using structural MRI data (Salvatore et al. 2014). They report a classification accuracy of 92.5% for PD vs. PSP and 92.7% for PD vs. HC. Illan et al. (2012) analyzed dopaminergic functional imaging of 108 parkinsonian syndrome subjects and 100 health controls. They reported 89.0% sensitivity and 93.2 % specificity using an SVM classifier.

Machine learning techniques have also proven useful in prognosis and disease tracking. Machine learning algorithms were used to predict the development of dementia in PD patients based on structural MRI and identified structural changes most predictive of cognitive decline (Morales et al. 2013). Because PD patients often exhibit vocal symptoms that include impairment in the production of vocal sounds, vocal recording can be used to track disease progression of PD patients (Little et al. 2009, Rahn et al. 2007). Various studies have used machine learning techniques for the automated remote tracking of PD disease progression.

Publicly available data from PD and control subjects like those from the Parkinson’s Progression Marker Initiative (PPMI) database (Marek et al. 2011) have helped facilitate PD research. Recent studies utilizing the PPMI database have examined the feasibility of using neuroimaging data for the CAD of PD. For instance, Babu et al. (2014) report a classification accuracy of 82.3% using a meta-cognitive radial basis function (RBF) network classifier to distinguish between PD subjects and healthy controls based on structural MRI data. Similarly dopaminergic functional neuroimaging data has been used to classify PD vs. HC subjects using an SVM classifier (Martinez-Murcia et al. 2014, Prashanth et al. 2014). However, no studies have used motor, non-motor, and neuroimaging features simultaneously for the CAD of parkinsonism.

In this chapter, a comprehensive model is presented for the diagnosis of PD based on motor, non-motor, and neuroimaging features using the recently-developed enhanced probabilistic neural network (EPNN). The model’s ability to differentiate PD from SWEDDs and healthy controls is tested using the PPMI dataset. Differentiating PD from SWEDDs presents similar diagnostic challenges as other non-PD parkinsonian syndromes. Additionally, the results are compared to four other commonly-used machine learning algorithms: the probabilistic neural network (PNN), SVM, k-nearest neighbors (k-NN) algorithm, and classification tree (CT).

Methods

Description of data

Data used in this study were obtained from the Parkinson’s Progression Markers Initiative (PPMI) database (www.ppmi-info.org/data). For up-to-date information on the study, visit www.ppmi-info.org. PPMI (Marek et al. 2011) is an observational, multi-center, international study designed to identify PD biomarkers for diagnosis and disease progression. To be included in the study, the subjects are required to have results for six clinical exams and functional neuroimaging data for two brain regions of interest. The 8 diagnostic tests are summarized in Table 6.1. The six clinical examinations are: 1.) the Movement Disorder Society-sponsored revision of the United Parkinson’s Disease Rating Scale (MDS-UPDRS) Part I, which consists of 13 items and assesses the non-motor experiences of daily living; 2.) the MDS-UPDRS Part II, which consists of 13 items and assesses motor experiences of daily living; 3.) the MDS-UPDRS Part III, which consists of 18 items and assesses motor function; 4.) the Montreal Cognitive Assessment (MoCA), which consists of 26 items and assesses cognitive function; 5.) the Scales for Outcomes in Parkinson’s disease – Autonomic (SCOPA-AUT), which consists of 21 items and assesses autonomic function; and 6.) the University of Pennsylvania Smell Identification Test (UPSIT), which consists of 4 items and assesses olfactory function.

For clinical examinations 1, 2, and 3, each item is assigned a score between 0 (normal) and 4 (most severe) for a maximum total score of 52, 52, and 72, respectively (Goetz et al. 2008). For examination 4, the maximum possible score on each item varies between 1 and 3 (higher scores indicating better cognitive function) for a maximum total score of 30, with a score of less than 26 indicative of impaired cognitive function. For examination 5, each item is assigned a score between 0 (normal) and 3 (most severe), for a maximum score of 105 with a score of greater than approximately 15 suggestive of impaired autonomic function (Visser et al. 2004). In order to eliminate bias based on differences in disease prevalence between sexes, the sex-specific questions of examination 5 are excluded. Finally, for examination 6, a score of 0 (all incorrect) to 10 (perfect) is assigned to each of the 4 items for a total score of 40, with a score of less than 35 (for men) or 36 (for women) indicative of impaired olfactory function (Doty et al. 1984). For each examination, a final test score is calculated by summing the values for all of the items included in that examination. Neurologists use these kinds of clinical examinations to grade patients using a standardized metric and to determine if the patient's functioning is within normal limits. However, on their own, these clinical examinations are not sufficient for any specific diagnosis.

For neuroimaging, the two brain regions of interest are the caudate nucleus and the putamen, which together constitute the striatum, the part of the basal ganglia that receives dopaminergic inputs from the substantia nigra. For each region of interest, single positron emission computed tomography (SPECT) was used to measure the striatal-binding ratio (SBR) of ioflupane (^{123}I), a radioactive compound that binds to presynaptic dopamine transporters. The striatal binding ratio compares the average signal intensity of ioflupane (^{123}I) in the region of interest (caudate or putamen) to the average signal intensity in the occipital lobe as a control region. Thresholds distinguishing PD from healthy subjects have not previously been characterized.

Of the 1141 subjects available in the PPMI database, the 666 subjects (58.4%) that have received all of the aforementioned diagnostic tests are included in this study. Of the 666 subjects included in the study, 189 subjects (28.4 %) are diagnosed with PD, 62 subjects (9.3%) exhibited SWEDDs, and the remaining 415 subjects (62.3%) are healthy controls. The exclusion rates of subjects do not significantly differ between classes.

Probabilistic neural network

A PNN is a feedforward neural network with four layers: an input layer, a pattern layer, a summation layer, and an output layer (Specht 1990), shown in Fig. 1 for the classification of HC, SWEDDs, and PD subjects using the PPMI database. The PNN classifies test cases by applying a Gaussian radial basis function (RBF) to the Euclidean distance between the test case and each training case, finding the average RBF output for all training cases of each class, and then assigning the case to the class with the highest average. The d neurons in the input layer correspond to the elements of the d-dimensional input vector. The number of neurons in the pattern layer, N, corresponds to the number of cases in the training data. The i neurons in the summation layer correspond to the i classification categories. These neurons receive input only from the N_i pattern layer neurons corresponding to training cases from that category. The decision layer has one neuron that determines which neuron in the summation layer has the greatest output. For the PPMI database each input vector consists of 8 elements – the scores from 6 clinical examinations and 2 neuroimaging measurements, summarized in Table 6.1.

For each pattern layer neuron, a Gaussian kernel is applied to the Euclidean distance from the test case to estimate the likelihood of the test case being from the same class as the training case represented by the pattern layer neuron according to the equation:

$$\varphi_{ij}(y) = \frac{1}{(2\pi)^{d/2}\sigma^d} e^{-\frac{(y-x_{ij})^T(y-x_{ij})}{2\sigma^2}} \tag{1}$$

where $\varphi_{ij}(y)$ is the kernel function for input vector y and the j^{th} pattern layer neuron from class i, y is the input vector, x_{ij} is feature vector for the j^{th} pattern layer neuron from class i, and σ is the spread parameter of the Gaussian kernel. The value of $\varphi_{ij}(y)$ obtained from Eq. (1) is then fed only to the summation layer neuron that corresponds to the class, i, of that training case according to the equation:

$$P_i(y) = \frac{1}{N_i}\sum_{j=1}^{N_i} \varphi_{ij}(y) \tag{2}$$

where $P_i(y)$ represents the likelihood that the test case y belongs to class i. Lastly, the output layer neuron determines the summation layer neuron with the greatest sum according to the equation:

$$Class(y) = \arg\max_i\{P_i(y)\} \tag{3}$$

Enhanced probabilistic neural network

In order to improve the classification accuracy of PNN, Ahmadlou and Adeli (2010a) developed the Enhanced Probabilistic Network (EPNN) model with local decision circles by modifying the spread of the Gaussian kernel based on the local heterogeneity of the training set. For each case in the training set, the local heterogeneity,

$\alpha_{x_{ij}}$, is calculated by determining the proportion of all training cases within a hypersphere of radius, r, that are of the same class as the central training case, x_{ij}, according to the following equation:

$$\alpha_{x_{ij}} = P\left[x \in Class(x_{ij}) | x \in S_{r,x_{ij}}\right] \quad (4)$$

In the EPNN, the spread parameter, σ, for each neuron in the pattern layer is adjusted according to the equation:

$$\sigma_{x_{ij}} = \alpha_{x_{ij}} \times \sigma \quad (5)$$

The optimal values for the spread parameter, σ, and local decision circle radius, r, are determined empirically.

Reference classification algorithms for comparison

In addition to the EPNN, four other commonly used supervised learning techniques were implemented to provide a benchmark for comparison of diagnostic performance: PNN, SVM, k-NN, and CT classification algorithms. Because the SVM is only capable of binary classification, it is not used for the ternary classification of PD, SWEDDs, and HC subjects. PNN was described previously. Brief descriptions of the other three techniques are provided here.

The SVM algorithm classifies each test case by finding a hyperplane in the feature space that best separates the training data based on class, then assigning the test case to a class based on its location in the feature space relative to the hyperplane. The k-NN algorithm classifies each test case by assigning it to the class that matches the majority of the k training data that are nearest to the test case in the feature space as measured by Euclidean distance. The CT algorithm classifies each test case by making a series of decisions, represented by nodes on the tree, that assign test cases to one of a number of branches. Each branch leads to either another node, where another decision is made, or to a leaf, where a final classification is assigned.

Receiver operating characteristics of clinical exams

The ability of eight diagnostic tests (Table 6.1) to individually differentiate between disease states is examined using receiver operating characteristic (ROC) curves. For each diagnostic test, an ROC curve is plotted for the three binary comparisons (PD vs. HC, SWEDDs vs. HC, and PD vs. SWEDDs). ROC curves are created by plotting the true positive rate against the false positive rate of a diagnostic test while varying the classification threshold across the entire range of possible test scores. The classification threshold is the cutoff value that is used to decide which class the subjects are assigned to. The area under the ROC curve (AUC) gives a measure of diagnostic performance, with 1.0 indicating that the test perfectly separates the two classes and 0.5 indicative of a completely uninformative test. The percentile confidence intervals are derived from a bootstrap distribution. The ROC analysis is also used to determine the threshold score that maximizes classification accuracy for each diagnostic test. This is then compared to the maximum classification accuracy achieved by machine learning algorithms that use all items as individual inputs instead of considering only the sum of all the item scores.

Modeling the EPNN

The number of neurons in the input layer of the EPNN matches the number of diagnostic features used for classification. For the PPMI database, the feature set consists of 8 inputs (6 clinical exams and 2 neuroimaging measurements). For each classification problem, approximately 90% of the data are used for training and 10% are used for testing as indicated in Table 6.2. Subjects are assigned to the training or testing group randomly. For cross-validation, the process is repeated 100 times, and the average values are reported in the paper. Training and test data ranges were standardized by subtracting the median and dividing by the interquartile range for each input feature.

To test the model in different clinical scenarios, both ternary and pairwise binary classifications are performed. The number of neurons in the pattern layer is equal to the number of training cases. This varies depending on whether a ternary or binary classification is performed and, for binary classifications, which two classes are being classified. In the ternary classification the number of neurons in the pattern layer is equal to the entire number of training instances available, that is, 599 (Table 6.2). There are 3 neurons in the summation layer representing the three potential class assignments (PD, SWEDDs, and HC).

For the binary classifications, the number of neurons in the pattern layer is 544 for the PD vs. HC classification, 226 for the SWEDDs vs. HC classification, and 429 for the PD vs. SWEDDs classification as summarized in Table 6.2. There are 2 neurons in the summation layer corresponding to the two potential class assignments (PD/HC, SWEDDs/HC, or PD/SWEDDs) for each classification pair. Lastly, for both ternary and binary classifications, there is one neuron in the decision layer which provides the final class assignment for each test case. All algorithms and calculations have been implemented in Matlab.

Measures of diagnostic performance

Classification results from the ternary classification are expressed in the form of an error matrix, or contingency table, in which each column indicates the assigned classes of the test data and each row indicates the actual class. Therefore, the number of correctly assigned cases is equal to the sum of the values along the main diagonal. The *accuracy* of a diagnostic test is defined as the ratio of the number of correct assignments to the total number of cases. Error matrices also show whether certain types of errors in classification are more likely to occur than others, for example if PD subjects are more likely to be misclassified as SWEDDs than as HC.

For binary classification, the *sensitivity*, or true positive rate, is defined as the proportion of positive cases that are correctly identified as positive; and the *specificity*, or true negative rate, is defined as the proportion of negative cases that are correctly identified as negative. Since accuracy calculations can report an inflated estimate of performance for datasets with an imbalanced number of cases and controls, a *balanced accuracy* metric is also defined as the arithmetic mean of the sensitivity and specificity.

Results

Classification accuracy of individual diagnostic tests

The receiver operating characteristic curves were created for all 8 diagnostic tests (6 clinical examinations, 2 neuroimaging measurements). The areas under the ROC curves for each test are reported in Table 6.3 and the maximum balanced accuracies are reported in Table 6.4. The most accurate tests for each binary classification are the MDS-UPDRS Part III for PD vs. HC, the MDS-UPDRS Part III for SWEDDs vs. HC, and the putamen SBR for PD vs. SWEDDs.

Figure 2 shows the ROC curve and classification accuracy for the MDS-UPDRS Part III. The MDS-UPDRS Part III exam is most effective at differentiating PD vs. HC (AUC = 0.997, Acc. = 97.0%) and SWEDDs vs. HC (AUC = 0.973, Acc. = 91.0%), but is less effective at differentiating PD vs. SWEDDs (AUC = 0.698, Acc. = 65.8%). The MDS-UPDRS Part II, which also assesses motor function, is similarly effective at differentiating PD vs. HC (AUC = 0.968, Acc. = 89.0%) and SWEDDs vs. HC (AUC = 0.957, Acc. = 86.6%), but is not effective at differentiating PD vs. SWEDDs (AUC = 0.560, Acc. = 57.1%). The MDS-UPDRS Part I, which assesses non-motor function, is better at differentiating SWEDDs vs. HC (AUC = 0.810, Acc. = 71.2%) than PD vs. HC (AUC = 0.739, Acc. = 67.7%), but is less effective at differentiating PD vs. SWEDDs (AUC = 0.581, Acc. = 62.5%).

Figure 3 shows the ROC curve and classification accuracy for the putamen SBR. The putamen SBR is very effective at differentiating PD vs. HC (AUC = 0.987, Acc. = 95.8%) and PD vs. SWEDDs (AUC = 0.974, Acc. = 93.7%), but does not significantly differentiate SWEDDs vs. HC (AUC = 0.557, Acc. = 58.6%). The caudate SBR is also effective at differentiating PD vs. HC (AUC = 0.897, Acc. = 81.2%) and PD vs. SWEDDs (AUC = 0.853, Acc. = 78.6%), but similarly does not significantly differentiate SWEDDs vs. HC (AUC = 0.559, Acc. = 55.8%).

Figure 4 shows the ROC curve and classification accuracy for the UPSIT. The UPSIT is the clinical examination that best differentiates PD vs. SWEDDs (AUC = 0.794, Acc. = 74.4%), while also significantly differentiating PD vs. HC (AUC = 0.898, Acc. = 82.4%) and SWEDDs vs. HC (AUC = 0.664, Acc. = 61.0%). MoCA is moderately effective at differentiating PD vs. HC (AUC = 0.620, Acc. = 66.4%) and SWEDDs vs. HC (AUC = 0.616, Acc. = 64.8%), but does not significantly differentiate PD vs. SWEDDs. SCOPA-AUT significantly differentiates SWEDDs vs. HC (AUC = 0.781, Acc. = 72.8%) and PD vs. SWEDDs (AUC = 0.612, Acc. = 62.0%), with SWEDDs associated with a higher SCOPA-AUT score than PD.

Machine learning classification

The results of the computer-aided diagnosis classification using five different ML algorithms are summarized in Table 6.5. The EPNN resulted in the highest classification accuracy for the ternary classification with 92.5% accuracy followed by PNN (91.6%), k-NN (90.8%), and CT (90.2%). The error matrix for the EPNN ternary classification is given in Table 6.7. The classification accuracy of 92.5% is calculated by summing the percentages along the main diagonal. The EPNN used a spread parameter, σ, of 0.44 and a radius, r, of 0.72. Fig. 5 shows the diagnostic accuracy versus the spread parameter for the PNN, which is the first step in the bi-level optimization of the EPNN. Fig. 6 shows the diagnostic accuracy versus the decision circle radius for the EPNN. Because binary classification has fewer opportunities for misclassification than ternary, the binary classification generally resulted in higher accuracies.

The results of the clinical screening for SWEDDs are summarized in Table 6.6. The EPNN exhibited the highest classification accuracy for the ternary classification with 89.2% accuracy followed by k-NN (88.8%), CT (88.5%), and PNN (84.0%). However, to improve its utility as a screening tool, the parameters of the PNN/EPNN were chosen to maximize the balanced classification accuracy. The error matrix for this EPNN is given in Table 6.8. The balanced classification accuracy of 75.3% is determined by calculating the mean classification accuracy among all 3 classes. The sensitivity of the SWEDDs classification was 59.0%, and the specificity was 85.9%. The EPNN used a spread parameter, σ, of 0.44 and a radius, r, of 0.08.

Discussion

Classification accuracy of individual diagnostic tests

The MDS-UPDRS Part III, a clinical examination that assesses motor function, was most effective at differentiating between HC and other classes, as shown in Tables 6.3 and 6.4 and Fig. 2. It was less effective at differentiating between PD and SWEDDs, but still performed significantly above chance. Based on the area under the receiver operating characteristic curve and the binary classification accuracies, the MDS-UPDRS Part III was significantly more effective than the SCOPA-AUT, which assesses autonomic function, and the MoCA which assesses cognitive function, at differentiating HC vs. PD, HC vs. SWEDDs, and SWEDDs vs. PD, shown in Tables 6.3 and 6.4. These findings indicate that the deficits in motor function are the most predictive clinical symptom for PD compared to both HC and SWEDDs subjects.

The caudate and putamen ioflupane (^{123}I) SBRs, which analyze dopaminergic functioning of striatal neurons, were most effective at differentiating between subjects with PD and other classes, as shown in Tables 6.3 and 6.4. However, they were not successful at differentiating between HC and SWEDDs. The putamen SBR, shown in Fig. 3, was significantly more accurate than the caudate SBR for all classification types. These results suggest a more consistent decrease in putamen dopamine transporter binding compared to the caudate for subjects with PD. The putamen SBR distinguished between SWEDDs and PD subjects with 93.7% accuracy; however, obtaining these SBR measurements requires subjects to be injected with a radioactive tracer followed by expensive SPECT imaging, which may limit its cost-effectiveness in clinical use.

Of all the clinical examinations studied, the UPSIT best differentiated PD vs. SWEDDs, while also significantly differentiating PD vs. HC and SWEDDs vs. HC, shown in Tables 6.3 and 6.4. Because of the greater ability of UPSIT to differentiate SWEDDs vs. PD subjects compared to MDS-UPDRS Part III, this could be an important indicator of the likelihood of SWEDDs, and a useful figure in determining the need for ioflupane (^{123}I)/SPECT imaging to determine SBR.

The receiver operating characteristic curve for MoCA indicated decreased cognitive function in both SWEDDs and PD subjects, but without a significant difference between the two classes. The receiver operating characteristic curve for SCOPA-AUT indicates that SWEDDs subjects have autonomic functioning that is not intermediate to HC and PD subjects, but instead significantly worse than those for PD subjects. This finding supports the hypothesis that SWEDDs subjects are not an early stage of PD, but represent a different etiology.

Computer-aided diagnosis of parkinsonism

The computer-aided diagnosis using all diagnostic tests was shown to perform well for both the ternary classification (92.5% accuracy) and for the main binary classification of interest, HC vs. PD (98.6% accuracy). For all classification types, the EPNN exhibited the highest classification accuracy compared to other machine learning algorithms, as shown in Table 6.5. The error matrix for the EPNN ternary classification is given in Table 6.7. The majority of all misclassifications were of SWEDDs subjects (54.9%), calculated by dividing the percentage of misclassifications of SWEDDs subjects (4.1%) by the percentage of all misclassifications (7.5%). Approximately 27.0% of SWEDDs subjects were misclassified as HC. HC was misclassified least often, with only 1.7% of HC cases classified as either SWEDDs or PD.

Clinical screening for further examination of potential SWEDDs subjects

SWEDDs and PD subjects are difficult to differentiate based on classic motor symptoms alone (Lee et al. 2014). However, other studies have identified differences in gait between the two classes (Mian et al. 2011). The present study has shown that

SWEDDs and PD subjects can be differentiated above chance using all features except for cognitive function. This supports previous findings that non-motor symptoms differ between SWEDDs and PD subjects (Yang et al. 2014, Silveira-Moriyama et al. 2009).

While the putamen SBR was shown to be the most accurate test in differentiating between SWEDDs and PD, ioflupane (^{123}I)/SPECT imaging is expensive and time-consuming compared to clinical examinations. Clinical screening of subjects to identify those with a high likelihood of SWEDDs could decrease costs by limiting the number of patients that obtain neuroimaging. The clinical screening was performed by using only the 6 clinical examinations as inputs for the machine learning algorithms. The results are given in Table 6.6. For the ternary classification, the EPNN exhibited the highest classification accuracy at 89.2%, which was 3.3 percentage points lower than when all diagnostic tests were included. The balanced classification accuracy was 75.3%, calculated by finding the mean classification accuracy across all 3 classes, shown in Table 6.8. The sensitivity of the SWEDDs clinical screening was 59.0%, and the specificity was 85.9%.

Clinical examinations	*Abbr.*	*Functions assessed*	*Item #*
Motor Disorder Society-sponsored revision of the Unified Parkinson’s Disease Rating Scale Part I	MDS-UPDRS Part I	Non-motor tasks of daily living	13
Motor Disorder Society-sponsored revision of the Unified Parkinson’s Disease Rating Scale Part II	MDS-UPDRS Part II	Motor tasks of daily living	13
Motor Disorder Society-sponsored revision of the Unified Parkinson’s Disease Rating Scale Part III	MDS-UPDRS Part III	Motor function	18
Montreal Cognitive Assessment	MoCA	Cognitive function	26
Scales for Outcomes in Parkinson's disease – Autonomic	SCOPA-AUT	Autonomic function	21
University of Pennsylvania Smell Identification Test	UPSIT	Olfactory function	4
Neuroimaging measurements			
Caudate ioflupane (^{123}I) Striatal Binding Ratio	SBR-Caud	Caudate dopaminergic functioning	2
Putamen ioflupane (^{123}I) Striatal Binding Ratio	SBR-Put	Putamen dopaminergic functioning	2

Table 6.1 Parkinson’s Progression Markers Initiative (PPMI) subject data. The data used in this study consists of six clinical examinations and neuroimaging measurements of two regions of interest.

Classification type	Classes	Training	Testing	Total cases
Ternary	PD/SWEDDs/HC	599	67	666
Binary	PD/HC	544	60	604
Binary	SWEDDs/HC	226	25	251
Binary	PD/SWEDDs	439	48	477

Table 6.2 Numbers of training and test data cases by classification type. Because of the different numbers of subjects per class, the numbers of training and test cases differ between classification types. Of the binary classifications, the PD vs. HC classification has the most subjects (604 total), while the SWEDDs vs. HC classification has the least subjects (251 total).

Diagnostic test	PD vs. HC	SWEDDs vs. HC	PD vs. SWEDDs
MDS-UPDRS I	0.74 (0.68-0.76)	*0.81 (0.69-0.87)*	0.58 (0.54-0.71)
MDS-UPDRS II	*0.97 (0.94-0.97)*	0.96 (0.90-0.97)	0.56 (0.46-0.62)
MDS-UPDRS III	***1.00 (0.99-1.00)***	**0.97 (0.95-0.99)**	0.70 (0.62-0.78)
MoCA	*0.62 (0.58-0.67)*	0.62 (0.52-0.73)	0.51 (0.43-0.58)
SCOPA-AUT	0.70 (0.66-0.75)	*0.78 (0.71-0.84)*	0.61 (0.54-0.69)
UPSIT	*0.90 (0.87-0.92)*	0.66 (0.59-0.74)	0.79 (0.74-0.86)
Caudate SBR	*0.90 (0.87-0.92)*	0.56 (0.45-0.66)	0.85 (0.80-0.90)
Putamen SBR	*0.99 (0.98-0.99)*	0.56 (0.48-0.64)	**0.97 (0.95-0.99)**

Table 6.3 Area under the ROC curves of binary classifications for each diagnostic test. The test that most effectively differentiated between PD vs. HC and SWEDDs vs. HC was the MDS-UPDRS Part III, while the test that best differentiated PD vs. SWEDDs was the putamen SBR (bold). The MDS-UPDRS Parts II and III; MoCA; UPSIT; caudate SBR; and putamen SBR were most effective at differentiating PD vs. HC, whereas the MDS-UPDRS Parts I and SCOPA-AUT was most effective at differentiating SWEDDs vs. HC (italics). Parentheses indicate 95% bootstrap confidence intervals.

Diagnostic test	PD vs. HC	SWEDDs vs. HC	PD vs. SWEDDs
MDS-UPDRS I	67.7%	*71.2%*	62.5%
MDS-UPDRS II	*89.0%*	86.6%	57.1%
MDS-UPDRS III	***97.0%***	**91.0%**	65.8%
MoCA	*66.4%*	64.8%	53.2%
SCOPA-AUT	66.0%	*72.8%*	62.0%
UPSIT	*82.4%*	61.0%	74.4%
Caudate SBR	*81.2%*	55.8%	78.6%
Putamen SBR	*95.8%*	58.6%	**93.7%**

Table 6.4 Balanced accuracies of binary classifications for each diagnostic test. The test that most accurately differentiated between PD vs. HC and SWEDDs vs. HC was the MDS-UPDRS Part III, while the test that most accurately differentiated PD vs. SWEDDs was the putamen SBR (bold). The MDS-UPDRS Parts II and III; MoCA; UPSIT; caudate SBR; and putamen SBR were most accurate at differentiating PD vs. HC, whereas the MDS-UPDRS Parts I and SCOPA-AUT was most accurate at differentiating SWEDDs vs. HC (italics).

	Ternary	Binary		
Diagnostic test	PD/SWEDDs/ HC	PD/HC	SWEDDs/HC	PD/SWEDDs
CT	90.2%	96.5%	89.2%	94.2%
SVM	n/a	98.1%	89.0%	89.3%
k-NN	90.8%	98.2%	91.6%	94.7%
PNN	91.6%	97.9%	91.6%	94.6%
EPNN	**92.5%**	**98.6%**	**92.0%**	**95.3%**

Table 6.5 Classification accuracies of machine learning algorithms using inputs from all 8 diagnostic tests. The EPNN yielded the highest classification accuracy for both binary and ternary classifications.

	Ternary	Binary		
Diagnostic test	PD/SWEDDs/ HC	PD/HC	SWEDDs/HC	PD/SWEDDs
CT	88.5%	97.1%	90.6%	85.3%
SVM	n/a	96.4%	88.0%	85.4%
k-NN	88.8%	96.7%	92.3%	86.2%
PNN	84.0%	97.0%	92.2%	83.8%
EPNN	**89.2%**	**97.2%**	**93.6%**	**86.8%**

Table 6.6 accuracies of machine learning algorithms using only inputs from the 6 clinical examinations. The lack of neuroimaging results decreases the ability of the algorithms to correctly classify subjects. The EPNN yielded the highest classification accuracy for both binary and ternary classifications.

		Assigned Class			
		HC	SWEDDs	PD	Total
Actual Class	HC	28.9%	0.4%	0.2%	29.5%
	SWEDDs	2.7%	5.9%	1.4%	10.0%
	PD	1.4%	1.5%	57.7%	60.6%
	Total	33.0%	7.8%	59.3%	100.0%

Table 6.7 Error matrix for ternary classification for EPNN with all tests as inputs. The overall classification accuracy was 92.5%, calculated by summing the percentages along the shaded diagonal. The non-shaded cells in the 3x3 matrix represent the 6 different ways to misclassify a subject. The majority of all misclassifications (54.9%) were of SWEDDs subjects, with 27.0% of SWEDDs subjects classified as HC. HC cases were misclassified least often, with only 1.7% of HC cases classified as either SWEDDs or PD.

			Assigned Class		
		HC	SWEDDs	PD	Total
Actual Class	HC	27.8%	0.9%	0.2%	28.9%
	SWEDDs	1.6%	5.4	2.2%	9.1%
	PD	4.8%	11.9%	45.3%	62.0%
	Total	34.2%	18.2%	47.6%	100.0%

Table 6.8 Error matrix for SWEDDs clinical screening using EPNN with only clinical examinations as inputs. The balanced classification accuracy was 75.3%, calculated by finding the mean classification accuracy across all 3 classes. The shaded cells in the 3x3 matrix represent correctly classified subjects, and the non-shaded cells represent the 6 different ways to misclassify a subject. The sensitivity of the SWEDDs classification was 59.0%, and the specificity was 85.9%.

Figure 6.1 Example architecture of the PNN/EPNN for the classification of HC, SWEDDs, and PD subjects using the PPMI database. The eight inputs are the MDS-UPDRS Part I (x_1), MDS-UPDRS Part II (x_2), MDS-UPDRS Part III (x_3), MoCA (x_4), SCOPA-AUT (x_5), UPSIT (x_6), the caudate ioflupane (^{123}I) SBR (x_7), and the putamen ioflupane (^{123}I) SBR (x_8). *PD*, Parkinson’s disease; *SW*, SWEDDs; *HC*, healthy controls. As indicated in the pattern layer, there are 170 PD cases in the training set, 56 SWEDDs cases, and 373 healthy control cases.

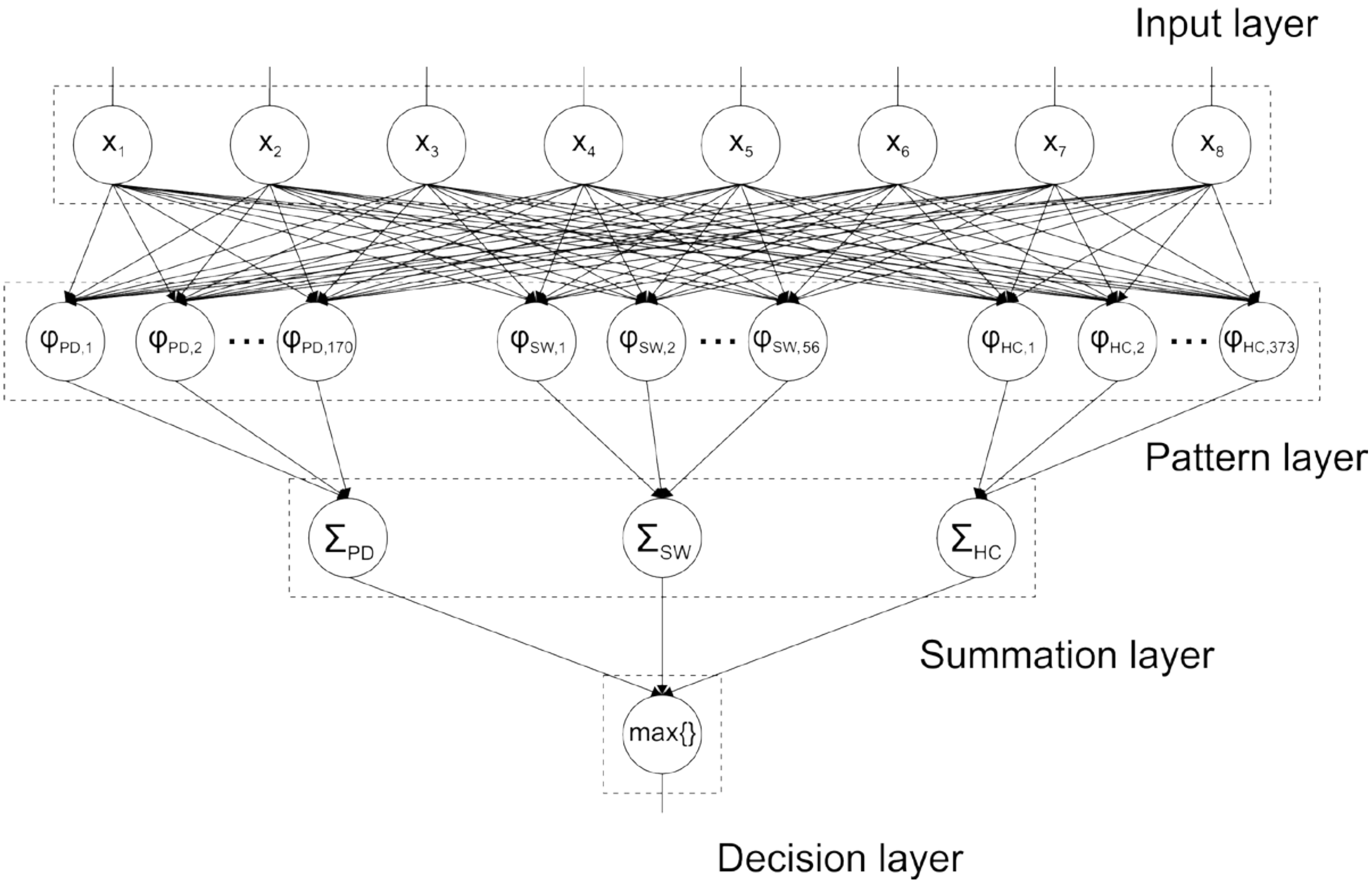

Figure 6.1 Example architecture of the PNN/EPNN for the classification of HC, SWEDDs, and PD subjects.

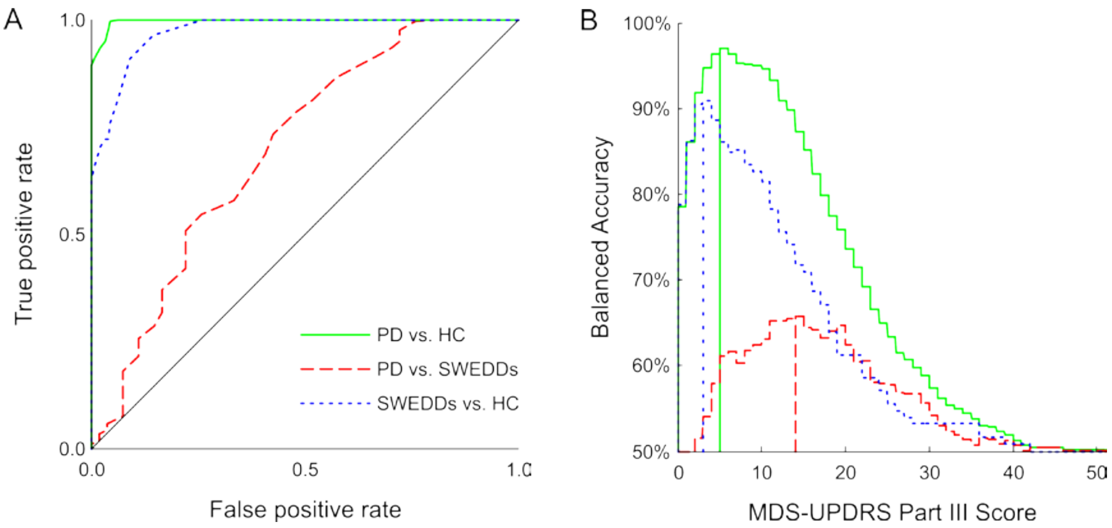

Figure 6.2 *A*: Receiver operating characteristic curve for the MDS-UPDRS Part III. *Solid curve*: PD vs. HC (AUC = 0.997, *N* = 548); *Dashed curve*: PD vs. SWEDDs (AUC = 0.973, *N* = 425); *Dotted curve*: SWEDDs vs. HC (AUC = 0.698, *N* = 229). Diagonal line indicates chance levels of discrimination. *AUC*, area under the curve. *B*: Balanced accuracy of MDS-UPDRS Part III across all classification thresholds. *Solid curve*: PD vs. HC (Max Acc. = 97.0%, threshold = 5.5); *Dashed curve*: PD vs. SWEDDs (Max Acc. = 65.8%, threshold = 13.5); *Dotted curve*: SWEDDs vs. HC (Max Acc. = 91.0%, threshold =3.5).

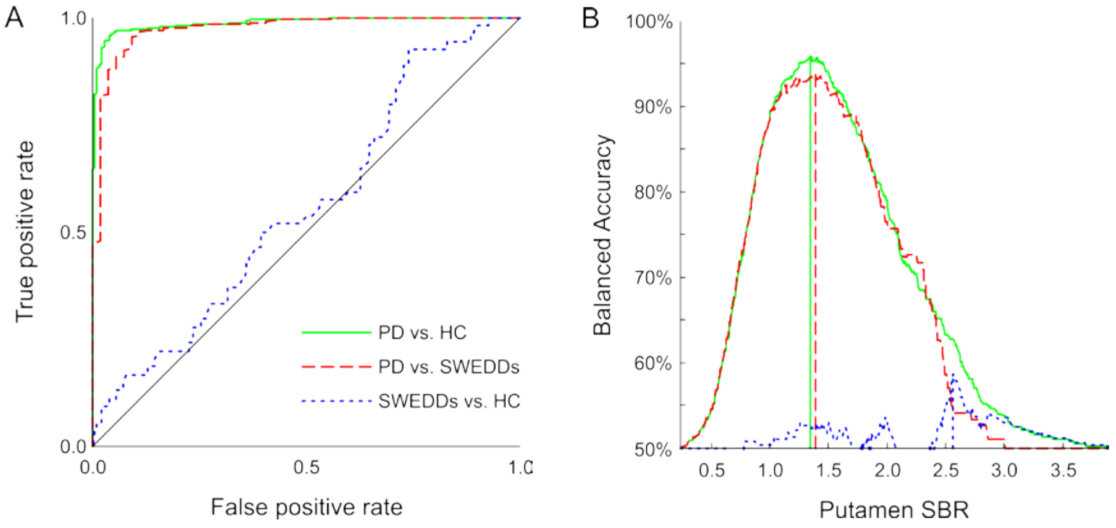

Figure 6.3 *A*: Receiver operating characteristic curve for the putamen SBR. *Solid curve*: PD vs. HC (AUC = 0.987, *N* = 548); *Dashed curve*: PD vs. SWEDDs (AUC = 0.974, *N* = 425); *Dotted curve*: SWEDDs vs. HC (AUC = 0.557, *N* = 229). Diagonal line indicates chance levels of discrimination. *AUC*, area under the curve. *B*: Balanced accuracy of putamen SBR across all classification thresholds. *Solid curve*: PD vs. HC (Max Acc. = 95.8%, threshold = 1.35); *Dashed curve*: PD vs. SWEDDs (Max Acc. = 93.7%, threshold = 1.39); *Dotted curve*: SWEDDs vs. HC (Max Acc. = 58.6%, threshold = 2.57).

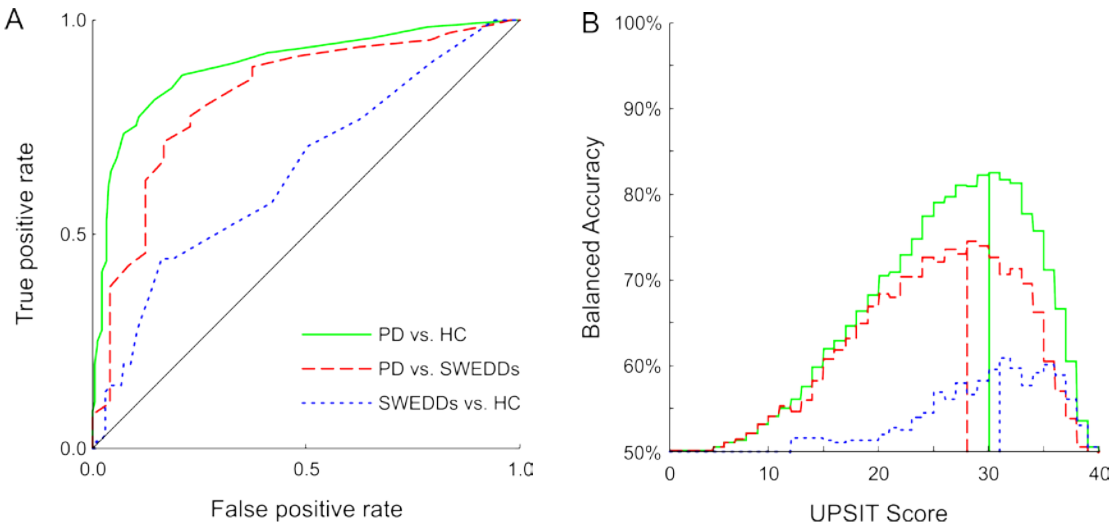

Figure 6.4 *A*: Receiver operating characteristic curve for the UPSIT. *Solid curve*: PD vs. HC (AUC = 0.997, *N* = 548); *Dashed curve*: PD vs. SWEDDs (AUC = 0.973, *N* = 425); *Dotted curve*: SWEDDs vs. HC (AUC = 0.698, *N* = 229). Diagonal line indicates chance levels of discrimination. *AUC*, area under the curve. *B*: Balanced accuracy of UPSIT across all classification thresholds. *Solid curve*: PD vs. HC (Max Acc. = 82.4%, threshold = 30.5); *Dashed curve*: PD vs. SWEDDs (Max Acc. = 74.4%, threshold = 28.5); *Dotted curve*: SWEDDs vs. HC (Max Acc. = 61.0%, threshold = 31.5).

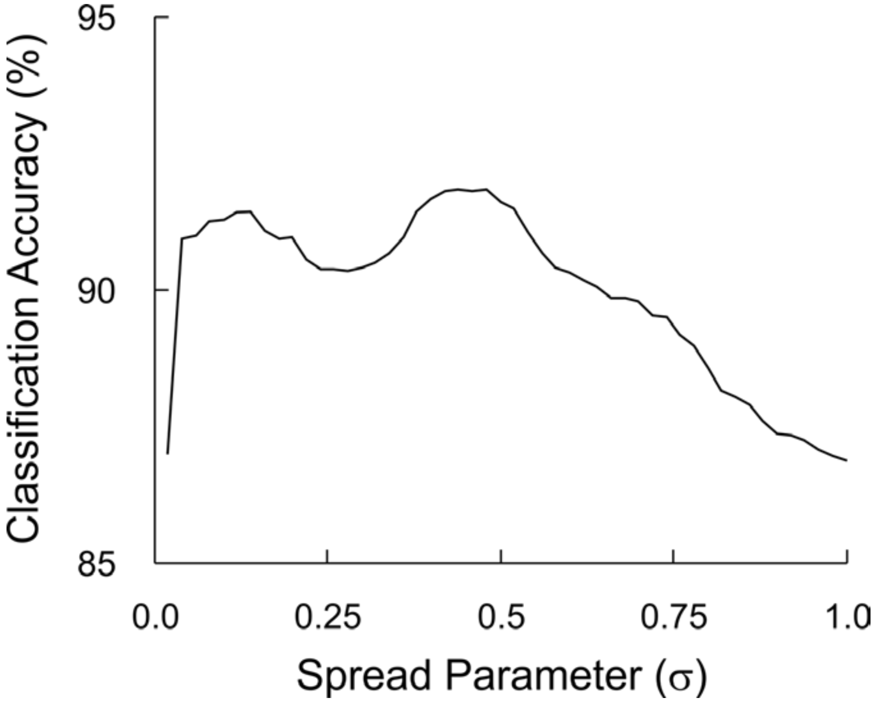

Figure 6.5 Classification accuracy of PNN over a range of spread parameter values. The mean accuracy of 100 iterations is shown. The maximum accuracy was 91.6% for parameter $\sigma = 0.44$.

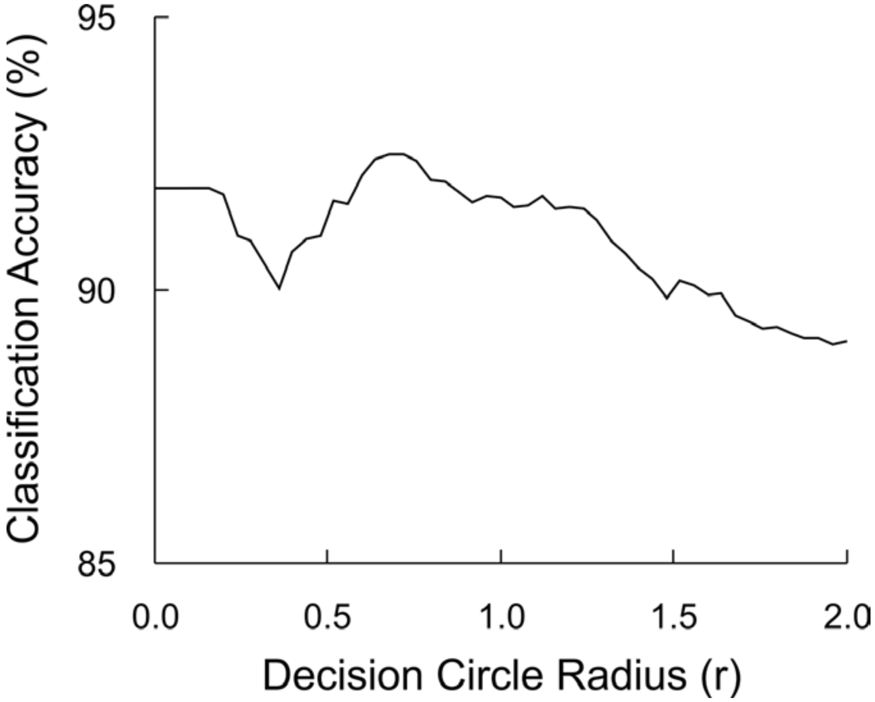

Figure 6.6 Classification accuracy of EPNN over a range of local decision circle radius values. The mean accuracy of 100 iterations is shown. The maximum accuracy was 92.5% for parameters $\sigma = 0.44$ and $r = 0.72$.

Chapter 7: Conclusion

General conclusions

The novel technique for measuring force responses to single-pulse microstimulation presented in Chapter 3 provides investigators a method for detecting small movements or forces evoked by stimulation in the CNS. Just as this technique was used to detect the upper limb forces evoked by stimulation in the PMRF, the physiological motor outputs of other UMNs could be measured. The force pattern resulting from PMRF stimulation supports previous findings indicating a double reciprocal pattern of EMG effects (i.e. facilitation of ipsilateral flexors and contralateral extensors and suppression of ipsilateral extensors and contralateral flexors). In addition, these results characterize the magnitude, direction, and onset latency of upper limb forces as well as the electromechanical delay associated with PMRF microstimulation.

The application of this technique to spontaneous spiking of PMRF neurons presented in Chapter 4 demonstrates sufficient muscle recruitment from single neurons to produce detectable upper limb forces. By demonstrating the validity of this novel technique for investigating motor systems neurophysiology, our findings enable researchers to identify the force outputs of CNS neurons in different motor pathways. This technique could be especially useful in determining the force effects of individual neurons in the motor cortex, which remain controversial (Kakei et al. 1999, 2001). Additionally, the similarity in EMG and force responses to stimulation and spontaneous spiking of nearby PMRF neurons supports the physiological relevance of single-pulse microstimulation and demonstrates its ability to replicate the effects of spontaneous spiking.

The EPNN described in Chapter 6 was shown to be an effective machine learning algorithm for the CAD of PD, with an accuracy of 92.5% for the ternary classification problem. Based on ROC analysis, the putamen SBR was demonstrated to be the single feature most effective at individually differentiating between PD and SWEDDs subjects, whereas the MDS-UPDRS Part III was shown to be the feature most effective at differentiating between SWEDDs subjects and health controls. The fact that UPSIT was the clinical exam that best differentiated PD vs. SWEDDs not only demonstrates its usefulness in informing a cost-effective implementation of ioflupane (^{123}I) neuroimaging, but also suggests that different pathologies cause PD and SWEDDs with distinct effects on olfaction. The EPNN was shown to be more effective at accounting for missing data than the SVM and CT algorithms.

Clinical significance

The motor outputs of the reticulospinal system characterized in Chapters 3 and 4 are similar to the patterns of flexion synergy observed in stroke patients, consistent with an increased role in the control of movement after injury to the corticospinal pathway. This involvement of the PMRF in stroke rehabilitation indicates its potential as a target for pharmacological or electrophysiological therapy after stroke (Jankowska et al. 2005, Jankowska and Edgley 2006). Previous studies have demonstrated that certain pharmacological interventions may preferentially affect reticulospinal pathways (Jankowska and Edgley 2006). For instance, norepinephrine enhances the activation of commissural interneurons by reticulospinal neurons but not by group II afferents (Hammar et al. 2004). The K^+ channel blocker 4-aminopyridine (4-AP) has been shown to increase the effects of pyramidal tract neurons on ipsilateral motor neurons via the reticulospinal pathway (Jankowska et al. 2005). The feasibility of 4-AP as a pharmaceutical therapy is supported by clinical trials for patients with spinal cord injury in which administration of 4-AP was associated with improved motor outcomes (Hansebout et al. 1993, Hayes et al. 1993).

Another pharmacological therapy, the use of a monoclonal anti-Nogo-A antibody treatment has improved motor function in rodent and primate models of stroke and spinal cord injury (Freund et al. 2007, Hamadjida et al. 2012, Lindau et al. 2013). Similarly, down-regulation of the Nogo receptor using adenovirus-mediated RNA interference promoted functional recovery after stroke in rats (Wang et al. 2010). These treatments improved motor outcomes by enhancing neuronal sprouting of upper motor neurons (Freund et al. 2007, Lindau et al. 2013). A thorough understanding of corticospinal, corticoreticular, and reticulospinal outputs is important for appropriate targeting of pharmacological and gene therapies for stroke.

Electrophysiological therapies have a long history of use in treating motor system dysfunction. Deep brain stimulation (DBS) was first used clinically to treat essential tremor (Hassler et al. 1960, Perlmutter and Mink 2006). DBS in the basal ganglia has been shown to effectively manage the motor symptoms of PD and reduce side-effects of

PD medications (Benabid et al. 1991, Perlmutter and Mink 2006). DBS and motor cortex stimulation (MCS) have also been used to successfully control involuntary movements in stroke patients (Katayama et al. 2003). Clinical trials of MCS for stroke patients have shown improved upper limb motor function compared to a standard rehabilitation group (Brown et al. 2006, Levy et al. 2008). Similarly, modulating the activity of PMRF neurons through electrical stimulation, either directly or indirectly, could improve motor rehabilitation after stroke.

CAD of PD can lead to earlier and more accurate diagnoses (Long et al. 2012). Additionally, CAD can facilitate monitoring of PD to better track disease progression (Little et al. 2009, Tsanas et al. 2010). With this information, earlier intervention with disease-modifying agents can slow the decline of motor function in PD patients and improve overall health outcomes (Kansara et al. 2013). By identifying motor and non-motor features predictive of SWEDDs, machine learning algorithms would be able use clinical information to identify patients at risk for SWEDDs who would be candidates for cost-effective functional neuroimaging. By including clinical data from multiple time points as are available in the PPMI database, CAD systems could predict disease progression of PD patients and identify the treatments most likely to be effective on an individual basis. Similarly, using these machine learning techniques for the CAD of other neurological disorders or injuries, such as stroke, could facilitate earlier diagnosis and improved outcomes. Machine learning techniques have previously been used for detecting lesions in MR images of stroke patients (Uchiyama et al. 2012) identifying fMRI markers of motor impairment (Rehme et al. 2014).

Future studies

In the future, we plan to deliver single-pulse microstimulation to neurons in both the motor cortex and PMRF simultaneously while recording EMG and force data. By doing so, we will be able to determine how interactions between cortical neurons and reticulospinal neurons combine to generate force responses in the upper limbs. Next, we will record spontaneous spiking activity from these sites and use these data to analyze gating effects between the cortex and PMRF. With these experiments we will also be able to compare how differently neurons from different motor cortex areas, such as M1, SMA, and PMd, interact with neurons in the PMRF to produce EMG and force effects.

Electrophysiological studies in a primate model of stroke could provide valuable insight into changes in the corticoreticulospinal pathway that occur following ischemic injury to the corticospinal pathway. Injection of the vasoconstrictor endothelin-1 into the motor cortex results in localized ischemic cell death, leading to loss of corticospinal neurons. Changes in descending motor pathways could be identified by comparing the EMG and force responses to microstimulation of motor cortex and PMRF neurons in the stroke model to the responses in the intact primate.

We also plan to complete neuronal tract tracing studies in which triple-labeling will be used to determine the relative proportion of corticoreticular tract fibers that project ipsilaterally or contralaterally from different areas in the motor cortex to the PMRF. This will be accomplished by first injecting two anterograde tracers, biotinylated dextran amine (BDA) and fluorescein isothiocyanate-dextran (FD), one into M1 or PMd of each cerebral hemisphere; then injecting a retrograde tracer, cholera toxin B, into the cervical enlargement. Reticulospinal neurons can then be detected with immunohistochemistry by identifying retrogradely labeled neurons in the brainstem reticular formation. By counting the ratio of anterogradely labeled axons that synapse onto the dendrites of reticulospinal neurons that are labeled with BDA and FD, the proportion of the corticoreticular tract that crosses midline can be determined for each cortical region.

To continue studying the CAD of PD, we plan to examine the effect of genetic biomarkers in improving PD diagnosis. This will be accomplished by utilizing data from the LRRK2 Cohort Consortium dataset, which indicates whether subjects possess any of the common gene variants associated with PD (Paisán-Ruíz 2004). Because this dataset also includes many of the clinical features analyzed in Chapter 6, we will be able to assess the intercenter variability in the accuracy of automated PD diagnosis. The PPMI dataset includes data from multiple time points throughout the course of disease. These data could be used to more accurately predict disease progress for individual patients based on their current symptoms and test results.

References

1. **Adeli H, Hung SL.** Machine Learning - Neural Networks, Genetic Algorithms, and Fuzzy Sets. John Wiley and Sons, New York, 1995.

2. **Aerts MB, Esselink RA, Post B, van de Warrensburg PB, Bloem BR.** Improving the diagnostic accuracy in parkinsonism: a three-pronged approach. *Pract Neurol* 12(2): 77-87, 2012.

3. **Afelt Z.** Functional significance of ventral descending tracts of the spinal cord in the cat. *Acta Neurobiol Exp (Wars)* 34(3): 393-407, 1974.

4. **Ago T, Kitazono T, Ooboshi H, Takada J, Yoshiura T, Mihara F, Ibayashi S, Iida M.** Deterioration of pre-existing hemiparesis brought about by subsequent ipsilateral lacunar infarction. *J Neurol Neurosurg Psychiatry* 74(8): 1152-1153, 2003.

5. **Ahmadlou M, Adeli.** Enhanced probabilistic neural networks with local decision circles: A robust classifier. *Integr Comput Aided Eng* 17: 197-210, 2010.

6. **Alagona G, Delvaux V, Gérard P, De Pasqua V, Pennisi G, Delwaide PJ, Nicoletti F, Maertens de Noordhout A.** Ipsilateral motor responses to focal transcranial magnetic stimulation in healthy subjects and acute-stroke patients. *Stroke* 32(6): 1304-1309, 2001.

7. **Alexander GE, DeLong MR, Strick PL.** Parallel organization of functionally segregated circuits linking basal ganglia and cortex. *Annu Rev Neurosci* 9: 357-381, 1986.

8. **Alibiglou L, MacKinnon CD.** The early release of planned movement by acoustic startle can be delayed by transcranial magnetic stimulation over the motor cortex. *J Physiol* 590(4): 919-936, 2012.

9. **Alstermark B, Pinter MJ, Sasaki S.** Pyramidal effects in dorsal neck motoneurones of the cat. *J Physiol* 363: 287–302, 1985.

10. **Antonini A, Benti R, De Notaris R, Tesei S, Zecchinelli A, Sacilotto G, Meucci N, Canesi M, Mariani C, Pezzoli G, Gerundini P.** 123I-Ioflupane/SPECT binding to striatal dopamine transporter (DAT) uptake in patients with Parkinson's disease, multiple system atrophy, and progressive supranuclear palsy. *Neurol Sci* 24(3): 149-150, 2003.

11. **Armañanzas R, Bielza C, Chaudhuri KR, Martinez-Martin P, Larrañaga P**. Unveiling relevant non-motor Parkinson's disease severity symptoms using a machine learning approach. *Artif Intell Med* 58(3): 195-202, 2013.

12. **Ashe J.** Force and the motor cortex. *Behav Brain Res* 87: 255-269, 1997.

13. **Babu GS, Suresh S, Mahanand BS.** A novel PBL-McRBFN-RFE approach for identification of critical brain regions responsible for Parkinson's disease. *Expert Syst Appl* 41(2): 478-488, 2014.

14. **Baker SN, Lemon RN.** Computer simulation of post-spike facilitation in spike-triggered averages of rectified EMG. *J Neurophysiol* 80: 1391-1406, 1998.

15. **Baker SN, Zaaimi B, Fisher KM, Edgley SA, Soteropoulos DS.** Pathways mediating functional recovery. *Prog Brain Res* 218: 389-412, 2015.

16. **Bannatyne BA, Edgley SA, Hammar I, Jankowska E, Maxwell DJ.** Networks of inhibitory and excitatory commissural interneurons mediating crossed reticulospinal actions. *Eur J Neurosci* 18: 2273-2284, 2003.

17. **Beer RF, Dewald JP, Rymer WZ.** Deficits in the coordination of multijoint arm movements in patients with hemiparesis: evidence for disturbed control of limb dynamics. *Exp Brain Res* 131(3): 305-319, 2000.

18. **Bem T, Górska T, Majczyński H, Zmysłowski W.** Different patterns of fore-hindlimb coordination during overground locomotion in cats with ventral and lateral spinal lesions. *Exp Brain Res* 104(1): 70-80, 1995.

19. **Benabid AL, Pollak P, Gervason C, Hoffmann D, Gervason C, Hommel M, Perret JE, de Rougemont J, Gao DM**. Long-term suppression of tremor by chronic stimulation of the ventral intermediate thalamic nucleus. *Lancet* 337: 403-406, 1991.

20. **Bennett RL, Blanks RG, Moss SM.** Does the accuracy of single reading with CAD (computer-aided detection) compare with that of double reading?: A review of the literature. *Clin Radiol* 61(12): 1023-1028, 2006.

21. **Betts B, Smith JL, Edgerton VR, Collatos TC.** Telemetered EMG of fast and slow muscles in cats. *Brain Res* 117: 529-533, 1976.

22. **Boelmans K, Bodammer NC, Bogdana S, Kaufman J, Ebersbach G, Heinze H, Niehaus L**. Diffusion tensor imaging of the corpus callosum differentiates corticobasal syndrome from Parkinson’s disease. *Parkinsonism & Relat Disord* 16(8): 498-502, 2010.

23. **Bolton PS, Goto T, Schor RH, Wilson VJ, Yamagata Y, Yates BJ.** Response of pontomedullary reticulospinal neurons to vestibular stimuli in vertical planes. Role in vertical vestibulospinal reflexes of the decerebrate cat. *J Neurophysiol* 67(3): 639-647, 1992.

24. **Bonita R, Beaglehole R.** Recovery of motor function after stroke. *Stroke* 19(12): 1497-1500, 1988.

25. **Borlongan CV, Burns J, Tajiri N, Stahl CE, Weinbren NL, Shojo H, … van Loveren HR.** Epidemiological Survey-Based Formulae to Approximate Incidence and Prevalence of Neurological Disorders in the United States: a Meta-Analysis. *PLoS ONE* 8(10): e78490. doi:10.1371/journal.pone.0078490, 2013.

26. **Brink EE, Suzuki I, Timerick SJ, Wilson VJ.** Tonic neck reflex of the decerebrate cat: a role for propriospinal neurons. *J Neurophysiol* 54: 978-987, 1985.

27. **Brown JA, Lutsep H, Weinand M, Cramer S.** Motor cortex stimulation for the enhancement of recovery from stroke: a prospective, multicenter safety study. *J Neurosurg* 58: 464-473, 2006.

28. **Brown P, Rothwell JC, Thompson PD, Britton TC, Day BL, Marsden CD.** New observations on the normal auditory startle reflex in man. *Brain* 114(4): 1891–1902, 1991.

29. **Brustein E, Rossignol S.** Recovery of locomotion after ventral and ventrolateral spinal lesions in the cat. I. Deficits and adaptive mechanisms. *J Neurophysiol* 80(3): 1245-1267, 1998.

30. **Buford JA, Davidson AG.** Movement-related and preparatory activity in the reticulospinal system of the monkey. *Exp Brain Res* 159: 284-300, 2004.

31. **Buford JA, Montgomery L.** Small force transients in the upper limbs recorded in association with stimulus triggered averaging in the reticulospinal system of the monkey. *Soc Neurosci Abstr* 591.02, 2011.

32. **Bütefisch CM.** Plasticity in the human cerebral cortex: lessons from the normal brain and from stroke. Neuroscientist 10(2): 163-73, 2004.

33. **Canedo A, Lamas JA.** Pyramidal and corticospinal synaptic effects over reticulospinal neurones in the cat. *J Physiol* 463: 475-489, 1993.

34. **Caplan LR, Goodwin JA.** Lateral tegmental brainstem hemorrhages. *Neurology* 32(3): 252-260, 1982.

35. **Chae J, Yang G, Park BK, Labatia I.** Delay in initiation and termination of muscle contraction, motor impairment, and physical disability in upper limb hemiparesis. *Muscle Nerve* 25(4): 568-575, 2002.

36. **Cheney PD, Fetz EE.** Comparable patterns of muscle facilitation evoked by individual corticomotoneuronal (CM) cells and by single intracortical microstimuli in primates: evidence for functional groups of CM cells. *J Neurophysiol* 53: 786-804, 1985.

37. **Cheney PD, Fetz EE, Mewes K.** Neural mechanisms underlying corticospinal and rubrospinal control of limb movements. *Prog Brain Res* 87: 213–252, 1991.

38. **Connolly BS, Lang AE.** Pharmacological treatment of Parkinson disease: a review. *JAMA* 311(16): 1670-1683, 2014.

39. **Corio M, Palisses R, Viala D.** Origin of the central entrainment of respiration by locomotion facilitated by MK 801 in the decerebrate rabbit. *Exp Brain Res* 95(1): 84-90, 1993.

40. **Cortes C, Vapnik V.** Support-vector networks. *Mach Learn* 20(3): 273, 1995.

41. **Cover TM, Hart PE.** Nearest neighbor pattern classification. *IEEE T Inform Theory* 13(1): 21–27, 1967.

42. **Cowie RJ, Robinson DL.** Subcortical contributions to head movements in macaques. I. Contrasting effects of electrical stimulation of a medial pontomedullary region and the superior colliculus. *J Neurophysiol* 72: 2648-2664, 1994.

43. **Cowie RJ, Smith MK, Robinson DL.** Subcortical contributions to head movements in macaques. II. Connections of a medial pontomedullary head-movement region. *J Neurophysiol* 72(6): 2665-2682, 1994.

44. **Daliri M.** Chi-square distance kernel of the gaits for the diagnosis of Parkinson's disease. *Biomedical Signal Processing and Control* 8: 66-70, 2013.

45. **Daly JJ, Fang Y, Perepezko EM, Siemionow V, Yue GH.** Prolonged cognitive planning time, elevated cognitive effort, and relationship to coordination and motor control following stroke. *IEEE Trans Neural Syst Rehabil Eng*14(2): 168-171, 2006.

46. **Daly JJ, Sng K, Roenigk K, Fredrickson E, Dohring M.** Intra-limb coordination deficit in stroke survivors and response to treatment. *Gait Posture* 25(3): 412-418, 2007.

47. **Darabid H, Perez-Gonzalez AP, Robitaille R.** Neuromuscular synaptogenesis: coordinating partners with multiple functions. *Nat Rev Neurosci* 15(11): 703-718, 2014.

48. **Davidson AG, Buford JA.** Motor outputs from the primate reticular formation to shoulder muscles as revealed by stimulus triggered averaging. *J Neurophysiol* 92: 83-95, 2004.

49. **Davidson AG, Buford JA.** Bilateral actions of the reticulospinal tract on arm and shoulder muscles in the monkey: stimulus triggered averaging. *Exp Brain Res* 173: 25-39, 2006.

50. **Davidson AG, Schieber MH, Buford JA.** Bilateral spike-triggered average effects in arm and shoulder muscles from monkey pontomedullary reticular formation. *J Neurosci* 27: 8053-8058, 2007.

51. **Davie CA.** A review of Parkinson's disease. *Br Med Bull* 86(1): 109-127, 2008.

52. **de Dombal FT, Leaper DJ, Staniland JR, McCann AP, Horrocks JC.** Computer-aided diagnosis of acute abdominal pain. *Br Med J* 2(5804): 9-13, 1972.

53. **de Freitas GR, Devuyst G, van Melle G, Bogousslavsky J.** Motor strokes sparing the leg: different lesions and causes. *Arch Neurol* 57(4): 513-8, 2000.

54. **de Lau LM, Breteler MM.** Epidemiology of Parkinson's disease. *Lancet Neurol* 5(6): 525-535, 2006.

55. **de Lau LM, Koudstaal PJ, Hofman A, Breteler MM.** Subjective complaints precede Parkinson disease: the rotterdam study. *Arch Neurol* 63(3): 362-365, 2006.

56. **De Rosa A, Carducci C, Carducci C, Peluso S, Lieto M, Mazzella A, Saccà F, Brescia Morra V, Pappatà S, Leuzzi V, De Michele G.** Screening for dopa-responsive dystonia in patients with scans without evidence of dopaminergic deficiency (SWEDD). *J Neurol* 261(11): 2204-2208, 2014.

57. **DeKosky ST, Marek K.** Looking backward to move forward: early detection of neurodegenerative disorders. *Science* 302(5646): 830-834, 2003.

58. **Dewald JP, Beer RF.** Abnormal joint torque patterns in the paretic upper limb of subjects with hemiparesis. *Muscle Nerve* 24(2): 273-283, 2001.

59. **Dewald JP, Pope PS, Given JD, Buchanan TS, Rymer WZ.** Abnormal muscle coactiviation patterns during isometric torque generation at the elbow and shoulder in hemiparetic subjects. *Brain* 118: 495-510, 1995.

60. **Dickson DW, Fujishiro H, Orr C, DelleDonne A, Josephs KA, Frigerio R, Burnett M, Parisi JE, Klos KJ, Ahlskog JE.** Neuropathology of non-motor features of Parkinson disease. *Parkinsonism Relat Disord* 15: S1-5, 2009.

61. **Doi K.** Computer-aided diagnosis in medical imaging: historical review, current status and future potential. *Comput Med Imaging Graph* 31(4-5): 198-211, 2007.

62. **Drew T, Dubuc R, Rossignol S.** Discharge patterns of reticulospinal and other reticular neurons in chronic, unrestrained cats walking on a treadmill. *J Neurophysiol* 55(2): 375-401, 1986.

63. **Drew T, Prentice S, Schepens B.** Cortical and brainstem control of locomotion. *Prog Brain Res* 143: 251-261, 2004.

64. **Drew T, Rossignol S.** Phase-dependent responses evoked in limb muscles by stimulation of medullary reticular formation during locomotion in thalamic cats. *J Neurophysiol* 52: 653-675, 1984.

65. **Drew T, Rossignol S.** Functional organization within the medullary reticular formation of intact unanesthetized cat. I. Movements evoked by microstimulation. *J Neurophysiol* 64: 767-781, 1990a.

66. **Drew T, Rossignol S.** Functional organization within the medullary reticular formation of intact unanesthetized cat. II. Electromyographic activity evoked by microstimulation. *J Neurophysiol* 64: 782-795, 1990b.

67. **Eccles JC, Nicoll RA, Schwarz WF, Táboriková H, Willey TJ**. Reticulospinal neurons with and without monosynaptic inputs from cerebellar nuclei. *J Neurophysiol* 38(3): 513-530, 1975.

68. **Edgley SA, Jankowska E, Hammar I.** Ipsilateral actions of feline corticospinal tract neurons on limb motoneurons. *J Neurosci* 24(36): 7804-7813, 2004.

69. **Eidelberg E, Story JL, Walden JG, Meyer BL.** Anatomical correlates of return of locomotor function after partial spinal cord lesions in cats. *Exp Brain Res* 42: 81-88, 1981.

70. **Eidelberg D, Surmeier DJ.** Brain networks in Huntington disease. *J Clin Invest* 121(2): 484-492, 2011.

71. **Elbert T, Rockstroh B.** Reorganization of human cerebral cortex: the range of changes following use and injury. Neuroscientist. 10(2): 129-141, 2004.

72. **Ellis MD, Acosta AM, Yao J, Dewald JP.** Position-dependent torque coupling and associated muscle activation in the hemiparetic upper extremity. *Exp Brain Res* 176(4): 594-602, 2007.

73. **Ellis MD, Drogos J, Carmona C, Keller T, Dewald JP.** Neck rotation modulates flexion synergy torques, indicating an ipsilateral reticulospinal source for impairment in stroke. *J Neurophysiol* 108: 3096-3104, 2012.

74. **Elmore JG, Armstrong K, Lehman CD, Fletcher SW.** Screening for breast cancer. *JAMA* 293(10): 1245-1256, 2005.

75. **Evarts EV.** Relation of pyramidal tract activity to force exerted during voluntary movement. *J Neurophysiol* 31: 14-27, 1968.

76. **Fang Y, Daly JJ, Sun J, Hvorat K, Fredrickson E, Pundik S, Sahgal V, Yue GH.** Functional Corticomuscular Connection During Reaching Is Weakened Following Stroke. *Clin Neurophysiol* 120(5): 994–1002, 2009.

77. **Fisher CM.** Concerning the mechanism of recovery in stroke hemiplegia. *Can J Neurol Sci* 19: 57–63, 1992.

78. **Fisher KM, Zaaimi B, Baker SN.** Reticular formation responses to magnetic brain stimulation of primary motor cortex. *J Physiol* 590(16): 4045-4060, 2012.

79. **Freer TW, Ulissey MJ.** Screening mammography with computer-aided detection: prospective study of 12,860 patients in a community breast center. *Radiology* 220(3): 781-786, 2001.

80. **Freund P, Wannier T, Schmidlin E, Bloch J, Mir A, Schwab ME, Rouiller EM.** Anti-Nogo-A antibody treatment enhances sprouting of corticospinal axons rostral to a unilateral cervical spinal cord lesion in adult macaque monkey. *J Comp Neurol* 502(4): 644-659, 2007.

81. **Fuchs AF, Luschei ES.** Firing patterns of abducens neurons of alert monkeys in relationship to horizontal eye movement. *J Neurophysiol* 33: 382-392, 1970.

82. **Gahéry Y, Ioffe ME, Massion J, Polit A.** The postural support of movement in cat and dog. *Act Neurobiol Exp* 40: 741-756, 1980.

83. **Gahéry Y, Nieoullon A.** Postural and kinetic coordination following cortical stimuli which induce flexion movements in the cat's limbs. *Brain Res* 149(1): 25-37, 1978.

84. **Gallagher DA, Lees AJ, Schrag A.** What are the most important nonmotor symptoms in patients with Parkinson's disease and are we missing them? *Mov Disord* 25(15): 2493-2500, 2010.

85. **Garcia-Rill E.** The basal ganglia and the locomotor regions. *Brain Res* 396(1): 47-63, 1986.

86. **Garcia-Rill E, Kinjo N, Atsuta Y, Ishikawa Y, Webber M, Skinner RD.** Posterior midbrain-induced locomotion. *Brain Res Bull* 24(3): 499-508, 1990.

87. **Garcia-Rill E, Skinner RD, Fitzgerald JA.** Chemical activation of the mesencephalic locomotor region. *Brain Res* 330(1): 43-54, 1985.

88. **Garcia-Rill E, Skinner RD, Jackson MB, Smith MM.** Connections of the mesencephalic locomotor region (MLR) I. Substantia nigra afferents. *Brain Res Bull* 10(1): 57-62, 1983.

89. **Garraux G, Phillips C, Schrouff J, Kreisler A, Lemaire C, Degueldre C, Delcour C, ... Salmon E.** Multiclass classification of FDG PET scans for the distinction between Parkinson's disease and atypical parkinsonian syndromes. *Neuroimage Clin* 2: 883-893, 2013.

90. **Gelb DJ, Oliver E, Gilman S.** Diagnostic criteria for Parkinson disease. *Arch Neurol* 56: 33-39, 1999.

91. **Georgopolous AP, Ashe J, Smyrnis N, Taira M.** The motor cortex and the coding of force. *Science* 256: 1692-1695, 1992.

92. **Ghosh-Dastidar S, Adeli H, and Dadmehr N.** Voxel-based Morphometry in Alzheimer’s Patients. *J Alzheimers Dis* 10(4): 445-447, 2006.

93. **Glickstein M, Doron K.** Cerebellum: connections and functions. *Cerebellum* 7(4): 589-594, 2008.

94. **Goetz CG, Tilley BC, Shaftman SR, Stebbins GT, Fahn S, Martinez-Martin P, Poewe W, … LaPelle N; Movement Disorder Society UPDRS Revision Task Force.** Movement Disorder Society-sponsored revision of the Unified Parkinson's Disease Rating Scale (MDS-UPDRS): scale presentation and clinimetric testing results. *Mov Disord* 23(15): 2129-2170, 2008.

95. **Goldstein DS, Holmes C, Bentho O, Sato T, Moak J, Sharabi Y, Imrich R, … Eldadah BA.** Biomarkers detect central dopamine deficiency and distinguish Parkinson disease from multiple system atrophy. *Parksinonism Relat Disord* 14(8): 600-607, 2008.

96. **Górska T, Bem T, Majczyński H.** Locomotion in cats with ventral spinal lesions: support patterns and duration of support phases during unrestrained walking. *Acta Neurobiol Exp (Wars)* 50(4-5): 191-199, 1990.

97. **Górska T, Bem T, Majczyński H, Zmysłowski W.** Unrestrained walking in cats with partial spinal lesions. *Brain Res Bull* 32(3): 241-249, 1993.

98. **Gray H.** *Anatomy of the Human Body*. Philadelphia: Lea & Febiger, 1918.

99. **Grillner S.** The motor infrastructure: from ion channels to neuronal networks. *Nat Rev Neurosci* 4(7): 573-586, 2003.

100. **Grillner S, Lund S.** A descending pathway with monosynaptic action on flexor motoneurones. *Experimentia* 22: 390-390, 1966.

101. **Grillner S, Lund S.** The origin of a descending pathway with monosynaptic action on flexor motoneurones. *Acta Physiol Scand* 74: 274-284, 1968.

102. **Groenewegen HJ.** The basal ganglia and motor control. *Neural Plast* 10(1-2): 107-120, 2003.

103. **Grosset J-F, Piscione J, Lambertz D, Perot C.** Paired changes in electromechanical delay and musculo-tendinous stiffness after endurance or plyometric training. *Eur J Appl Physiol* 105: 131-139, 2008.

104. **Hallett M.** Plasticity of the human motor cortex and recovery from stroke. *Brain Res Rev* 36(2-3):169-174, 2001.

105. **Hamadjida A, Wyss AF, Mir A, Schwab ME, Belhaj-Saif A, Rouiller EM.** Influence of anti-Nogo-A antibody treatment on the reorganization of callosal connectivity of the premotor cortical areas following unilateral lesion of primary motor cortex (M1) in adult macaque monkeys. *Exp Brain Res* 223(3): 321-340, 2012.

106. **Hanna JP, Frank JI.** Automatic stepping in the pontomedullary stage of central herniation. *Neurology* 45(5): 985-986, 1995.

107. **Hansebout RR, Blight AR, Fawcett S, Reddy K.** 4-Aminopyridine in chronic spinal cord injury: a controlled, double-blind, crossover study in eight patients. *J Neurotrauma* 10(1): 1–18, 1993.

108. **Hassler R, Riechart T, Munginer F, Umbach W, Ganglberger JA.** Physiological observations in stereotaxic operations in extrapyramidal motor disturbances. *Brain* 83: 337-350, 1960.

109. **Hauser RA, Auinger P; Parkinson Study Group.** Determination of minimal clinically important change in early and advanced Parkinson's disease. *Mov Disord* 26(5): 813-818, 2011.

110. **Hayes KC, Blight AR, Potter PJ, Allatt RD, Hsieh JT, Wolfe DL, Lam S, Hamilton JT.** Preclinical trial of 4-aminopyridine in patients with chronic spinal cord injury. *Paraplegia* 31(4): 216–224, 1993.

111. **He XW, Wu CP.** Connections between pericruciate cortex and the medullary reticulospinal neurons in cat: an electrophysiological study. *Exp Brain Res* 61(1): 109-116, 1985.

112. **Herbert WJ, Davidson AG, Buford JA.** Measuring the motor output of the pontomedullary reticular formation in the monkey: do stimulus-triggered averaging and stimulus trains produce comparable results in the upper limbs? *Exp Brain Res* 203: 271-283, 2010.

113. **Hirschauer TJ, Buford JA.** Bilateral force transients in the upper limbs evoked by single-pulse microstimulation in the ponto-medullary reticular formation. *J Neurophysiol* 113(7): 2592-2604, 2015.

114. **Hoffman DS, Strick PL.** Step-tracking movements of the wrist. IV. Muscle activity associated with movements in different directions. *J Neurophysiol* 81: 319-333, 1999.

115. **Houssami N, Given-Wilson R, Ciatto S.** Early detection of breast cancer: overview of the evidence on computer-aided detection in mammography screening. *J Med Imaging Radiat Oncol* 53(2): 171-176, 2009.

116. **Hughes AJ, Ben-Shlomo Y, Daniel SE, Lees AJ.** What features improve the accuracy of clinical diagnosis in Parkinson's disease: a clinicopathologic study. *Neurology* 42: 1142-1146, 1992.

117. **Hughes AJ, Daniel SE, Kilford L, Lees AJ.** Accuracy of clinical diagnosis of idiopathic Parkinson's disease: a clinico-pathological study of 100 cases. *J Neurol Neurosurg Psychiatry* 55: 181–184, 1992.

118. **Hughes AJ, Daniel SE, Lees AJ.** Improved accuracy of clinical diagnosis of Lewy body Parkinson’s disease. *Neurology* 57: 1497-1499, 2001.

119. **Illan IA, Gorrz JM, Ramirez J, Segovia F, Jimenez-Hoyuela JM, Ortega Lozano SJ.** Automatic assistance to Parkinson's disease diagnosis in DaTSCAN SPECT imaging. *Med Phys* 39(10): 5971-5980, 2012.

120. **Jang SH.** Motor recovery mechanisms in patients with middle cerebral artery infarct: a mini-review. *Eur Neurol* 68(4): 234-239, 2012.

121. **Jankovic J.** Parkinson's disease: clinical features and diagnosis. *J Neurol Neurosurg Psychiatry* 79(4): 368-376, 2008.

122. **Jankowska E, Edgley SA.** How can corticospinal tract neurons contribute to ipsilateral movements? A question with implications for recovery of motor functions. *Neuroscientist* 12: 67-79, 2006.

123. **Jankowska E, Hammar I, Slawinska U, Maleszak K, Edgley SA.** Neuronal basis of crossed actions from the reticular formation on feline hindlimb motoneurons. *J Neurosci* 23: 1867-1878, 2003.

124. **Johansen-Berg H, Rushworth MF, Bogdanovic MD, Kischka U, Wimalaratna S, Matthews PM.** The role of ipsilateral premotor cortex in hand movement after stroke. *Proc Natl Acad Sci USA* 99(22): 14518-14523, 2002.

125. **Jørgensen HS, Nakayama H, Raaschou HO, Vive-Larsen J, Støier M, Olsen TS.** Outcome and time course of recovery in stroke. Part II: Time course of recovery. The Copenhagen Stroke Study. *Arch Phys Med Rehabil* 76(5): 406-412, 1995.

126. **Kably B, Drew T.** Corticoreticular pathways in the cat. I. Projection patterns and collaterization. *J Neurophysiol* 80(1): 389-405, 1998.

127. **Kakei S, Hoffman DS, Strick PL.** Muscle and movement representations in the primary motor cortex. *Science* 285: 2136-2139, 1999.

128. **Kakei S, Hoffman DS, Strick PL.** Direction of action is represented in the ventral premotor cortex. *Nature Neurosci* 4: 1020-1025, 2001.

129. **Kansara S, Trivedi A, Chen S, Jankovic J, Le W.** Early diagnosis and therapy of Parkinson's disease: can disease progression be curbed? *J Neural Transm* 120(1): 197-210, 2013.

130. **Katayama Y, Yamamoto T, Kobayashi K, Oshima H, Fukaya C.** Deep brain and motor cortex stimulation for post-stroke movement disorders and post-stroke pain. *Acta Neurochir Suppl* 87: 121-123, 2003.

131. **Keizer K, Kuypers HG.** Distribution of corticospinal neurons with collaterals to lower brain stem reticular formation in cat. *Exp Brain Res* 54(1): 107-120, 1984.

132. **Keizer K, Kuypers HG.** Distribution of corticospinal neurons with collaterals to the lower brain stem reticular formation in monkey (Macaca fascicularis). *Exp Brain Res* 74(2): 311-318, 1989.

133. **Kilbreath SL, Gorman RB, Raymond J, Gandevia SC.** Distribution of the forces produced by motor unit activity in the human flexor digitorum profundus. *J Physiol* 543: 289-296, 2002.

134. **Klöppel S, Stonnington CM, Chu C, Draganski B, Scahill RI, Rohrer JD, Fox NC, Jack CR Jr, Ashburner J, Frackowiak RS.** Automatic classification of MR scans in Alzheimer's disease. *Brain* 131(3): 681-689, 2008.

135. **Krakauer JW.** Arm function after stroke: from physiology to recovery. *Semin Neurol* 25(4): 384-395, 2005.

136. **Krakauer JW, Radoeva PD, Zarahn E, Wydra J, Lazar RM, Hirsch J, Marshall RS.** Hypoperfusion without stroke alters motor activation in the opposite hemisphere. *Ann Neurol* 56(6): 796-802, 2004.

137. **Kuypers HG.** Anatomical analysis of cortico-bulbar connexions to the pons and the lower brain stem in the cat. *J Anat* 92: 198-218, 1958.

138. **Kuypers HG.** Anatomy of descending pathways. In: *Handbook of Physiology. The Nervous System. Motor Control*. Bethesda, MD: Am. Physiol. Soc., 1981, sect. 1, vol. II, pt 1., p. 597-666.

139. **Kuypers HG.** The descending pathways to the spinal cord, their anatomy and function. *Prog Brain Res* 11: 178-202, 1964.

140. **Langhorne P, Coupar F, Pollock A.** Motor recovery after stroke: a systematic review. *Lancet Neurol* 8(8): 741-754, 2009.

141. **Lawrence DG, Kuypers HG.** The functional organization of the motor systems in the monkey. I. The effects of bilateral pyramidal lesions. *Brain* 91: 1–14, 1968.

142. **Lawrence ES, Coshall C, Dundas R, Stewart J, Rudd AG, Howard R, Wolfe CD.** Estimates of the prevalence of acute stroke impairments and disability in a multiethnic population. *Stroke.* 32(6): 1279-1284, 2001.

143. **Lee MJ, Kim SL, Lyoo CH, Lee MS.** Kinematic analysis in patients with Parkinson's disease and SWEDD. *J Parkinsons Dis* 4(3): 421-430, 2014.

144. **Lemon RN.** The G. L. Brown Prize Lecture. Cortical control of the primate hand. *Exp Physiol* 78(3): 263-301, 1993.

145. **Lemon RN.** Descending pathways in motor control. *Ann Rev Neurosci* 31: 195-218, 2008.

146. **Levin MF.** Interjoint coordination during pointing movements is disrupted in spastic hemiparesis. *Brain* 119(1): 281-293, 1996.

147. **Levy R, Ruland S, Weinand M, Lowry D, Dafer R, Bakay R.** Cortical stimulation for the rehabilitation of patients with hemiparetic stroke: a multicenter feasibility study of safety and efficacy. *J Neurosurg* 108(4): 707-714, 2008.

148. **Li S, Chang SH, Francisco GE, Verduzco-Gutierrez M.** Acoustic startle reflex in patients with chronic stroke at different stages of motor recovery: a pilot study. *Top Stroke Rehabil* 21(4): 358-370, 2014.

149. **Lindau NT, Bänninger BJ, Gullo M, Good NA, Bachmann LC, Starkey ML, Schwab ME.** Rewiring of the corticospinal tract in the adult rat after unilateral stroke and anti-Nogo-A therapy. *Brain* 137(3): 739-756, 2014.

150. **Lippold, OCJ**. The relation between integrated action potentials in a human muscle and its isometric tension. *J Physiol* 117: 492-499, 1952.

151. **Little MA, McSharry PE, Hunter EJ, Spielman J, Ramig LO.** Suitability of dysphonia measurements for telemonitoring of Parkinson's disease. *IEEE Trans Biomed Eng* 56(4): 1015, 2009.

152. **Liu CN, Chambers WW.** An experimental study of the cortico-spinal system in the monkey (Macaca mulatta). *J Comp Neurol* 123: 257-284, 1964.

153. **Long D, Wang J, Xuan M, Gu Q, Xu X, Kong D, Zhang M**. Automatic classification of early Parkinson's disease with multi-modal MR imaging. *PLoS One* 7(11): e47714, 2012.

154. **Luccarini P, Gahéry Y, Pompeiano O.** Cholinoceptive pontine reticular structures modify the postural adjustments during the limb movements induced by cortical stimulation. *Arch Ital Biol* 128(1): 19-45, 1990.

155. **Magni F, Willis WD.** Cortical control of brain stem reticular neurons. *Arch Ital Biol* 102: 418-433, 1964.

156. **Marek K, Jennings D, Lasch S, Siderowf A, Tanner C, Simuni T, Coffey C, … Taylor P.** The Parkinson Progression Marker Initiative (PPMI). *Prog Neurobiol* 95(4): 629-635, 2011.

157. **Mark VW, Taub E.** Constraint-induced movement therapy for chronic stroke hemiparesis and other disabilities. *Restor Neurol Neurosci* 22(3-5): 317-336, 2004.

158. **Martin JH.** The corticospinal system: from development to motor control. *Neuroscientist* 11(2): 161-173, 2005.

159. **Martin RF, Bowden DM.** A stereotaxic template atlas of the macaque brain for digital imaging and quantitative neuroanatomy. *Neuroimage* 4: 119-150, 1996.

160. **Martinez-Murcia FJ, Gorriz JM, Ramirez J, Illan IA, the Parkinson's Progression Markers Initiative.** Automated Detection of Parkinsonism Using Significance Measures and Component Analysis in DatSCAN imaging. *Neurocomputing* 126: 58-70, 2014.

161. **Masdeu JC, Alampur U, Cavaliere R, Tavoulareas G.** Astasia and gait failure with damage of the pontomesencephalic locomotor region. *Ann Neurol* 35(5): 619-621, 1994.

162. **Matsuyama K, Drew T.** Organization of the projections from the pericruciate cortex to the pontomedullary brainstem of the cat: a study using the anterograde tracer Phaseolus vulgaris-leucoagglutinin. *J Comp Neurol* 389(4): 617-641, 1997.

163. **Matsuyama K, Drew T.** Vestibulospinal and reticulospinal neuronal activity during locomotion in the intact cat. I. Walking on a level surface. *J Neurophysiol* 84(5): 2237-2256, 2000.

164. **Matsuyama K, Mori F, Nakajima K, Drew T, Aoki M, Mori S.** Locomotor role of the corticoreticular-reticulospinal-spinal interneuronal system. *Prog Brain Res* 143: 239-249, 2004.

165. **Matsuyama K, Takakusaki K, Nakajima K, Mori S.** Multi-segmental innervation of single pontine reticulospinal axons in the cervico-thoracic region of the cat: anterograde PHA-L tracing study. *J Comp Neurol* 377: 234-250, 1997.

166. **McClellan AD, Grillner S.** Activation of 'fictive swimming' by electrical microstimulation of brainstem locomotor regions in an in vitro preparation of the lamprey central nervous system. *Brain Res* 300(2): 357-361, 1984.

167. **McKiernan BJ, Marcario JK, Karrer JH, Cheney PD.** Corticomotoneuronal postspike effects in shoulder, elbow, wrist, digit, and intrinsic hand muscles during a reach and prehension task. *J Neurophysiol* 80: 1961-1980, 1998.

168. **Ménard A, Grillner S.** Diencephalic locomotor region in the lamprey--afferents and efferent control. *J Neurophysiol* 100(3): 1343-1353, 2008.

169. **Merello M, Nouzeilles MI, Arce GP, Leiguarda R.** Accuracy of acute levodopa challenge for clinical prediction of sustained long-term levodopa response as a major criterion for idiopathic Parkinson's disease diagnosis. *Mov Disord* 17(4): 795-798, 2002.

170. **Mian OS, Schneider SA, Schwingenschuh P, Bhatia KP, Day BL.** Gait in SWEDDs patients: comparison with Parkinson's disease patients and healthy controls. *Mov Disord* 26(7): 1266-1273, 2011.

171. **Miller LC, Dewald JPA.** Involuntary paretic wrist/finger flexion forces and EMG increase with shoulder abduction load in individuals with chronic stroke. *Clin Neurophysiol* 123: 1216-1225, 2012.

172. **Milner-Brown HS, Stein RB.** The relation between the surface electromyogram and muscular force. *J Physiol* 246: 549-569, 1975.

173. **Morales DA, Vives-Gilabert Y, Gómez-Ansón B, Bengoetxea E, Larrañaga P, Bielza C, Pagonabarraga J, ... Delfino M.** Predicting dementia development in Parkinson's disease using Bayesian network classifiers. *Psychiatry Res* 213(2): 92-98, 2013.

174. **Moran DW, Schwartz AB.** Motor cortical representation of speed and direction during reaching. *J Neurophysiol* 82: 2676-2692, 1999.

175. **Mori S, Matsuyama K, Miyashita E, Nakajima K, Asanome M.** Basic neurophysiology of primate locomotion. *Folia Primatol (Basel)* 66(1-4): 192-203, 1996.

176. **Muro A, Nagata A.** The effects on electromechanical delay of muscle stretch of the human triceps surae. In: *Biomechanics IX-A*, edited by Winter DA, Norman RW, Wells RP, Hayes KC, Patla AE. Champaign, IL: Human Kinetics, 1985, p. 86-90.

177. **Nakayama H, Jørgensen HS, Raaschou HO, Olsen TS.** Compensation in recovery of upper extremity function after stroke: the Copenhagen Stroke Study. *Arch Phys Med Rehabil* 75(8): 852-857, 1994.

178. **Ng YS, Stein J, Ning M, Black-Schaffer RM.** Comparison of clinical characteristics and functional outcomes of ischemic stroke in different vascular territories. *Stroke* 38(8): 2309-2314, 2007.

179. **Noble M, Bruening W, Uhl S, Schoelles K.** Computer-aided detection mammography for breast cancer screening: systematic review and meta-analysis. *Arch Gynecol Obstet* 279(6): 881-890, 2009.

180. **Norman RW, Komi PV.** Electromechanical delay in skeletal muscle under normal movement conditions. *Acta Physiol Scand* 106: 241-248, 1979.

181. **Obeso JA, Rodríguez-Oroz MC, Rodríguez M, Arbizu J, Giménez-Amaya JM**. The basal ganglia and disorders of movement: pathophysiological mechanisms. *News Physiol Sci* 17: 51-55, 2002.

182. **Olanow CW, Tatton WG.** Etiology and pathogenesis of Parkinson's disease. *Annu Rev Neurosci* 22: 123-144, 1999.

183. **Paisán-Ruíz C, Jain S, Evans EW, Gilks WP, Simón J, van der Brug M, López de Munain A, … Singleton AB.** Cloning of the gene containing mutations that cause PARK8-linked Parkinson's disease. *Neuron* 44(4): 595-600, 2004.

184. **Palmer E, Ashby P, Hajek VE.** Ipsilateral fast corticospinal pathways do not account for recovery in stroke. *Ann Neurol* 32(4): 519-525, 1992.

185. **Park MC, Belhaj-Saif A, Cheney PD.** Chronic recording of EMG activity from large numbers of forelimb muscles in awake macaque monkeys. *J Neurosci Methods* 96: 153-160, 2000.

186. **Partridge CJ, Johnston M, Edwards S.** Recovery from physical disability after stroke: normal patterns as a basis for evaluation. *Lancet* 1(8529):373-375, 1987.

187. **Perlmutter JS, Mink JW.** Deep brain stimulation. *Annu Rev Neurosci* 29: 229-257, 2006.

188. **Peterson BW.** Reticulospinal projections to spinal motor nuclei. *Ann Rev Physiol* 41: 127-140, 1979.

189. **Peterson BW, Anderson ME, Filion M.** Response of pontomedullary reticular neurons to cortical, tectal and cutaneous stimuli. *Exp Brain Res* 21: 19-44, 1974.

190. **Peterson BW, Maunz RA, Pitts NG, Mackel RG.** Patterns of projection and braching of reticulospinal neurons. *Exp Brain Res* 23: 333-351, 1975.

191. **Peterson BW, Pitts NG, Fukushima K.** Reticulospinal connections with limb and axial motoneurons. *Exp Brain Res* 36: 1-20, 1979.

192. **Philipp R, Hoffmann K-P.** Arm movements induced by electrical microstimulation in the superior colliculus of the macaque monkey. *J Neurosci* 34: 3350-3363, 2014.

193. **Poliakov AV, Schieber MH.** Multiple fragment statistical analysis of post-spike effects in spike-triggered averages of rectified EMG. *J Neurosci Methods* 94: 3325-3341, 1998.

194. **Postuma RB, Lang AE**. Hemiballism: revisiting a classic disorder. *Lancet Neurology* 2(11): 661-668, 2003.

195. **Prashanth R, Roy SD, Mandal PK, Ghosh S.** Automatic classification and prediction models for early Parkinson's disease diagnosis from SPECT imaging. *Expert Syst Appl* 41: 3333-3342, 2014.

196. **Prentice SD, Drew T.** Contributions of the reticulospinal system to the postural adjustments occurring during voluntary gait modifications. *J Neurophysiol* 85(2): 679-698, 2001.

197. **Quinlan JR.** Induction of Decision Trees. *Mach Learn* 1: 81-106, 1986.

198. **Rajput AH, Rozdilsky B, Rajput A.** Accuracy of clinical diagnosis in Parkinsonism: a prospective study. *Can J Neurol Sci* 18: 275–278, 1991.

199. **Rehme AK, Volz LJ, Feis DL, Bomilcar-Focke I, Liebig T, Eickhoff SB, Fink GR, Grefkes C.** Identifying Neuroimaging Markers of Motor Disability in Acute Stroke by Machine Learning Techniques. *Cereb Cortex,* 2014. doi:10.1093/cercor/bhu100.

200. **Rekand T.** Clinical assessment and management of spasticity: a review. *Acta Neurol Scand* 122(S190):62-66, 2010.

201. **Riddle CN, Edgley SA, Baker SN.** Direct and indirect connections with upper limb motoneurons from the primate reticulospinal tract. *J Neurosci* 29: 4993-4999, 2009.

202. **Rizzolatti G, Luppino G.** The cortical motor system. *Neuron* 31(6): 889-901, 2001.

203. **Sakai ST, Davidson AG, Buford JA.** Reticulospinal neurons in the pontomedullary reticular formation of the monkey (*Macaca fascicularis*). *Neurosci* 163: 1158-1170, 2009.

204. **Sakamoto T, Gahéry Y, Mori S.** Effects of bethanecol injection into pontine reticular formation upon postural changes accompanying a food retrieval task by a forelimb in a standing cat. In: *Neurobiological Basis of Human Locomotion*, edited by Shimamura M, Grillner S, Edgerton VR. Tokyo: Japan Scientific Societies Press, 1991, p. 45–50.

205. **Salvatore C, Cerasa A, Augimeri A, Quattrone A, Castiglioni I, Gallivanone F, Gilardi MC, ... Morelli M.** Machine learning on brain MRI data for differential diagnosis of Parkinson's disease and Progressive Supranuclear Palsy. *J Neurosci Methods* 222: 230-237, 2014.

206. **Sandow A.** Excitation-contraction coupling in muscular response. *Yale J Biol Med* 25: 176-201, 1952.

207. **Savica R, Rocca WA, Ahlskog JE.** When does Parkinson disease start? *Arch Neurol* 67(7): 798-801, 2010.

208. **Schepens B, Drew T.** Independent and convergent signals from the pontomedullary reticular formation contribute to the control of posture and movement during reaching in the cat. *J Neurophysiol* 92: 2217-2238, 2004.

209. **Schepens B, Drew T.** Descending signals from the pontomedullary reticular formation are bilateral, asymmetric, and gated during reaching movements in the cat. *J Neurophysiol* 96: 2229-2252, 2006.

210. **Schepens B, Stapley P, Drew T.** Neurons in the pontomedullary reticular formation signal posture and movement both as an integrated behavior and independently. *J Neurophysiol* 100: 2235-2253, 2008.

211. **Schneider SA, Edwards MJ, Mir P, Cordivari C, Hooker J, Dickson J, Quinn N, Bhatia KP.** Patients with adult-onset dystonic tremor resembling parkinsonian tremor have scans without evidence of dopaminergic deficit (SWEDDs). *Mov Disord* 22(15): 2210-2215, 2007.

212. **Schwingenschuh P, Ruge D, Edwards MJ, Terranova C, Katschnig P, Carrillo F, Silveira-Moriyama L, … Bhatia KP.** Distinguishing SWEDDs patients with asymmetric resting tremor from Parkinson's disease: a clinical and electrophysiological study. *Mov Disord* 25(5): 560-569, 2010.

213. **Shik ML, Severin FV, Orlovskiĭ GN.** [Control of walking and running by means of electric stimulation of the midbrain]. *Biofizika* 11(4): 659-666, 1966.

214. **Shiraishi J, Li Q, Appelbaum D, Doi K.** Computer-aided diagnosis and artificial intelligence in clinical imaging. *Semin Nucl Med* 41(6): 449-462, 2011.

215. **Silveira-Moriyama L, Schwingenschuh P, O'Donnell A, Schneider SA, Mir P, Carrillo F, Terranova C, Petrie A, Grosset DG, Quinn NP, Bhatia KP, Lees AJ.** Olfaction in patients with suspected parkinsonism and scans without evidence of dopaminergic deficit (SWEDDs). *J Neurol Neurosurg Psychiatry* 80(7): 744-748, 2009.

216. **Smith SL, Timmis J.** An immune network inspired evolutionary algorithm for the diagnosis of Parkinson's disease. *Biosystems* 94(1-2): 34-46, 2008.

217. **Soteropoulos DS, Edgley SA, Baker SN.** Lack of evidence for direct corticospinal contributions to control of the ipsilateral forelimb in monkey. *J Neurosci* 31(31): 11208-11219, 2011.

218. **Soteropoulos DS, Williams ER, Baker SN.** Cells in the monkey ponto-medullary reticular formation modulate their activity with slow finger movements. *J Physiol* 590: 4011-4027, 2012.

219. **Soto O, Cros D.** Direct corticospinal control of force derivative. *J Neurosci* 31: 1944-1948, 2011.

220. **Specht DF.** Probabilistic neural networks. *Neural Netw* 3: 109-118, 1990.

221. **Sprague JM, Chambers WW.** Control of posture by reticular formation and cerebellum in the intract, anesthetized and unanesthetized and in the decerebrated cat. *Am J Physiol* 176: 52-64, 1954.

222. **Srivastava UC, Manzoni D, Pompeiano O, Stampacchia G.** Responses of medullary reticulospinal neurons to sinusoidal rotation of neck in decerebrate cat. *J Neurosci* 11: 473-486, 1984.

223. **Stifani N.** Motor neurons and the generation of spinal motor neuron diversity. *Front Cell Neurosci* 8: 293, 2014.

224. **Swedo SE, Leonard HL, Shapiro MB.** Sydenham's Chorea: Physical and Psychological Symptoms of St Vitus Dance. *Pediatrics* 91(4): 706-713, 1993.

225. **Szabo J, Cowan WM.** A stereotaxic atlas of the brain of the cynomolgus monkey (Macaca fascicularis). *J Comp Neurol* 222: 265-300, 1984.

226. **Szokol K, Glover JC, Perreault MC.** Organization of functional synaptic connections between medullary reticulospinal neurons and lumbar descending commissural interneurons in the neonatal mouse. *J Neurosci* 31(12): 4731-4742, 2011.

227. **Takakusaki K, Habaguchi T, Ohtinata-Sugimoto J, Saitoh K, Sakamoto T.** Basal ganglia efferents to the brainstem centers controlling postural muscle tone and locomotion: a new concept for understanding motor disorders in basal ganglia dysfunction. Neuroscience 119(1): 293-308, 2003.

228. **Taub E, Uswatte G, King DK, Morris D, Crago JE, Chatterjee A.** A placebo-controlled trial of constraint-induced movement therapy for upper extremity after stroke. *Stroke* 37(4): 1045-1049, 2006.

229. **Tazoe T, Perez MA.** Selective activation of ipsilateral motor pathways in intact humans. *J Neurosci* 34(42): 13924-13934, 2014.

230. **Thach WT, Goodkin HP, Keating JG.** The cerebellum and the adaptive coordination of movement. *Annu Rev Neurosci* 15: 403-442, 1992.

231. **Thijsa RD, Notermansa NC, Wokkea JHJ, van der Graafb Y, van Gijna J**. Distribution of muscle weakness of central and peripheral origin. *J Neurol Neurosurg Psychiatry* 65:794-796, 1998.

232. **Tolosa E, Wenning G, Poewe W.** The diagnosis of Parkinson's disease. *Lancet Neurol* 5(1): 75-86, 2006.

233. **Tsanas A, Little MA, McSharry PE, Ramig LO.** Accurate telemonitoring of Parkinson's disease progression by noninvasive speech tests. *IEEE Trans Biomed Eng* 57(4): 884-893, 2010.

234. **Turton A, Wroe S, Trepte N, Fraser C, Lemon RN.** Contralateral and ipsilateral EMG responses to transcranial magnetic stimulation during recovery of arm and hand function after stroke. *Electroencephalogr Clin Neurophysiol* 101(4): 316-328, 1996.

235. **Twitchell TE.** The restoration of motor function following hemiplegia in man. *Brain* 74(4): 443-480, 1951.

236. **Uchiyama Y, Asano T, Kato H, Hara T, Kanematsu M, Hoshi H, Iwama T, Fujita H.** Computer-aided diagnosis for detection of lacunar infarcts on MR images: ROC analysis of radiologists' performance. *J Digit Imaging* 25(4): 497-503, 2012.

237. **Ugolini G, Kuypers HG.** Collaterals of corticospinal and pyramidal fibres to the pontine grey demonstrated by a new application of the fluorescent fibre labelling technique. *Brain Res* 365(2): 211-227, 1986.

238. **Utiumi MA, Felício AC, Borges CR, Braatz VL, Rezende SA, Munhoz RP, Bressan RA, Ferraz HB, Teive HA.** Dopamine transporter imaging in clinically unclear cases of parkinsonism and the importance of scans without evidence of dopaminergic deficit (SWEDDs). *Arq Neuropsiquiatr* 70(9): 667-673, 2012.

239. **Valls-Solé J, Kumru H, Kofler M.** Interaction between startle and voluntary reactions in humans. *Exp Brain Res* 187(4): 497-507, 2008.

240. **Valls-Solé J, Rothwell JC, Goulart F, Cossu G, Muñoz E.** Patterned ballistic movements triggered by a startle in healthy humans. *J Physiol* 516(3):931-938, 1999.

241. **Valls-Solé J, Solé A, Valldeoriola F, Munoz E, Gonzalez LE, Tolosa ES.** Reaction time and acoustic startle in normal human subjects. *Neurosci Lett* 195: 97–100, 1995.

242. **Walker FO.** Huntington's disease. *Lancet* 369(9557): 218–228, 2007.

243. **Wang S, Summers RM.** Machine learning and radiology. *Med Image Anal* 16(5): 933-951, 2012.

244. **Wang T, Wang J, Yin C, Liu R, Zhang JH, Qin X.** Down-regulation of Nogo receptor promotes functional recovery by enhancing axonal connectivity after experimental stroke in rats. *Brain Res* 1360: 147-158, 2010.

245. **Ward NS.** Functional reorganization of the cerebral motor system after stroke. *Curr Opin Neurol* 17(6): 725-730, 2004.

246. **Winter EM, Brookes FBC.** Electromechanical response times and muscle elasticity in men and women. *Eur J Appl Physiol* 63: 124-128, 1991.

247. **Yang HJ, Kim YE, Yun JY, Ehm G, Kim HJ, Jeon BS.** Comparison of sleep and other non-motor symptoms between SWEDDs patients and de novo Parkinson's disease patients. *Parkinsonism Relat Disord* 20(12): 1419-1422, 2014.

248. **Yao J, Chen A, Carmona C, Dewald JP.** Cortical overlap of joint representations contributes to the loss of independent joint control following stroke. *Neuroimage* 45(2): 490-499, 2009.

249. **Yeo SS, Chang MC, Kwon YH, Jung YJ, Jang SH.** Corticoreticular pathway in the human brain: diffusion tensor tractography study. *Neurosci Lett* 508(1): 9-12, 2012.

250. **Yousefi J, Hamilton-Wright A.** Characterizing EMG data using machine-learning tools. *Comput Biol Med* 51: 1-13, 2014.

251. **Yu WS, Kilbreath SL, Fitzpatrick RC, Gandevia SC.** Thumb and finger forces produced by motor units in the long flexor of the human thumb. *J Physiol* 583: 1145-1154, 2007.

252. **Zaaimi B, Edgley SA, Soteropoulos DS, Baker SN.** Changes in descending motor pathway connectivity after corticospinal tract lesion in macaque monkey. *Brain* 135(7): 2277-2289, 2012.

253. **Ziemann U, Ishii K, Borgheresi A, Yaseen Z, Battaglia F, Hallett M, Cincotta M, Wassermann EM.** Dissociation of the pathways mediating ipsilateral and

contralateral motor-evoked potentials in human hand and arm muscles. *J Physiol* 518(3): 895-906, 1999.

254. **Zweig RM, Whitehouse PJ, Casanova MF, Walker LC, Jankel WR, Price DL.** Loss of pedunculopontine neurons in progressive supranuclear palsy. *Ann Neurol* 22(1): 18-25, 1987.